University of Alberta

A Fundamental Study of Silicon Nanocrystals Derived From Hydrogen Silsesquioxane

by

Colin M. Hessel

A thesis submitted to the Faculty of Graduate Studies and Research
in partial fulfillment of the requirements for the degree of

Doctor of Philosophy

Department of Chemistry

Edmonton, Alberta
Fall, 2008

Library and Archives Canada

Published Heritage Branch

395 Wellington Street
Ottawa ON K1A 0N4
Canada

Bibliothèque et Archives Canada

Direction du Patrimoine de l'édition

395, rue Wellington
Ottawa ON K1A 0N4
Canada

Your file Votre référence
ISBN: 978-0-494-46332-1
Our file Notre référence
ISBN: 978-0-494-46332-1

NOTICE:
The author has granted a non-exclusive license allowing Library and Archives Canada to reproduce, publish, archive, preserve, conserve, communicate to the public by telecommunication or on the Internet, loan, distribute and sell theses worldwide, for commercial or non-commercial purposes, in microform, paper, electronic and/or any other formats.

The author retains copyright ownership and moral rights in this thesis. Neither the thesis nor substantial extracts from it may be printed or otherwise reproduced without the author's permission.

AVIS:
L'auteur a accordé une licence non exclusive permettant à la Bibliothèque et Archives Canada de reproduire, publier, archiver, sauvegarder, conserver, transmettre au public par télécommunication ou par l'Internet, prêter, distribuer et vendre des thèses partout dans le monde, à des fins commerciales ou autres, sur support microforme, papier, électronique et/ou autres formats.

L'auteur conserve la propriété du droit d'auteur et des droits moraux qui protège cette thèse. Ni la thèse ni des extraits substantiels de celle-ci ne doivent être imprimés ou autrement reproduits sans son autorisation.

In compliance with the Canadian Privacy Act some supporting forms may have been removed from this thesis.

While these forms may be included in the document page count, their removal does not represent any loss of content from the thesis.

Conformément à la loi canadienne sur la protection de la vie privée, quelques formulaires secondaires ont été enlevés de cette thèse.

Bien que ces formulaires aient inclus dans la pagination, il n'y aura aucun contenu manquant.

Canada

This thesis is dedicated to my friend, my mentor, and my father,

Dr. Patrick Hessel

Abstract

A novel synthesis for gram quantities of luminescent, oxide-embedded and freestanding silicon nanocrystals is presented. The reductive thermal processing of hydrogen silsesquioxane (HSQ) yields size-controlled oxide-embedded silicon nanocrystals, and their subsequent liberation through straight-forward hydrofluoric (HF) acid etching procedures allows tailoring of their optical response throughout the visible region of the electromagnetic spectrum.

The thermally-induced transformation of HSQ to oxide-embedded silicon nanocrystals occurs via a multi-step process, involving cage rearrangement, network decomposition to form silane-like species, *in-situ* silane decomposition to form elemental silicon clusters, and subsequent nucleation, growth and crystallization to form silicon nanocrystals in an SiO_2 matrix. This formation process was confirmed using detailed spectroscopic and microscopic characterization.

The luminescence characteristics of oxide-embedded and freestanding silicon nanocrystals were determined using laser-based photoluminescence and X-ray excited optical luminescence spectroscopy. Oxide-embedded systems were found to exhibit two emission bands in the visible region of the electromagnetic spectrum: a high energy emission that is independent of nanocrystal size, and a size-dependent low energy emission. HF etching was employed to liberate the silicon nanocrystals from the encapsulating oxide in order to assign the origin of these emission bands. Oxide removal was accompanied by a loss of the green emission, indicating that it is of silicon oxide

origin. Progressively decreasing the nanocrystal size with extended HF treatment was accompanied by a blue-shift in the emission energy and a narrowing of the emission profile, indicative of an increase in the bandgap energy and a narrowing of the density of states, respectively. This behavior establishes that the low energy emission band is a result of quantum confinement effects in sub-5nm silicon nanocrystals.

It was found that HSQ is an ideal precursor for conformal coating of both flat and not-flat surfaces with oxide-embedded silicon nanocrystals, highlighting its device application potential. Patterning of luminescent sub-10 nm structures was also achieved by electron beam writing and subsequent thermal processing.

The ability to produce large quantities of size-controlled oxide-embedded and freestanding silicon nanocrystals in bulk and thin film architectures demonstrates that HSQ is currently the most versatile silicon nanocrystal precursor available.

Acknowledgement

I would like to thank the University of Alberta, in particular the members of the department of chemistry, for providing a wonderful learning environment and effective the teaching tools over the last nine years. In the last decade I have been inspired by the teaching and direction of many professors, postdoctoral fellows, and students. I would like to thank Dr. Martin Cowie, Dr. Mariusz Klobukowski, Dr. Derrick Clive, Dr. Arthur Mar, Dr. Al Meldrum, and Dr. Ronald Cavell for being exemplary scientific role models during both my undergraduate and graduate careers. The chemistry department machine, electronic, and glass shops are thanked for their incredible ability to produce the complex reactors and instruments necessary for present investigation.

I would like to thank my supervisor, Dr. Jonathan Veinot, for encouraging my scientific creativity, giving me the freedom to test my many preposterous hypotheses, and for believing in my capabilities as both a student and a teacher. Dr. Veinot is also thanked for allowing me the time necessary to rekindle my passion for science away from the laboratory when the pressures of graduate school seemed overwhelming.

The members of the Veinot group, including Dianne Rollings, Janet Macdonald, and Shaune Mcfarlane, are thanked for their productive discussions, scholarly challenge, and continual support. In particular I would like to thank Eric Henderson, who was once my protégé, but has now become my intellectual counterpoint. Eric's relentless curiosity and continual input was crucial in developing and fine-tuning the HF etching procedure used to liberate

freestanding silicon nanocrystals from oxide matrixes. Eric was also instrumental in developing an ingenious method to transfer highly reactive, hydride-terminated silicon nanocrystals under an inert atmosphere to synchrotron beamline endstations. These efforts resulted in the first X-ray absorption spectrum of oxide-free silicon nanocrystals and conclusive evidence for quantum confinement in HSQ derived silicon nanocrystals. Eric's technical expertise, in conjunction with his unwavering loyalty and impeccable ethical standards have enriched my graduate career and provided me with a life long friend.

My best friend, Rusty Hessel, is thanked for always looking out for me and not being afraid to take me down a couple notches when my ego became hyperactive. Ms. Christi Horne is thanked for helping me become one with the wonderful earth we inhabit, and for providing me with significant motivation to complete a PhD. My mother, Laura Hessel, is thanked for her extraordinary ability to calm me down with only the sound of her voice, and for teaching me to stand up for what I believe in, even in the face of adversity and potential consequence. Lastly, I would like to thank my mentor, Dr. Patrick Hessel, for being a tangible model of an ideal scientist. My efforts to emulate Dr. Hessel have provided me with a greater understanding of the scientific method, and have solidified my motivation for scientific exploration.

Table of Contents

Chapter 1: Introduction to luminescent silicon nanomaterials.....1

1.1 Introduction.....2

1.2 Semiconductors.....3

1.3 Silicon luminescence.....9

1.4 Preparation of low dimensional silicon.....15

1.4.1 Physical methods.....15

1.4.2 Solution-based reduction methods.....19

1.4.2 Percursor thermolysis and pyrolysis.....22

1.5 Silsesquioxanes.....24

1.6 Thesis outline.....26

1.7 References.....27

Chapter 2: Hydrogen silsesquioxane: A molecular precursor for Si-NC/SiO_2 composites and freestanding hydride surface terminated silicon nanocrystals.....29

2.1 Introduction.....30

2.2 Experimental details.....35

2.2.1 Reagents and materials.....35

2.2.2 Bulk Si-NC/SiO_2 composite preparation.....35

2.2.3 Liberation of hydride surface-terminated freestanding Si-NCs.....37

2.2.4 Thermogravimetric analysis....38
2.2.5 X-ray photoelectron spectroscopy....38
2.2.5 Material characterization and instrumentation....39
2.3 Results and discussion....40
2.3.1 Thermogravimetric analysis....41
2.3.2 X-ray powder diffraction....44
2.3.3 X-ray photoelectron spectroscopy....49
2.3.4 Fourier transform infrared spectroscopy....51
2.3.5 Photoluminescence spectroscopy....53
2.3.6 Transmission electron microscopy, energy dispersive X-ray spectroscopy and selected area electron diffraction....55
2.4 Conclusion....58
2.5 References....59

Chapter 3: An investigation of the formation and growth of oxide-embedded silicon nanocrystals in hydrogen silsesquioxane derived nanocomposites....65

3.1 Introduction....66
3.2 Experimental details....69
3.2.1 Reagents and materials....69
3.2.2 Bulk Si-NC/SiO_2 composite preparation....69
3.2.3 X-ray photoelectron spectroscopy....71

3.2.4 X-ray photoelectron spectroscopy analysis.....71
3.2.5 X-ray powder diffraction.....72
3.2.6 Optical spectroscopy.....72
3.3 Results and discussion.....73
3.3.1 X-ray photoelectron spectroscopy.....73
3.3.2 X-ray powder diffraction.....77
3.3.3 Fourier transform infrared and Raman spectroscopy.....79
3.3.4 Photoluminescence spectroscopy.....81
3.3.5 Factors influencing silicon nanodomain formation, growth, and crystallization.....84
3.4 Conclusion.....86
3.5 References.....87

Chapter 4: The origin of luminescence from silicon nanocrystals: A near edge X-ray absorption fine structure (NEXAFS) and X-ray excited optical luminescence (XEOL) study of oxide-embedded and freestanding systems.....91

4.1 Introduction.....92
4.2 Experimental details.....96
4.2.1 Sample preparation.....96
4.2.2 Hydrofluoric acid etching of oxide-embedded silicon nanocrystal composites.....97
4.2.3 X-ray analysis.....98

4.2.4 X-ray photoelectron spectroscopy.....99

4.2.5 X-ray photoelectron spectral analysis.....99

4.3 Results and discussion.....100

4.4 Conclusion.....117

4.5 References.....119

Chapter 5: Direct patterning, conformal coating, and erbium doping of luminescent Si-NC/SiO_2 thin films from solution processable hydrogen silsesquioxane.....123

5.1 Introduction.....124

5.2 Experimental details.....127

5.2.1 Sample preparation.....127

5.2.2 Optical characterization.....128

5.2.3 Scanning and transmission electron microscopy.....128

5.3 Results and discussion.....129

5.4 Conclusion.....136

5.5 References.....137

Chapter 6: Conclusions.....139

6.1 Conclusions.....140

6.2 Future directions.....148

6.3 References.....149

List of Tables

Table 1.1 Typical room temperature conductivities and carrier densities for metals, semimetals, semiconductors, and insulators.....4

Table 1.2 The lattice constant, bandgap energy, Pauling covalent radii, and bond dissociation energy of Group IV elements.....6

Table 1.3 The dielectric constants and Bohr exciton radii for common semiconductors.....13

Table 2.1 Samples of hydrogen silsesquioxane (HSQ) processed at specified temperatures for 1 hour in 4%H_2/96%N_2.....36

Table 2.2 Etching parameters and luminescence information for samples of HSQ processed at 1100°C and etched for specified times in solutions of 1:1:1 49% HF : H_2O :ethanol.....38

Table 3.1 Samples of HSQ processed at 18°C/min for specified times and temperatures under 5%H_2/95%Ar. The silicon L-edge electron binding energies for $Si^{(0)}$ and $Si^{(IV)}$ are presented with theoretical estimates of nanocrystal size for the corresponding samples.....70

Table 4.1 Samples of hydrogen silsesquioxane (HSQ) processed in 5% H_2/95% Ar at specified temperatures and times with a heating rate of 18°C/min. HSQ processed at 1100°C was etched with solutions of 49% HF, water, ethanol, and for specified times to yield freestanding silicon nanocrystals.....97

List of Figures

Figure 1.1 Schematic bandgap model for a metal, semiconductor, and insulator.....5

Figure 1.2 The theoretically modeled density of states for a semiconductor of decreasing particle dimension.....12

Figure 1.3 Silicon 2p core level spectra of SiO_x ((a) fractured, (b) scratched, (c) sputter-cleaned sample) fitted to five peaks corresponding to different Si oxidation states, respectively.....17

Figure 1.4 The molecular structure of hydrogen silsesquioxane (HSQ).....25

Figure 2.1 Photographs of as prepared and ground samples of HSQ processed at 500 - 1100°C.....37

Figure 2.2 Thermogravimeteric analysis of HSQ heated at 10°C/min in 4% H_2 : 96% N_2 atmosphere.....41

Figure 2.3 Heating rate dependence of HSQ weight loss in N_2 and 5% H_2/95% Ar.....42

Figure 2.4 X-ray powder diffraction of HSQ composites processed between 800 - 1100°C showing the peak thermal processing temperature dependence of Si nano-domain crystallinity.....47

Figure 2.5A X-ray powder diffraction of composites processed at 800°C and 1100°C. Characteristic (111), (220), and (311) reflections of diamond structure are noted.....48

Figure 2.5B X-ray powder diffraction of etched silicon nanocrystals.....48

Figure 2.6 High-resolution X-ray photoelectron spectroscopy of the Si 2p spectral region of HSQ processed at 800 and 1100°C.....50

Figure 2.7 Infrared spectra of HSQ, HSQ processed at 1100°C, and samples of oxide-embedded silicon nanocrystals etched in HF for specified times.....52

Figure 2.8 Photoluminescence spectrum obtained upon excitation of a thin film of HSQ processed at 1100°C dropcoated from a pentane suspension of the finely ground powder onto optical grade fused silica using the 325 nm line of a He-Cd laser.....54

Figure 2.9 Photoluminescence spectra of pentane solutions containing red, orange, yellow, and green emitting freestanding silicon nanocrystals. Inset: Photographs of photoluminescence observed from pentane suspensions of freestanding silicon nanocrystals upon exposure to a standard handheld UV light.....54

Figure 2.10 A brightfield transmission electron micrograph of HSQ processed at 1100°C. Inset: Selected area electron diffraction of Si-NC/SiO_2 thin film composite showing the characteristic (111), (200), and (311), reflections of diamond structure silicon.....56

Figure 2.11A A representative bright-field transmission electron micrograph of red emitting, freestanding silicon nanocrystals.....57

Figure 2.11B Size distribution of red emitting, freestanding silicon nanocrystals providing average particle dimensions of d = 3.41 nm (2σ = 1.40 nm; n = 188).....57

Figure 3.1 Representative Shirley background subtracted high-resolution XP spectra of the Si 2p region for Si-NC/SiO_2 composites obtained from processing HSQ at the indicated temperature.....73

Figure 3.2 Shirley background subtracted high-resolution XP spectrum of the Si 2p region for Si-NC/SiO_2 for HSQ processed at 1100°C. For clarity only the Si $2p_{3/2}$ spin-orbit couple partner lines are shown.....74

Figure 3.3 The relationship between Si $2p_{3/2}$ binding energy and peak processing temperature.....76

Figure 3.4 X-ray powder diffraction patterns showing the appearance of characteristic silicon (111), (220), (311), (400), (331), (422), (333), (440), and (531) reflections for samples of HSQ processed between 1100°C and 1400°C. Peak processing temperatures are indicated for clarity.....77

Figure 3.5 FTIR spectra of HSQ composites processed between 300°C and 900°C showing a marked decrease in Si-H stretching and increase in Si-O-Si stretching with increased processing temperature. Processing temperatures are noted for clarity.....79

Figure 3.6 The Si-Si region of the Raman spectra of HSQ composites processed between 300°C and 900°C showing a clear increase in Si-Si vibration with increased peak processing temperature. Processing temperatures are provided for clarity.....79

Figure 3.7A Normalized PL spectra for cast films of HSQ processed at 1100°C for 1hr, 2hr, 5hr, 10hr, and 24hr.....81

Figure 3.7B Normalized PL spectra for cast films of HSQ processed between 1100°C and 1400°C.....81

Figure 4.1 Normalized FLY Si K-edge NEXAFS spectra for HSQ thermally processed between 500°C and 1100°C for 1 hour in 5% H_2/95% Ar. FLY spectra are also included for SiO_2 and elemental Si standards for comparison. The absorption maxima for Si and SiO_2, 1841 eV and 1848 eV respectively, are noted for reference. Spectra have been shifted vertically for clarity.....101

Figure 4.2A Schematic of the thermal degradation of HSQ to form oxide-embedded Si-NCs.....102

Figure 4.2B,C HSQ has a theoretical silicon to oxygen ratio of 1 to 1.5, and a Si K-edge absorption maximum at 1845 eV, an energy between that of the products, elemental Si (1841 eV) and SiO_2 (1848 eV)...,102

Figure 4.3 Normalized X-ray excited optical luminescence (XEOL) spectra of oxide-embedded silicon nanocrystals. The inset indicates the selected X-ray excitation energy for each XEOL spectrum with respect to the NEXAFS spectrum. The spectra are normalized to the intensity maximum of the 540 nm emission peak to clearly indicate how the intensity of the emission bands change as a function of excitation energy.....105

Figure 4.4 Shirley background subtracted high-resolution XP spectrum of the Si 2p region for HSQ processed at 1100°C. For clarity, the Si $2p_{1/2}$ spin-orbit couple partner lines have been omitted. All silicon oxide species, $Si^{(n)}$ (n = 0 – IV) are labeled for clarity...109

Figure 4.5 Comparison of the Si K-edge TEY and FLY spectra for oxide-embedded silicon nanocrystals, HF prepared freestanding silicon nanocrystals and, a ground silicon wafer standard. Spectra have been shifted vertically for clarity.....112

Figure 4.6 Normalized FLY Si K-edge NEXAFS spectra of hydride-terminated freestanding silicon nanocrystals produced by etching composites of oxide-embedded silicon nanocrystals for specified times in solutions of HF. Spectra for HSQ processed at 1100°C and a silicon wafer standard are included for reference. The absorption maxima for Si and SiO_2, 1841 eV and 1848 eV respectively, are noted for reference. Spectra have been shifted vertically for clarity.....114

Figure 4.7 Normalized X-ray excited optical luminescence (XEOL) spectra of oxide-embedded silicon nanocrystals and hydride-terminated freestanding silicon nanocrystals produced by etching composites of for 1 hour and 1.5 hours with solutions of hydrofluoric acid. The inset depicts the X-ray excitation energy for each XEOL spectrum at 1841 eV.....116

Figure 5.1A Structure of hydrogen silsesquioxane.....126

Figure 5.1B Films of HSQ on a fused silica wafer before and after thermal processing at 1100°C.....126

Figure 5.1C The HSQ structure collapses upon thermal processing to form Si-NCs in SiO_2, as shown in the high-resolution TEM image.....126

Figure 5.1D The photoluminescence spectrum (λ_{ex} = 325 nm) obtained from thermally processed films of HSQ.....126

Figure 5.2A SEM micrograph of a line pattern of indicated line widths (1μm, 100 nm, 10 nm, 7 nm).....131

Figure 5.2B Reflective optical image of the same line pattern in Figure 5.2A.....131

Figure 5.2C Photoluminescence image of the line pattern shown in Figure 5.2A.....131

Figure 5.2D SEM micrograph of a more complex pattern of HSQ.....131

Figure 5.2E Reflective optical image of pattern in Figure 5.2D.....131

Figure 5.2F Photoluminescence image of the line pattern shown in Figure 5.2D.....131

Figure 5.3A Panels a-d show SEM images of optical fibers with Si-NC/SiO_2 coatings of decreasing thicknesses. Thick films crack and peel from the fiber surface. Thinner Si-NC/SiO_2 coatings are smooth and featureless.....133

Figure 5.3F The fluorescence microscope image of the red-IR emission emanating from the cleaved end of the fiber shown upon 488 nm excitation along the side of the fiber.....133

Figure 5.4 A photoluminescence spectrum of Er doped Si-NC/SiO_2 composites upon excitation with the 325 nm line of a He-Cd laser excitation source.....135

List of Schemes

Scheme 2.1 Thermal processing of hydrogen silsesquioxane (HSQ) to produce silicon nanocrystal/SiO_2 (Si-NC/SiO_2) composites.....35

Scheme 2.2 Stages of HSQ thermal degradation in an inert atmosphere.....43

Scheme 3.1 Processing HSQ at: A. $\leq$400°C for 1 hour yields unidentified, crosslinked silsesquioxane materials. B. 500-800°C for 1 hr. provides material containing low valent Si, Si-H and Si-O bonding. C. 900°C-1400°C for 1 hr. induces crystallization and growth of Si nanodomains.....85

List of Equations

Equation 2.1 Scherrer equation.....45

Equation 2.2 Isolation of size related instrumental broadening from total broadening and instrumental broadening equation.....45

Chapter 1:

Introduction to luminescent silicon nanomaterials

1.1. Introduction

Materials chemistry encompasses the production, investigation, and application of substances with controlled physical and chemical properties. A modern branch of materials chemistry currently gaining momentum includes the fields of nanoscience and nanotechnology. Nanoscience aims to prepare and investigate materials with physical dimensions less than 100 nm, while nanotechnology focuses on the utilization of these materials for application-based technologies. As materials approach this size regime the surface area to volume ratio increases and novel chemical and physical properties emerge. These properties may be attributed to an increased number of high energy interfacial surface sites that lead to materials with increased catalytic activity, conductivity, and unique optical behavior.

Carbon has been shown to possess significantly different physical properties when reduced to nanoscale dimensions. Bulk graphite (i.e., > 100 nm) has a conductivity and carrier density characteristic of a semimetal (Table 1.1); however, when reduced to nanoscale dimensions, carbon nanotubes (i.e., rolled sheets of graphene) have been shown to attain electron mobility's and conductivities characteristic of metals.[1,2] Consequently, carbon nanotubes have been proposed as "quantum wires" in state-of-the-art microelectronic applications where traditional materials such as copper have impeded conductivities at this size scale due to increased phonon scattering.[3]

The above illustrates the exciting possibilities of exploring materials on nanometer length-scales and highlights some of the reasons for the exponential growth of nanoscience. Many other interesting phenomena emerge as a result of reducing

materials to nanoscale dimensions. Of particular pertinence to the present thesis are the size-related phenomena associated with Group IV nanoscale semiconductors, specifically the emergence of photoluminescence (PL) from sub-5 nm silicon nanocrystals (Si-NCs). However, before discussing these phenomena in detail a general discussion of semiconductors is warranted.

1.2. Semiconductors

Historically, the term semiconductor was applied to materials exhibiting conductivities greater than those of insulators, but less than metals. This definition, however, is incomplete, and fails to fully differentiate semiconductors from metals and insulators. To fully draw a demarcation between these materials it is helpful to examine their conductivities as a function of temperature. As the temperature is increased in turn for semiconductors and metals, the conductivities increase and decrease, respectively. The increase in semiconductor conductivities is due to thermal promotion of charge carrying species across the bandgap (*vide infra*). In contrast, the conductivities of metals decrease with increasing temperature due to an increase in the number of collisions between charge carriers and vigorously vibrating metal atoms. As for insulators, increasing their temperatures commonly results in material break down before any significant rise in conductivity. Table 1.1 lists the typical conductivity and carrier density ranges for metals, semimetals, semiconductors, and insulators.

Table 1.1. Typical room temperature conductivities and carrier densities for metals, semimetals, semiconductors, and insulators.[4]

Type of material	Conductivity (ohm^{-1} cm^{-1})	Carrier density (cm^{-3})	Example
Metal	10^5 - 10^{10}	10^{22}	Au, Ag, Cu
Semimetal	10^2 - 10^5	10^{17} - 10^{21}	Graphite (C), HgTe
Semiconductor	10^{-9} - 10^2	$< 10^{17}$	Si, Ge, GaAs
Insulator	$< 10^{-9}$	$<< 1$	SiO_2, CaF_2

The moderate insulating character of semiconductors provides a barrier to isotropic charge movement which is related to the energy required to promote a charge carrier from a ground-state to an excited-state orbital. In a bulk crystal, the accumulation of many of these discrete energy states form a pseudocontinuous energy continuum, or band, and the energy difference between the collective occupied ground states and unoccupied excited states is the bandgap (Figure 1.1).

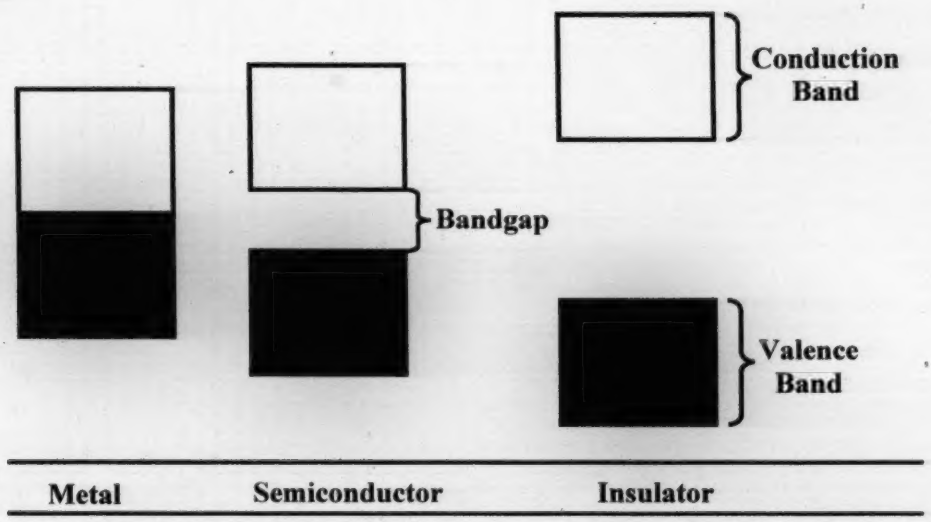

Figure 1.1. Schematic bandgap model for a metal, semiconductor, and insulator.

The magnitude of the bandgap is an intrinsic material property and is dependent on the extent of covalent bonding between atoms. The Group IV elements silicon, germanium, and α-tin are classified as semiconductors and have the general valence electron configuration Xs^2Xp^2, where X = 2, 3, 4, and 5 for carbon (diamond), silicon, germanium, and tin, respectively. With 4 valence electrons, each atom may be described as having sp^3-type hybridized bonding with 4 nearest neighbors located at four corners of a regular tetrahedron. The extent by which hybridization occurs is dependant on the energy difference between the unhybridized s and p-orbitals, which decreases down the group and results in more effective orbital mixing. In their elemental form, these materials crystallize predominantly in a diamond structure, consisting of an 8 atom unit cell that is dependant on the atomic radius. Table 1.2 summarizes some key physical constants for Group IV diamond structure solids.

Table 1.2. The lattice constant, bandgap energy, Pauling covalent radii, and bond dissociation energy of Group IV elements.

Group IV element	Lattice constant*[a] (nm)	Bandgap energy*[b], eV (λ, nm)	Pauling covalent radius[d] (Å)	Bond dissociation energy[c] (kJ/mol)
Diamond (C)	0.357	5.5 (230)	0.77	346
Silicon (Si)	0.543	1.1 (1100)	1.17	222
Germanium (Ge)	0.566	0.66 (1900)	1.22	188
Grey tin (α-Sn)	0.649	<0.1 (12,000)	1.40	146

* Constants taken from madelung.[5]

[a] Repeat distance, a of the cubic unit cell at 300 K, obtained from X-ray diffraction data

[b] Bandgap energy at 300 K

[c] Bond-dissociation energy determined from heats of atomization data.[6]

[d] Covalent radii given as one-half of observed covalent radius.[7]

Considering these elements crystallize in similar diamond structures, the increase in the Pauling covalent radius down the group results in a corresponding increase in the lattice constant. This increase in atomic separation leads to gradual, but pronounced changes in their bonding characteristics. As the Pauling covalent radius increases from carbon to tin, the extent of orbital overlap between adjacent atoms decreases, resulting in decreased bond strengths. The strength of a bond can also be correlated with the ease with which an electron can overcome the bandgap energy, and conduct charge. Therefore, the strong bonding observed in carbon leads to insulating character, while the relatively weaker bonding in silicon and germanium leads to semiconductor behavior. The control and manipulation of electrons is of the utmost

importance for devices in the "information age", and thus, silicon and germanium have become the most technologically relevant Group IV elements. For these elements, the barrier to charge movement (i.e., bandgap energy) is easily overcome by the application of a modest turn-on voltage (< 5 V), yet the slight insulating character reduces the potential for isotropic charge movement, an essential requirement for data retention in microelectronics.

The use of semiconductors is not only limited to the microelectronics industry, but has also been extended to the field of photonics. In photonic applications, semiconductors may act both as the light-emitting material and as the device platform. This architecture leads to decreased problems associated with material compatibility as well as infrastructure costs associated with fabrication. The first demonstration of a photonic device designed purely from semiconductor materials was reported by H. J. Round in 1907.[8] Round successfully demonstrated electroluminescence (EL) from SiC in what became the first proof-of-concept light emitting diode (LED). This initial work paved the way for the thriving LED industry and many other applications that utilize luminescent semiconducting materials for efficient light generation.

It is important to note that the luminescent semiconductor materials of choice for most commercial applications are not based on Group IV elements, but are instead a combination of two or more elements that form a compound semiconductor. Compound semiconductors are materials engineered to mimic the electronic properties of their Group IV counterparts. They are typically formed by combining elements on either side of Group IV (i.e., III + V and II + VI) with the intent of producing a material that is isoelectronic with Group IV elements, having an average of 4 valence electrons.

For example, when gallium (Group III) is epitaxially combined with a stoichiometric proportion of arsenic (Group V), the resulting material has an average of 4 valence electrons and consequently conductivity characteristics of Group IV semiconductors. Varying the proportions of each component allows for precise manipulation of the bandgap, and since it is this bandgap that determines the energy of the light emission, this translates to control over the luminescence. This approach to producing well-defined semiconductors has become extremely versatile, in part because of the development of techniques such as molecular beam epitaxy (MBE) that allow for finely controlled deposition of compound semiconductor components. As a result, the luminescence from compound semiconductors can be tuned to specific energies ranging from infrared (IR) to deep UV regions of the electromagnetic (EM) spectrum.[4]

In addition to allowing for precise tuning of the emission energy from compound semiconductors, these materials are also superior to pure Group IV semiconductors with respect to luminescence quantum efficiency (i.e., the number of emitted photons vs. the number of absorbed photons). In bulk crystals, indirect bandgap Group IV semiconductors like silicon and germanium do not exhibit efficient room temperature PL or EL, whereas direct bandgap compound semiconductors like CdSe and ZnS have quantum efficiencies between 30 and 50 %.[9] The reason for this stark contrast arises from a fundamental difference between direct and indirect bandgap materials. In direct bandgap materials, the top of the valence band and the bottom of the conduction band occur at the same momentum coordinate in reciprocal space (i.e., k-space). Because this transition occurs at the same point in reciprocal space, a change in the momentum is not necessary for a radiative transition. For indirect bandgap

materials however, the valence band and conduction band do not occur at the same momentum coordinate and therefore a simultaneous change in momentum is necessary to facilitate a radiative transition. As a result, for indirect bandgap semiconductors a phonon (i.e., lattice vibration) must occur if the vertical bandgap transition is to proceed. The additional requirement of a phonon to assist the radiative transition decreases the probability of the transition. This decreased probability manifests itself in a marked decrease of the photoluminescent quantum yield for indirect bandgap materials. Given that quantum efficiency is a key figure of merit for photonic devices, direct bandgap semiconductors, exhibiting high photoluminescence quantum yields, are the materials of choice for light generation. To date, exploitation of indirect bandgap semiconductors such as silicon and germanium in photonic devices has been limited. However, the above optical limitations of indirect materials only manifests itself in bulk semiconductors, and as will be shown later, these limitations may be circumvented for indirect bandgap semiconductors by moving to the nano-regime.

1.3. Silicon Luminescence

Although the radiative recombination probability in bulk silicon is extremely low at room temperature, it is known that cooling silicon to liquid helium temperatures can minimize the mechanisms associated with non-radiative recombination resulting in weak luminescence. The application of bulk silicon to photonic materials is questionable, however, due to the practical challenges associated with cooling to cryogenic temperatures.

When the particle dimension of silicon is decreased to approximately 5 nm, the low quantum efficiencies associated with non-radiative recombination are suppressed due to a transition from an indirect to a pseudo-direct bandgap material, and visible room temperature luminescence is observed. Leigh Canham, working at The Royal Signals and Radar Establishment in the United Kingdom, was the first to report this phenomenon in 1990.[10] Canham anodically etched silicon wafers in solutions of hydrofluoric acid (HF) producing a porous silicon (p-Si) material that exhibited efficient PL upon UV illumination. The source of this emission was attributed to the presence of sub-5 nm "silicon wires" that formed during the etching process. Canham reported that the emission was due to the two dimensional quantum confinement of carriers which resulted in an increased bandgap of silicon. Canham suggested that decreasing the silicon particle size also resulted in an increase in the density of states (DOS).

The DOS in a semiconductor is the number of states per unit energy that satisfy the time independent Schrödinger equation. All possible electronic states for a semiconductor are described as points in k-space by the vectors k_x, k_y, k_z. If the combination of these vectors produce an integer or non-zero wave function solution then the electronic state is allowed. As the dimension of a semiconductor is decreased, one or more k-space vectors become constant and the carriers experience strong quantum confinement in one or more dimensions, depending on the geometry of the structure. Semiconductors can separated into four different dimensional configurations; three dimensional (bulk material), two dimensional (quantum well or slab), one dimensional (quantum wire), and zero dimensional (quantum dot). Electrons in bulk

materials do not experience strong confinement effects and are free to move in three directions. In the case of a quantum well, one k-space vector becomes fixed and the electrons are strongly confined in one direction, producing a step function DOS (Figure 1.2). A semiconductor wire has two fixed k-space vectors and the electrons become strongly confined in two directions, leading to a limited number of solutions to the Schrödinger equation and a corresponding decrease in the DOS. Confinement in three directions only occurs in pseudo zero dimensional semiconductors (quantum dots) where all three k-space vectors are held constant and the electrons experience confinement in three dimensions. In this extreme case the restriction of all k-space vectors leads to unique solutions of the Schrödinger equation at specific energies. Although the DOS for a semiconductor is represented schematically in Figure 1.2, it can be derived easily and accurately with modern computational methods. The detailed mathematical derivation of the DOS function, as well as its modification as a function of particle size can be found in reference 4.

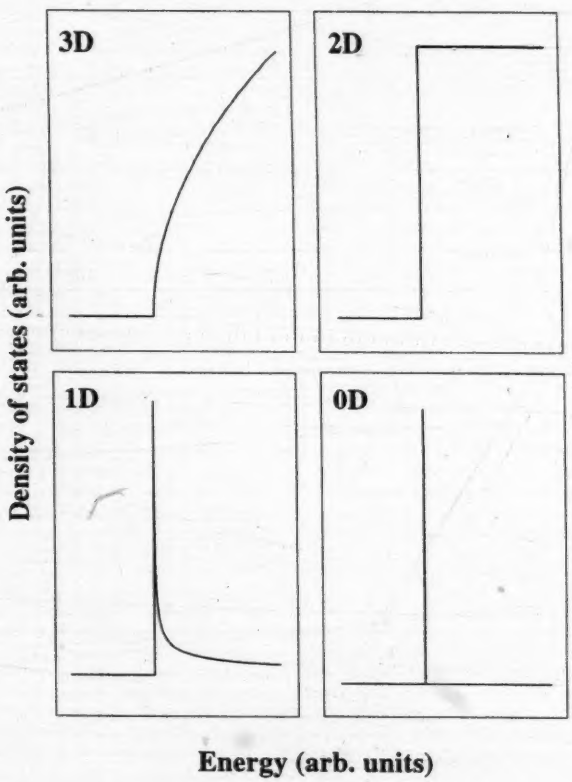

Figure 1.2. The theoretically modeled density of states for a semiconductor of decreasing particle dimension.

Quantum confinement effects in semiconductor nanocrystals emerge when the particle size is decreased to what is referred to as the Bohr exciton radius. The Bohr exciton radius is the spatial extent, or distance between the electron and hole in a given material. It is directly proportional to the dielectric constant of the material (ε) and inversely proportional to the reduced effective mass (μ_0) of the electron and hole ($m_e m_h/(m_e + m_h)$), and is commonly given as $r_{ex} \sim 0.529\varepsilon/\mu_0$, where 0.529 Å is the calculated Bohr exciton radius for hydrogen. [11] The absorption of an optical photon promotes an electron to the conduction band, consequently leaving a vacancy, or hole,

in the valence band. This coulombically bound electron-hole pair is called an exciton. From the above equation it can be seen that the Bohr exciton radius is directly proportional to the dielectric constant and inversely proportional to the reduced exciton mass. To rationalize why quantum confinement effects emerge at different size thresholds for different semiconductor materials, the dependence of Bohr exciton radius on the dielectric constant may be explained in terms of capacitance, where capacitance = ε*area/distance. If the electron and hole are visualized as being separated by a dielectric material of constant area and capacitance, a specific distance would separate the electron and hole. If the dielectric constant of the material between the electron and hole increases, the distance between the electron and hole would also increase. Therefore, an increase in the dielectric constant leads to an increase in the electron and hole distance and consequently an increase in the Bohr exciton radius. Examples of some common semiconductor Bohr exciton radii are shown in Table 1.3.

Table 1.3. The dielectric constants and Bohr exciton radii for common semiconductors

Semiconductor	Dielectric constant (ε)	Effective electron mass[b]	Effective hole mass[b]	Bohr exciton radius[a] (Å)
Silicon	11.4	0.191	0.537	~49
Germanium	15.4	0.081	0.284	~177
Gallium Arsenide	12.4	0.063	0.500	~140

[a]Effective mass approximation, where the Bohr exciton radius is given by $r_{ex} \sim 0.529\varepsilon/\mu_0$, where ε is the dielectric constant of the material and μ_0 is the reduced mass of the electron and hole, $(m_e m_h/(m_e + m_h))$.
[b]Effective masses in units of free electron mass – Effective mass = mass * 9.109×10^{-31} kg. Constants taken from reference 4.

As the particle size approaches its Bohr exciton radius the electron-hole pair experiences an enhanced coulombic interaction referred to as the exciton binding energy. The magnitude of this energy affects the probability of radiative recombination and hence the quantum yield. The binding energy may be enhanced by increasing the reduced mass of the exciton (μ_0) or by decreasing the dimensionality of the semiconductor. Therefore, holding the dielectric material and the exciton reduced-mass constant, a decrease the particle size leads to an increase in the exciton binding energy and a corresponding increase in the quantum yield of the system.

After Canham's quantum confinement explanation of visible room temperature PL from p-Si in 1990, skepticism in the scientific community and the possibility of unique silicon photonic applications resulted in a tremendous interest in the origin of luminescence from p-Si. Between 1990 and 1997 a number of alternative luminescence mechanisms in addition to the quantum confinement mechanism were proposed for p-Si, including, but not limited to adsorbed siloxenes,[12,13] volume defects,[14,15] and surface states.[16] However, a subsequent review published by Canham in 1997 examined[11] and successfully refuted all of these proposals, and provided additional support for the original quantum confinement mechanism. Despite the initial controversy associated with Canham's quantum confinement theory, it is now a well-accepted explanation for the origin of light emission from sub 5-nm silicon nanomaterials.

1.4. Preparation of low dimensional silicon

1.4.1. Physical methods

In light of the proposal that Si-NCs in p-Si give rise to the luminescence, new methods were devised to prepare low dimensional silicon. One method that quickly gained significant favor, due to the readily available infrastructure in the microelctronics industry, was the formation of oxide-embedded Si-NCs using ion implantation.[17] This technique was a direct extension of existing wafer technology and was very similar to well-established procedures employed to dope semiconductor wafers. Ion implantation is a physical method that introduces energetic charged atoms into the surface of a substrate. The formation of oxide-embedded Si-NCs by the ion implantation method first necessitates the formation of a silicon rich oxide (SRO) film. This is typically accomplished by implanting a specific "dose" of silicon ions (i.e., Si^{+} or Si^{2+}) into a layer of thermally grown SiO_2. After the SRO thin film is formed, the substrate is heated in an inert, or slightly reducing atmosphere to promote nucleation of the silicon ions and their crystallization into Si-NCs. This thermal processing step is often referred to as "annealing" in the Si-NC literature. It has been shown that the onset of silicon nucleation occurs between 600 - 750°C and subsequent crystallization begins at approximately 900°C.[18,19] This crystallization process occurs through a solid-state diffusion process in which silicon atoms, with sufficient energy, are able to diffuse through the SiO_2 matrix to form small clusters of elemental silicon.[18-20] Upon cooling, these clusters crystallize to form oxide-embedded Si-NCs. The size of Si-NCs produced by this method are predominantly dependent upon the "fluence" of silicon ions implanted and the peak processing temperature; increasing one or both leads to a larger nanocrystal diameter. This method has been shown to produce luminescent films

containing silicon nanocrystals that emit throughout the visible region of the electromagnetic spectrum;[21] however, the scale-up costs are not amenable to large scale production of Si-NCs.

Thin films of oxide-embedded Si-NCs can also be produced by *in vacuo* thermal and electron beam (e-beam) evaporation. These methods involve the vapor deposition of a solid silicon precursor onto a substrate to produce a SRO thin film that is subsequently thermally processed by a method similar to the annealing procedure outlined above. The formation of these SRO thin films can be accomplished by the reactive evaporation of a silicon target in a controlled oxygen environment. A common variation of this method involves low pressure evaporation of a commercially available SiO_x precursor, where ($0 < X < 2$). While SiO_x has been shown to form Si-NCs its exact composition and homogeneity is still a subject of debate.[23] Recently, Wieder and coworkers monitored the composition of SiO_x in a series of standard deposition and sputtering experiments.[22,23] Figure 1.3 shows the high resolution X-ray photoelectron spectra of the Si 2p region for samples of commercially available SiO_x that were physically abraded and sputtered with argon in ultra high vacuum (UHV) in order to monitor any associated changes in homogeneity. The silicon 2p spectra of all SiO_x samples clearly show the presence of elemental silicon (Si^0) and SiO_2 (Si^{+4}), but the non-zero baseline between these oxide emission peaks indicates there is also a significant amount of intermediate silicon oxides, such as (Si^{+1}, Si^{+2}, Si^{+3}), present. Many of the questions and challenges associated with commercially available SiO_x arise because of the relative concentrations of these intermediate oxides. Precise control of a well-defined silicon oxide species in SiO_x is difficult to achieve. Compounding this

compositional variability are the different evaporation rates of silicon and its oxides. For commercially available SiO_x, which is composed of all silicon oxides, this can cause inhomogeneous deposition of the oxides of silicon. Despite these concerns, deposition and subsequent thermal processing of SiO_x thin films has been successfully used in the production of luminescent oxide-embedded Si-NCs.[24]

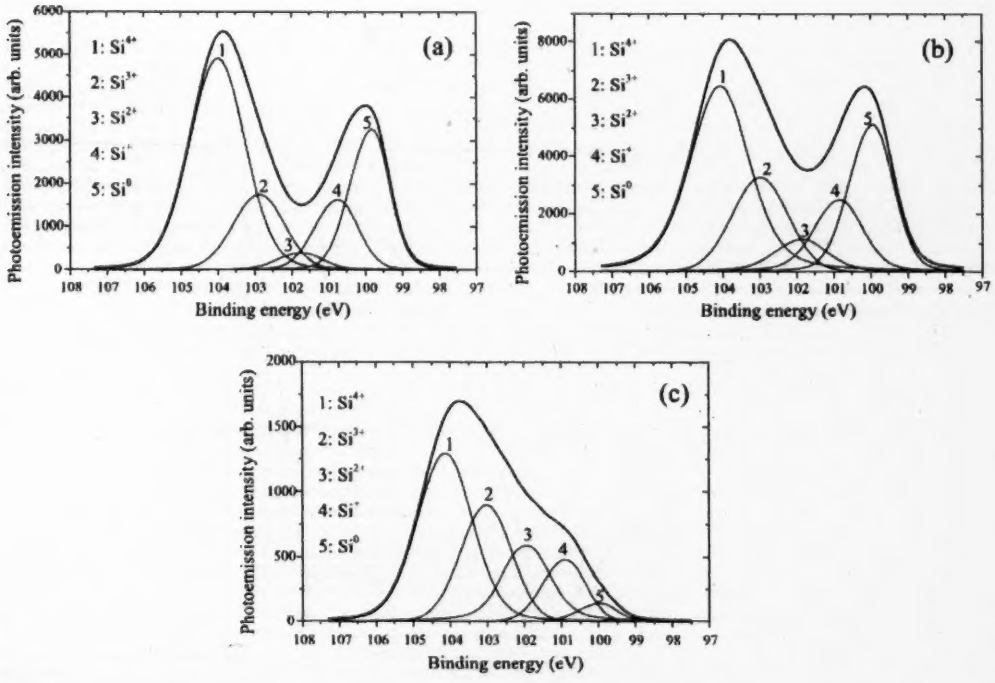

Figure 1.3. Silicon 2p core level spectra of SiO_x ((a) fractured, (b) scratched, (c) sputter-cleaned sample) fitted to five peaks corresponding to different Si oxidation states respectively. Significant amounts of intermediate silicon oxides (Si^{+1}, Si^{+2}, Si^{+3}) are clearly resolved. Figure adapted from reference 21.

The above two physical methods have played integral roles in developing our current understanding of Si-NC formation and their luminescence characteristics. However, in addition to the aforementioned limitations these methods face a number of additional challenges. First, these physical deposition methods rely on line-of-sight techniques, and are not well suited for conformal film formation on non-flat surfaces. Thermal and e-beam deposition, as well as ion implantation, all involve positioning a substrate in the flux stream from an evaporative silicon source to obtain a SRO thin film. Even when in-situ substrate rotation is employed, the underside of non-flat surfaces (i.e., spheres, cylinders) cannot be coated using these methods. This limitation has been clearly demonstrated with the coating of silica sphere optical cavities with oxide-embedded Si-NCs.[25] The e-beam deposition technique used in this investigation only coated the top half of the spheres resulting in a leakage of light out of the non-ideal optical cavity.

The second limitation of these physical deposition techniques is their inability to produce tangible (ca. > 500 mg) amounts of Si-NCs necessary for subsequent applications and fundamental studies. The physical techniques described here can only produce thin films of oxide-embedded Si-NCs. Even when the substrate area is maximized and thick films are grown, the actual yield of Si-NCs remains very small. Although thin film technology encompasses a significant proportion of the photonics industry, using these methods to produce oxide-embedded Si-NCs restricts the true potential of Si-NCs as advanced luminescent materials. Therefore, in order to attain this goal, new solution-based routes were sought to produce tangible amounts of Si-NCs.

1.4.2. Solution-based reduction methods

Solution-based methods to produce Si-NCs free from an encapsulating matrix (i.e., freestanding) offer the possibility to simultaneous control the size, crystal structure, and surface chemistry of Si-NCs. Recent chemical routes of producing freestanding Si-NCs can be organized into two broad categories, 1) solution precursor reduction (both hetero- and homogeneous), and 2) precursor thermolysis and pyrolysis. To date, solution reduction-based routes have received the majority of attention due to their potential for *in situ* chemical modification of the nanocrystal surface. These methods typically rely on reducing a volatile liquid phase silicon precursor, typically $SiCl_4$, with an appropriate reducing agent. Heath *et al.* reported one of the first successful demonstrations of a heterogeneous solution precursor reduction in 1992.[26] The biphasic synthesis involved the simultaneous reduction of $SiCl_4$ and $RSiCl_3$ (R = H and octyl) with a dispersion of sodium metal that was carried out for 3 – 7 days in a high pressure (> 100 atm) bomb reactor with a constant 385°C temperature to afford freestanding Si-NCs. Limited size control of the freestanding Si-NCs was demonstrated by varying the R-group on $RSiCl_3$. Reductions containing $HSiCl_3$ produced 5 – 3000 nm Si-NCs, whereas reductions containing $octylSiCl_3$ produced 5.5 ± 2.5 nm Si-NCs. Although successful, this synthesis is limited in its practicality because of the severe reaction conditions employed. The resulting product also showed a myriad of surface species, Si-H, Si-O, and Si-Cl, indicating a low level of control over the Si-NC surface chemistry. A variation on this procedure was presented by Dhas and coworkers in 1998,[27] involving the reduction of TEOS, ($Si(OCH_2CH_3)_4$), in the presence of sodium at ca. 70°C. The isolated grey product was thermally processed at 400°C in a nitrogen

atmosphere to yield aggregates of Si-NCs ranging in size from 2 and 5 nanometers. Although both Dhas and Heath successfully produced freestanding Si-NCs, their methods have limited practicality and do not lead to size monodisperse nanocrystals with predictable surface chemistry.

Heterogeneous reduction of $SiCl_4$ by Zintl salts (ASi; A = Na, K, Mg) has been shown by Kauzlarich *et al.* to be a viable route to producing small quantities (8 – 85 mg) of freestanding Si-NCs.[28] The first report utilized KSi to reduce $SiCl_4$ in refluxing solutions of glyme or THF to produce black powders containing freestanding 2 – 5 nm Si-NCs. Although FTIR spectroscopy identified characteristic stretching and bending frequencies for Si-O and C-H_{sat}, suggesting methoxy (-OCH_3) surface passivation, subsequent reactivity studies of identical materials suggested that the surface was terminated with Si-Cl bonds. It was concluded that the formation of methoxy-terminated surfaces resulted from methanol addition during the isolation procedure.[29] This seemingly unexpected reaction between methanol and the nanocrystal surface conveniently rendered the nanocrystals hydrophobic, and facilitated straightforward extraction from the reaction byproducts with non-polar organic solvents. The success of this procedure led to the exploration of a number of alkali-metal silicides, including NaSi, and the less reactive Mg_2Si.[28] The experimental modifications necessary for the incorporation of these alternative reducing agents did not significantly alter the resulting products, and luminescent, freestanding Si-NCs were still obtained. In a following report by Lee and coworkers,[30] ultrasonication replaced heat as a means of initiating the reduction of $SiCl_4$ by sodium silicide. This method produced relatively large amounts (120 mg/batch) of size polydisperse (d = 1 – 5 nm) alkyl terminated Si-NCs that

exhibited PL in the visible region of the EM spectrum. In this report it was noted that the PL emission energy and profile were dependent on ultrasonication time, and a narrow blue emission band was realized when the reaction was left for 15 minutes, and a broad white emission band after reaction for 60 minutes.

The initial successes with heterogeneous Zintl salt precursor reductions led to homogeneous reductions of $SiCl_4$. Wilcoxon and Samara showed that in a single phase mixture, $LiAlH_4$ could be used to reduce $SiCl_4$ to Si-NCs in the presence of a surfactant.[31,32] Although yield data were not reported, this procedure gave Si-NCs with a broad size distribution ranging from 2 – 10 nm in diameter. Soon after this report, Tilley was able to fine tune the homogeneous reduction method to produce small and remarkably size monodisperse freestanding Si-NCs ($d = 1.8 \pm 0.2$ nm) stabilized in trioctylammonium bromide (TOAB).[33] Subsequent reactivity investigations involving the attachment of heptene and allylamine indirectly suggested that the surfaces of the *as-prepared* nanocrystals were hydride terminated.

Employing a synthetic strategy similar to the heterogeneous Zintl salt reduction, Kauzlarich *et al.* have also produced freestanding Si-NCs by homogeneous precursor reduction. A homogeneous reducing agent, sodium napthalide, was employed for their synthesis, and work-up procedures follow the heterogeneous approach previously employed by these researchers. Homogeneous reductions involving sodium naphthalide are slightly more versatile than heterogeneous Zintl salt reductions because freestanding Si-NCs with various sizes and surface passivation are produced.[34,35,36] An additional advantage of the sodium napthalide reduction is the ability to control the Si-NC morphology. A slight variation to the synthesis allows for the production of large (40 –

80 nm) silicon tetrahedra.[35] Although these large nanocrystals are not luminescent, this is one of the only reports that demonstrates shape-controlled freestanding Si-NCs.

There was significant progression in the field of hetero- and homogeneous precursor reduction in the years following the first reports of freestanding Si-NCs. The harsh heterogeneous bomb reactions first employed by Heath and Dhas were replaced by single-phase solution syntheses that provided nearly size-monodisperse freestanding Si-NCs with somewhat controlled surface chemistries and crystal morphologies. Literature yield data indicate that these methods do not afford significant amounts (> 500 mg/batch) of material, with the ultrasonication method by Lee having the greatest promise with a product yield of 120 mg/batch. For Si-NCs to achieve their full potential in sensing and emission-based applications it is vital that synthetic procedures be developed to afford multigram quantities of well-defined freestanding Si-NCs. Unlike the aforementioned solution reduction methods, which are limited to small batch sizes, synthetic methods involving precursor decomposition have been shown to produce gram quantities of freestanding Si-NCs.

1.4.3. Percursor thermolysis and pyrolysis

Precursor thermolysis and pyrolysis are among the most widely studied routes toward highly monodisperse nanoparticles. These methods mimic the procedure designed by Bawendi to produce compound semiconductor nanocrystals.[37] They rely on the rapid thermal decomposition of reactive precursors, followed by immediate nucleation and subsequent controlled growth of the nanocrystals. The first method utilizing precursor thermolysis for the production of Si-NCs was reported by Korgel and

coworkers in 2001.[38] This synthesis involved the thermally-induced degradation of diphenyl silane in a mixture of supercritical octanol and hexane to afford 1.5 – 4.0 nm alkoxy-capped, highly luminescent freestanding Si-NCs. Although the batch yield of this procedure was very low (0.07 – 1.4 mg), it did offer control over the average nanocrystal size and distribution. When the silicon to octanol ratio was low, the octanol quickly capped the Si-NCs after nucleation and arrested particle growth, resulting in very small (d = 1.5 nm), yet highly size monodisperse Si-NCs. If the amount of octanol was decreased, the growth of the nanocrystals proceeded uninhibited and larger Si-NCs with broad size distributions were obtained. Like the precursor reduction methods, this synthesis was capable of producing narrow size ranges of freestanding Si-NCs with controlled surface chemistry, although it is only capable of producing milligram quantities of material in a single batch.

One of the most promising methods of producing tangible quantities of freestanding Si-NCs to date involves the laser-induced pyrolysis of silane gas. In 2003, Swihart *et al.,* reported a flow through reactor that combined silane with a slightly reducing stream of hydrogen and helium to produce freestanding Si-NCs with mixed hydride and oxide surface chemistries, at a rate of 20 – 200 mg/hour, a yield previously not seen in the literature.[39] The aerosol synthesis relies on the presence of a gaseous photosensitizer, SF_6, with a large absorption cross-section at the emission wavelength of the CO_2 laser, that provides the necessary energy to pyrolyze the silane gas. Opposing flows of helium and hydrogen in the reactor create a confined zone in which nucleation and particle growth occurs. The freestanding Si-NCs formed by this reaction are ca. 5 nm in diameter, and are collected in the exhaust stream of the reactor as a fine powder.

The *as prepared* Si-NCs do not exhibit photoluminescence, but when exposed to an etching mixture of HF/HNO_3, a bright PL emission in the visible region of the EM spectrum emerges. During the etching process, HF reacts with the surface oxide and exposes the silicon core, at which point the HNO_3 reoxidizes the surface. These processes happen concomitantly and the nanocrystal dimension is slowly decreased to below the Bohr exciton radius. The etching process also eliminates the dangling bonds in the *as prepared* Si-NCs and imparts a hydride surface passivation that renders the resulting Si-NCs highly luminescent. Swihart's method was the first demonstration of methodology producing tangible amounts (500 mg/batch) of freestanding Si-NCs. It offered the working material necessary for fundamental post-synthesis investigations and also increased the potential for Si-NCs in light emitting and sensing applications.

1.5 Silsesquioxanes

The novel Si-NC preparation described in this thesis produces comparable amounts of oxide-embedded Si-NCs with respect to the Swihart synthesis, but relies on the reductive thermal processing of hydrogen silsesquioxane. Silsesquioxanes are a very interesting class of silicon materials that originated from the silicone industry. They were first utilized as electrical insulators for high temperature electronic applications, but have since been replaced by polydimethylsiloxane (PDMS). The term silsesquioxane encompasses all structures with an molecular formula of $R_8Si_8O_{12}$, where R can be hydrogen, aryl, alkyl, arylene, aklylene, or organofunctional derivatives.[40] Hydrogen silsesquioxane (HSQ) is one of the few completely inorganic silsesquioxanes, and can be synthesized in a variety of ladder, chain, and cage

structures. Frye and Collins were the first to synthesize HSQ oligomers by adding benzene solutions containing trichlorosilane to a mixture of concentrated and fuming sulphuric acid.[41] The HSQ molecule with 8 silicon atoms at the corners of a "cube" (Figure 1.4) was isolated in a slightly different manner and involved the dilute-solution hydrolysis of trimethoxysilane in concentrated hydrochloric acid and a mixture of cyclohexane and acetic acid.[41]

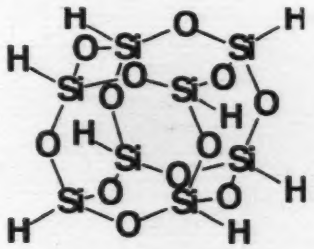

Figure 1.4. The molecular structure of hydrogen silsesquioxane (HSQ)

Although the yield was only 13% in this first report, a significant amount of proprietary research by Dow Corning Corporation has increased this. HSQ is now commercially available from Dow Corning Corporation which produces it via a proprietary procedure and markets it under the trade name FOx – highlighting that it is a solution processable "flowable" oxide. It is currently used as a spin-on dielectric insulator in the microelectronics industry as it provides a highly uniform silica surface when thermally processed at 250 – 300°C in ambient conditions. Close inspection of the empirical formula of HSQ reveals it is a silicon rich oxide. In context of the previous discussion regarding ion implantation and thermal evaporation methods used to form oxide-embedded Si-NCs from SRO thin films, this suggests that HSQ and similar silsesquioxanes should be suitable precursors for Si-NCs.

1.6. Thesis outline

This thesis presents HSQ as one of the most versatile Si-NC precursors to date. The second chapter briefly outlines the motivation for finding a new Si-NC precursor and describes the discovery and preliminary characterization that clearly demonstrates that reductive thermal processing of HSQ produces well-defined ca. 4 nm oxide-embedded Si-NCs. The *as prepared* oxide-embedded Si-NC composites are highly luminescent in the NIR region of the EM spectrum, and HF etching is employed to tailor the PL emission throughout the visible region. Chapter 3 outlines complimentary spectroscopic studies aimed at providing insight into the HSQ decomposition process that ultimately results in nanocrystal formation, while also describing the dependence of Si-NC PL characteristics on processing variables. Chapter 4 is an investigation into the origin of luminescence from Si-NCs. It relies on the relatively new but powerful technique of X-ray excited optical luminescence (XEOL). This investigation conclusively identified quantum confinement effects as a major contributor to the emission characteristics of Si-NCs, but also identified a previously unobserved emission that is attributed to a distinct interfacial species in the transition region between the Si-NC core and the surrounding oxide matrix. The final chapter is a series of proof-of-concept experiments highlighting the potential for HSQ as a thin film Si-NCs precursor for sensing and emission applications.

The many novel compounds synthesized for the present investigation were all based upon the thermal processing of HSQ composites. Systematically varying the heating rate, peak processing temperature, heating profile, and processing gas provided insight into the formation, growth, and electronic structure of the resulting Si-NCs. In

an effort to maintain consistency with respect to sample identification, a universal sample list provides the processing conditions for each HSQ derived sample described here in.

Table 1.4. Universal list of compounds synthesized for the present thesis. The numbering scheme is consistent throughout Chapters 2-4.

Compound	Processing Temperature (°C)	Processing Time (min)
HSQ		
1	300	60
2	400	60
3	500	60
4	600	60
5	700	60
6	800	60
7	900	60
8	1000	60
9	1100	60
10	1200	60
11	1300	60
12	1400	60
13	1100	120
14	1100	300
15	1100	600
16	1100	1440
	Samples etched with 49%HF: Ethanol: Water	
Compound	Etching Ratio	Etching Time (min)
17	1:1:1	30
18	1:1:1	60
19	1:1:1	90
20	1:1:1	120
21	1:1:1	150

1.7. References

(1) Liang, W.; Bockrath, M.; Bozovic, D.; Hafner, J. H.; Tinkham, M.; Park, H. *Nature* **2001**, *411*.

(2) Kong, J.; Yenilmez, E.; Tombler, T. W.; Kim, W.; Dai, H.; Laughlin, R. B.; Liu, L.; Jayanthi, C. S.; Wu, S. Y. *Phys. Rev. Lett.* **2001**, *87*.

(3) McEuen, P. L.; Fuhrer, M. S.; Park, H. *IEEE Transactions on Nanotechnology* **2002**, *1*, 78.

(4) Grahn, H. T. *Introduction to semiconductor physics*; World Scientific: Berlin, 1999.

(5) Madelung, O. *Landolt-Bornstein New Series*; Springer-Verlag: Berlin, Germany, 1987; Vol. III.

(6) Huheey, J. E. *Inorganic chemistry*; Harper and Row: New York, 1983.

(7) Pauling, L. *The nature of the chemical bond*; Cornell university press, 1960.

(8) Round, H. J. *Electrical world* **1907**, *49*, 308.

(9) Dabbousi, B. O.; Rodriguez-Viejo, J.; Mikulec, F. V.; Heine, J. R.; Mattoussi, H.; Ober, R.; Jensen, K. F.; Bawendi, M. G. *J. Phys. Chem. B* **1997**, *101*, 9463.

(10) Canham, L. T. *Appl. Phys. Lett.* **1990**, *57*.

(11) Cullis, A. G.; Canham, L. T.; Calcott, P. D. J. *J. Appl. Phys.* **1997**, *82*, 909.

(12) Deak, P.; Rosenbauer, M.; Stutzmann, M.; Weber, J.; Brandt, M. S. *Phys. Rev. Lett.* **1992**, *69*, 2531.

(13) Brandt, M. S.; Fuchs, H. D.; Stutzmann, M.; Weber, J.; Cardona, M. *Solid State Commun.* **1992**, *81*, 307.

(14) Kanemitsu, Y.; Uto, H.; Masumoto, Y.; Matsumoto, T.; Futagi, T.; Mimura, H. *Phys. Rev. B: Condens. Matter* **1993**, *48*, 2827.

(15) Wang, C.; Gaspari, F.; Zukotynski, S. MRS Proceedings, 1993, San Francisco, CA, USA.

(16) Koch, F. *Microelectron. Eng.* **1995**, *28*, 237.

(17) Shimizu-Iwayama, T.; Hama, T.; Hole, D. E.; Boyd, I. W. *Solid-State Electronics* **2001**, *45*, 1487.

(18) Hofmeister, H.; Kodderitzsch, P.; Dutta, J. *J. Non-Cryst. Solids* **1998**, *232-234*, 182.

(19) Shao, W. L.; Shinar, J.; Gerstein, B. C.; Li, F.; Lannin, J. S. *Phys. Rev. B: Condens. Matter* **1990**, *41*, 9491.

(20) Hofmeister, H.; Dutta, J.; Hofmann, H. *Phys. Rev. B: Condens. Matter* **1996**, *54*, 2856.

(21) Shimizu-Iwayama, T.; Hama, T.; Hole, D. E.; Boyd, I. W. *Solid-State Electron.* **2001**, *45*, 1487.

(22) Hohl, A.; Wieder, T.; Van Aken, P. A.; Weirich, T. E.; Denninger, G.; Vidal, M.; Oswald, S.; Deneke, C.; Mayer, J.; Fuess, H. *J. Non-Cryst. Solids* **2003**, *320*, 255.

(23) Friede, B.; Jansen, M. *J. Non-Cryst. Solids* **1996**, *204*, 202.

(24) Hryciw, A.; Laforge, J.; Blois, C.; Glover, M.; Meldrum, A. *Adv. Mater.* **2005**, *17*, 845.

(25) Beltaos, A. M.; Meldrum, A. *J. Lumin.* **2007**, *126*, 607.

(26) Heath, J. R. *Science* **1992**, *258*, 1131.

(27) Dhas, N. A.; Raj, C. P.; Gedanken, A. *Chem. Mater.* **1998**, *10*, 3278.
(28) Bley, R. A.; Kauzlarich, S. M. *J. Am. Chem. Soc.* **1996**, *118*, 12461.
(29) Mayeri, D.; Phillips, B. L.; Augustine, M. P.; Kauzlarich, S. M. *Chem. Mater.* **2001**, *13*, 765.
(30) Lee, S.; Cho, W. J.; Chin, C. S.; Han, I. K.; Choi, W. J.; Park, Y. J.; Song, J. D.; Lee, J. I. *Jpn. J. Appl. Phys., Part 1* **2004**, *43*, 784.
(31) Wilcoxon, J. P.; Samara, G. A.; Provencio, P. N. *Phys. Rev. B: Condens. Matter* **1999**, *60*, 2704.
(32) Wilcoxon, J. P.; Samara, G. A. *Appl. Phys. Lett.* **1999**, *74*, 3164.
(33) Warner, J. H.; Rubinsztein-Dunlop, H.; Tilley, R. D. *J. Phys. Chem. B* **2005**, *109*, 19064.
(34) Baldwin, R. K.; Pettigrew, K. A.; Ratai, E.; Augustine, M. P.; Kauzlarich, S. M. *Chem. Commun.* **2002**, *8*, 1822.
(35) Baldwin, R. K.; Pettigrew, K. A.; Garno, J. C.; Power, P. P.; Liu, G. Y.; Kauzlarich, S. M. *J. Am. Chem. Soc.* **2002**, *124*, 1150.
(36) Zou, J.; Baldwin, R. K.; Pettigrew, K. A.; Kauzlarich, S. M. *Nano Lett.* **2004**, *4*, 1181.
(37) Murray, C. B.; Norris, D. J.; Bawendi, M. G. *J. Am. Chem. Soc.* **1993**, *115*, 8706.
(38) Holmes, J. D.; Ziegler, K. J.; Doty, R. C.; Pell, L. E.; Johnston, K. P.; Korgel, B. A. *J. Am. Chem. Soc.* **2001**, *123*, 3743.
(39) Li, X.; He, Y.; Talukdar, S. S.; Swihart, M. T. *Langmuir* **2003**, *19*, 8490.
(40) Baney, R. H.; Itoh, M.; Sakakibara, A.; Suzuki, T. *Chem. Rev.* **1995**, *95*, 1409.
(41) Frye, C. L.; Collins, W. T. *J. Am. Chem. Soc.* **1970**, *92*, 5586.

Chapter 2:

Hydrogen silsesquioxane: A molecular precursor for Si-NC/SiO_2 composites and freestanding hydride surface terminated silicon nanocrystals*

---

* A version of this chapter has been published.

Hessel, C. M.; Henderson, E. J.; Veinot, J. G. C. *Chem. Mater.* **2006**, 18, 6139 – 6146.

2.1. Introduction

Silicon nanostructures including porous silicon (*p*-Si),[1] silicon rich oxides (SROs),[2] and freestanding silicon nanocrystals (Si-NCs)[3] have been the focus of intense research because of their unique chemical and optical characteristics. The electronic structure of the bulk silicon provides an indirect bandgap of 1.12 eV with the lowest point of the conduction band and the highest point in the valence band occurring at different coordinates in reciprocal space. This leads to a forbidden bandgap optical transition dipole and limits practical optoelectronic application of bulk silicon because of low photoluminescence intensity and slow carrier dynamics (i.e., long lived excited states). As the dimensions of a semiconductor particle approach the radius of an exciton in the bulk material (ca. 5 nm for Si), the bandgap energy increases and pseudo-continuous bands become discrete energy levels that are populated according to quantum mechanical selection rules. Consequently, quantum confinement effects emerge and photoluminescence blue shifts with decreasing particle size and increases in intensity.[4] Some researchers suggest that the photoluminescence (PL) observed from photo-excited Si nanoparticles arises because the bandgap transition becomes weakly dipole-allowed in this quantum confined size regime.[5] Others claim photoemission originates from the passivation of surface traps present in bulk Si.[6] Regardless of the explanation, a characteristic photoemission maximum at approximately 1.7 eV is seen for many Si-based nanostructures, including the "Si quantum wires" reported by Canham *et al.*,[7] Si-NC/SiO_2 composites,[2] and freestanding Si nanoparticles prepared via solution,[8,9,10] precursor pyrolysis,[11,12] and physical techniques.[13,14,15] The unique optical properties and electrochemical stability of nanoscale elemental Si offer significant potential for a variety

of light emission applications. [16] Furthermore, the biocompatibility of Si and SiO_2 makes these materials potentially useful in sensing applications where toxic,[17] electrochemically active compound semiconductor nanoparticles are impractical.

Measuring the direct effect of Si nanocrystal size on the PL spectrum of Si-NC/SiO_2 composites and freestanding Si-NCs is complicated with interface effects, surface chemistry, and particle interactions playing key roles. [18] This complexity is well illustrated by the optical response of ultrasmall Si particles (d ~ 1.1-1.4 nm).[19] The experimental optical behaviour of hydride surface terminated freestanding Si-NCs of this size is dominated by blue emission and reports suggest either a direct or indirect gap transition.[20,21] This is very different from observations previously noted for oxide terminated particles of equivalent size that show a red-yellow emission resulting from an indirect gap transition.[22] Very similar observations were reported by Wolkin *et al.* for blue emitting hydride surface terminated nanocrystals in *p-Si* whose PL maximum red shifted upon oxidation.[23] These data appear to contradict *simple* quantum confinement because the decrease in Si particle core size resulting from oxidation seems to cause the PL maximum to decrease in energy. To aid in our understanding of these complex optical properties, diverse theories for relating PL energy maxima to particle size have been proposed, including: the effective mass approximation,[24] empirical tight binding band theory,[25,26] empirical pseudopotential approximation,[27,28] and *ab-initio* local density approximation.[29,30] Still, the size effects and the influence of the indirect bandgap of bulk Si on the PL behavior of Si-NCs remains the subject of much controversy and scientific curiosity.

To facilitate a better understanding of the freestanding Si-NC optical and chemical response, straightforward, cost-effective, scalable methods for preparing materials of controlled polydispersity, size, crystal structure, and surface chemistry are necessary. Well-established physical techniques for preparing Si nanostructures often employ highly corrosive reagents (e.g., hydrofluoric acid), and specialized, highly technical procedures (e.g., ion implantation,[31,32] vacuum evaporation,[33] sputtering,[34] and laser ablation[35]). While freestanding particles have been dislodged from *p*-Si surfaces,[36] published data suggest individual Si nanoparticles remain trapped in larger (i.e., ≥ 1μm) pieces of the *p*-Si structure and that these methods are impractical for preparing macroscopic sample sizes (ca. > 500 mg).[13,14,15] Similar particle liberation protocols and bulk preparation of Si nanoparticles from traditional thin film SRO matrices are impractical given extremely small sample sizes.[37] To this end, a series of methods has been introduced for preparing freestanding Si-NCs. Laser induced precursor pyrolysis has recently been reported as an efficient method for preparing large quantities of Si nanoparticles from silane at rates of 20-200 mg/hour. This approach relies on specialized laser equipment and custom designed reactors not available in most synthetic laboratories.[11,12] Solution-based procedures[10,38,39,40,41,42,43,44,45] provide some post synthesis material processability, but are often plagued by wide size distributions, specialized reagents, small sample sizes, material purity, ill-defined particle surface chemistry, and limited ambient stability – all criteria crucial to the eventual application of these materials.

SROs remain a promising class of nanostructured materials composed of luminescent, crystalline Si nanoparticles embedded in an environmentally inert SiO_2-like

matrix. To date, one major limitation to their application in the synthesis of freestanding Si-NCs has been limited sample size (*vide supra*). One common method for preparing SROs employs a multi-step process; the first stage involves deposition of thin "SiO" precursor films using physical methods such as vapor deposition, physical sputtering, or e-beam evaporation to deposit films onto flat substrates.[2] These recipe-based approaches control the Si:O ratio by maintaining a specific oxygen flow rate (i.e., partial pressure) during reactive deposition of "SiO" or by controlling the co-deposition rates of Si, "SiO", and SiO_2 to produce SiO_x films ($0 \leq x \leq 2$).[46] Films are subsequently annealed at high temperature in a reducing atmosphere (typically 4% H_2, 96% inert gas) to promote the formation of Si-NCs.[47] Iterative variation of experimental parameters and post deposition micro-probe analyses have previously shown that precursor films with compositional ratios close to $Si_{1.0}:O_{1.5}$ produce the strongest PL upon annealing at ca. 1100°C. Still, fundamental questions remain regarding the mechanism for nanoparticle formation, the relationship between Si particle size and peak PL energy, among others.[2] Unfortunately, the *exact* composition, structure, and purity of "SiO" is the subject of a longstanding controversy and are strongly dependent upon processing conditions.[48,48,49] Further, the exact chemical structure of "SiO_x" remains largely ill-defined.[50] These uncertainties potentially hinder the rational study of chemical composition and its influence on the material properties of SRO nanoparticle composites.

Silsesquioxanes are commercially available, solution processable, discrete, structurally well-defined molecules composed of silicon-oxygen frameworks with empirical formulae ($RSiO_{1.5}$) where R may be a variety of chemical functionalities (e.g., H, alkyl, silyl, and aromatic). The chemistry of these compounds is well-established and

a variety of cage structures are known.[51] Hydrogen silsesquioxane (**HSQ**, Scheme 2.1), a totally inorganic silsesquioxane ($H_8Si_8O_{12}$), is one of the most widely studied and has been investigated as a model silica surface,[52,53,54,55] luminescent material,[56] and a catalytic support.[57,58] Examples of high purity silica have also been prepared from silsesquioxane precursors.[59] It is generally accepted that upon *oxidative* thermal curing, the silsesquioxane cage structure of **HSQ** collapses to release SiH_4[60] and a SiO_2-like network solid forms whose dielectric,[61] mechanical, and processing characteristics depend on the curing conditions. Dielectric films produced by thermal curing of **HSQ** currently find application as spin-on, planarizing dielectric interlayers in the microchip industry.[62] To date, no Si nanoparticle preparation employing silsesquioxanes has been reported. The similar composition (i.e., $Si_{1.0}$:$O_{1.5}$) and thermodynamic instability of both **HSQ** and the "ideal" SiO_x precursor films suggest **HSQ** may be a suitable molecular precursor to Si-NC/SiO_2 composites upon *reductive* thermal curing. In addition, the structural tunability of **HSQ** should offer control over film composition and structure previously unattainable using existing physical methods for SiO_x film preparation. Here we report the application of **HSQ** as a molecular precursor for the straightforward large scale (ca. 0.25 g) synthesis of Si-NC/SiO_2 composites and the corresponding liberation of freestanding Si-NCs that are photoluminescent throughout the visible spectrum.

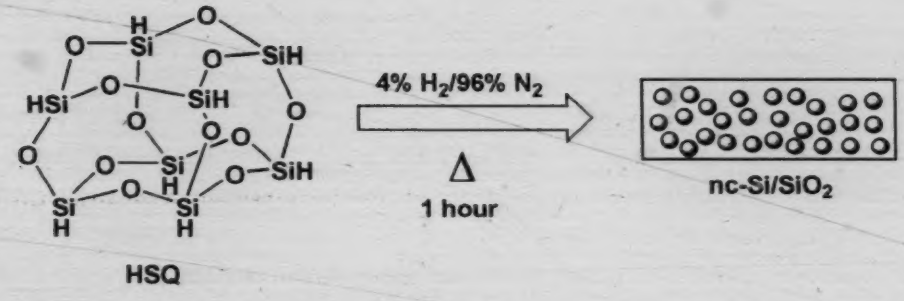

Scheme 2.1. Thermal processing of hydrogen silsesquioxane (**HSQ**) to produce silicon nanocrystal/SiO_2 (**Si-NC/SiO_2**) nanocomposites.

2.2. Experimental Details

2.2.1. Reagents and Materials

HSQ was purchased from Dow Corning (tradename FOx-12®) as a 10 weight percent solution in methyl isobutyl ketone. This stock solution was used as received and stored in subdued light and inert atmosphere prior to use. Electronic grade hydrofluoric acid (49% aqueous solution, J. T. Baker), HPLC grade pentane (Caledon Laboratory Chemicals), and reagent grade ethanol (95%, Sigma-Aldrich) were used as received. High purity water (18.2 MΩ/cm) was obtained from a Barnstead Nanopure Diamond purification system.

2.2.2. Bulk Si-NC/SiO_2 Composite Preparation (3-9)

Solvent was removed from the **HSQ** stock solution. The resulting white solid was placed in a quartz crucible and transferred in inert atmosphere to a high temperature furnace and annealed for one hour in a 4% H_2 and 96% N_2 atmosphere. In the furnace, **HSQ** samples were heated at 18°C/min until the desired peak temperature was reached at which time the samples remained at 500, 600, 700, 800, 900, 1000, or 1100°C for 1 hour.

After cooling to room temperature, the darkened solid was removed and mechanically ground in a mortar and pestle to yield a fine powder whose color varied with processing temperature (See, Figure 2.1 and Table 2.1). To increase particle size uniformity and facilitate more efficient etching, the powder was shaken with glass beads using a wrist action shaker, suspended in distilled water and collected by vacuum filtration with Whatman #2 filter paper. The product yields depend slightly on processing temperature and are summarized in Table 2.1.

Table 2.1. Samples of hydrogen silsesquioxane (HSQ) processed at specified temperatures for 1 hour in 4% H_2/96% N_2. All samples were processed with a heating rate of 18°C/min.

Compound	Processing Temperature (°C)	Colour	Yield (%)	Nanocrystalline (yes/no)
3	500	orange	96	no
4	600	orange	95	no
5	700	orange/brown	94	no
6	800	orange/brown	94	no
7	900	brown/black	94	no
8	1000	brown/black	94	yes
9	1100	brown/black	94	yes
69[a]	800,1100	orange/brown, brown/black	94,94	no,yes

[a] Sample 69 was thermally processed at 800°C for 1 hour (Sample **6**), cooled to room temperature, and subsequently reprocessed to 1100°C for 1 hour(Sample **9**). The sample was under an atmosphere of 5%H_2/95%Ar for both thermal processing cycles.

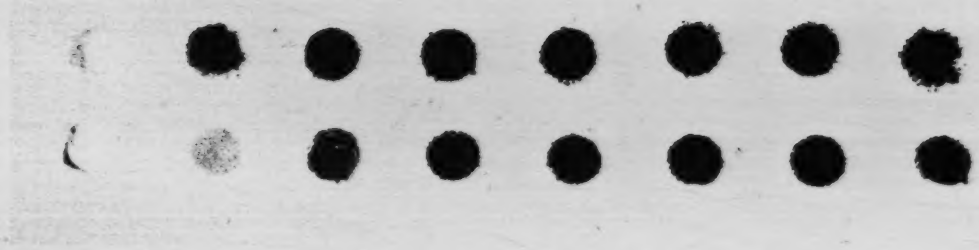

Figure 2.1. Photographs of **HSQ**, **3-9** (left to right) as prepared (top) and finely ground (bottom).

2.2.3. Liberation of Hydride Surface-Terminated Freestanding Si-NCs (17-21)

A representative etching procedure involves transferring 0.3 g of the ground **9** to a Teflon beaker containing 10 mL of a 1:1:1 49% HF : H_2O : ethanol solution. The mixture is stirred for 1.5 hours to remove the silica matrix to yield 0.03 g of **18** as a yellow powder. Once liberated, the hydrophobic, hydride terminated Si-NCs are extracted into two 5 ml portions of pentane and kept under inert atmosphere. Etching parameters for **17-21** are summarized in Table 2.2. This etching procedure is fully scalable.

Table 2.2. Etching parameters and luminescence information for samples of **9** etched for specified times in solutions of 1:1:1 49% HF : H_2O : ethanol.

Compound	Etch Time‡ (min)	Apparent PL Colour	PL Maximum (nm)	Quantum Yield Standard
17	30	N/A –partially etched	N/A	N/A
18	60	Red	705	$[Ru(bpy)_3]Cl_2$
19	90	Orange	812	$[Ru(bpy)_3]Cl_2$
20	120	Yellow	585	rhodamine 590
21	150	Green	512	fluorscein

‡ Etch times strongly depend on reagent concentrations and nanocomposite particle size.

2.2.4. Thermogravimetric Analysis

Thermogravimetric analysis (TGA) was performed using a Perkin Elmer Pyris 1 TGA equipped with Pyris Thermal Analysis 7.0 software. **HSQ** samples were placed in a Pt pan and heated in N_2 or 4% H_2 : 96% N_2 atmospheres from room temperature to 1100 °C at 10, 20, 50, 100 °C/min

2.2.5. X-ray Photoelectron Spectroscopy (XPS)

A Kratos Axis Ultra instrument operating in energy spectrum mode at 210 W was used for XPS measurements. The base pressure and operating chamber pressure was maintained at $\leq 10^{-7}$ Pa. A monochromatic Al K_α source was used to irradiate the samples

and the spectra were obtained with an electron take-off angle of 90°. Wide survey spectra were collected using an elliptical spot with 2 mm and 1 mm major and minor axis lengths, respectively, and 160 eV pass energy with a step of 0.33 eV. Sample compositions were determined from the peaks of the survey spectra with subtracted linear background using the internal instrument values of relative sensitivity factor. Depth profiling was carried out using a differential Ar^+ plasma system operating at $P = 5x10^{-8}$ Torr, $I_{emission}$ = 10 mA, Accelerating Voltage = 4 KeV. Sample charging was minimized using an electron gun.

2.2.6. Material Characterization and Instrumentation

Photoluminescence (PL) spectra of a thin film of finely powdered **9** drop-coated onto optical grade silica from a pentane suspension were evaluated at room temperature using the 325 nm line of a He-Cd laser excitation source and emission was detected with a fiber-optic digital charge coupled device (CCD) spectrometer whose spectral response was normalized using a standard black-body radiator. PL spectra of cloudy pentane solutions of **18-21** were obtained using a Cary Eclipse Fluorimeter. PL quantum yields were calculated by normalizing to appropriate standards.[62] Fourier-transform infrared spectroscopy (FTIR) of pentane cast films of **9,18-21** was performed using a Nicolet Magna 750 IR spectrophotometer. Transmission electron microscopy (TEM) and energy dispersive x-ray (EDX) analyses were preformed using a JEOL-2010 (LaB_6 filament) electron microscope with an accelerating voltage of 200 keV. The cross-sectional TEM sample was prepared by mounting a thin film of oxide-embedded Si-NCs onto a copper grid with a 400 μm diameter hole. The film was subsequently thinned by mechanical

polishing on a grinding wheel, followed by ion milling to perforation. TEM images were obtained from the edge of the milled hole where electron transmission was adequate. TEM samples of the liberated, freestanding Si nanoparticles were dropcoated from a pentane suspension onto carbon coated copper grids. Bulk crystallinity of Si-NC/SiO_2 composites was evaluated using an INEL XRG 3000 x-ray diffractometer equipped with a Cu K_α radiation source.

2.3. Results and Discussion

Hydrogen silsesquioxane or **HSQ** is commercially available from Dow-Corning Corporation under the tradename FOx-("XX") where "XX" is a numeric notation describing the solution formulation (i.e., solvent and concentration). **HSQ** is currently marketed as a "flowable oxide" for use as a spin-on dielectric in the semiconductor industry. Here we report that when **HSQ** is thermally processed in a 4% H_2 : 96%N_2 atmosphere, the white solid transforms into an amber-like solid whose color and crystallinity depend on the peak processing temperature (Figure 2.1). TEM, SAED, XPS, and photoluminescence spectroscopy support XRD observations confirming reductive thermal processing of **HSQ** at 1100°C yields luminescent, diamond structure, elemental silicon nanocrystallites encapsulated in an SiO_2-like matrix (*vide infra*). Matrix embedded Si-NCs are readily liberated upon exposure to hydrofluoric acid solutions that preferentially etch away the SiO_2, leaving freestanding, highly luminescent Si-NCs with emission maxima that are readily tuned throughout the visible region of the electromagnetic spectrum.[63]

2.3.1. Thermogravimetric Analysis

Thermal processing of **HSQ** was evaluated using thermogravimetric analysis (TGA) (Figure 2.2). In a nitrogen atmosphere, thermal traces of **HSQ** obtained at a heating rate of 10°C/min show four distinct regions of weight loss (ca. 50-225 °C ; 1.8%, 225-375 °C ; 2.1%, ca. 375-425°C ; 0.8%, ca. 507°C ; 48%). With increased heating rate (i.e., 10, 20, 50, 100 °C/min) we note a dramatic decrease (Figure 2.3) in the observed weight loss at 507°C (i.e., 10 °C/min, 48% vs. 100°C/min, 5%). TGA analysis of **HSQ** in 4%H_2: 96%N_2 shows ca. 5% weight loss regardless of heating rate.

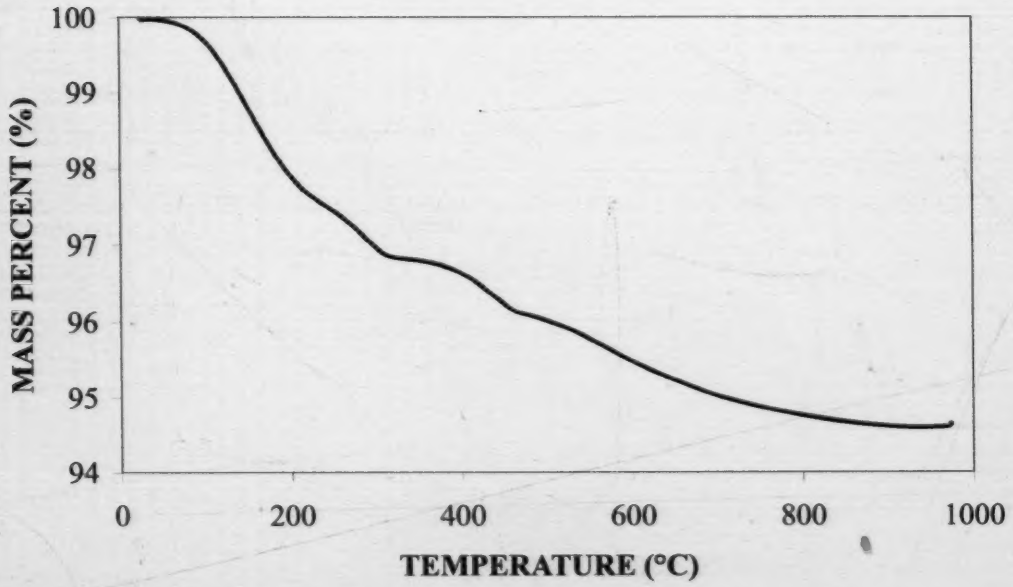

Figure 2.2. Thermogravimetric analysis of HSQ heated at 10°C/min in 4% H_2 : 96% N_2 atmosphere.

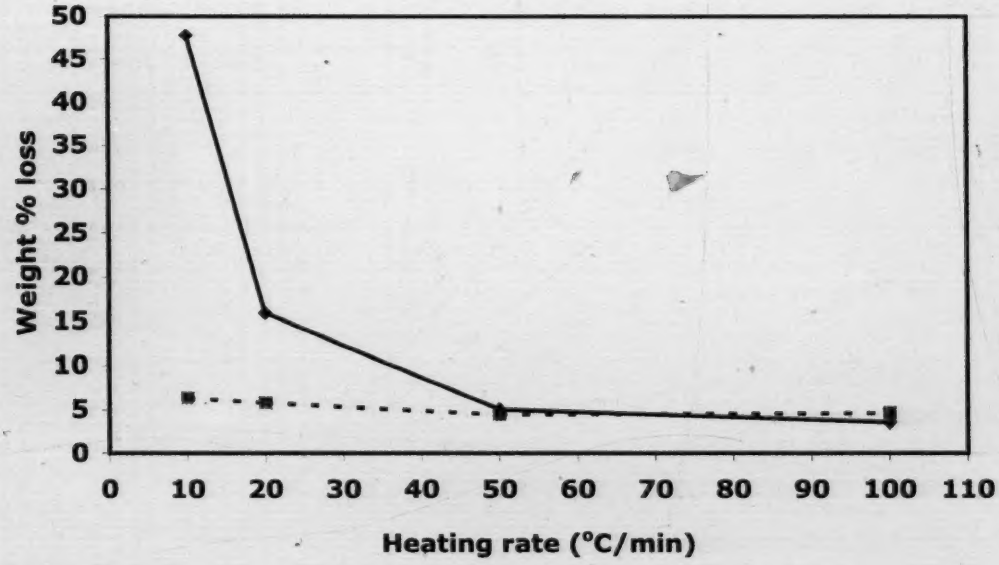

Figure 2.3. Heating rate dependence of **HSQ** weight loss between 25°C and 1000°C. Solid: nitrogen atmosphere. Dashed: 4% H_2 : 96% N_2 atmosphere.

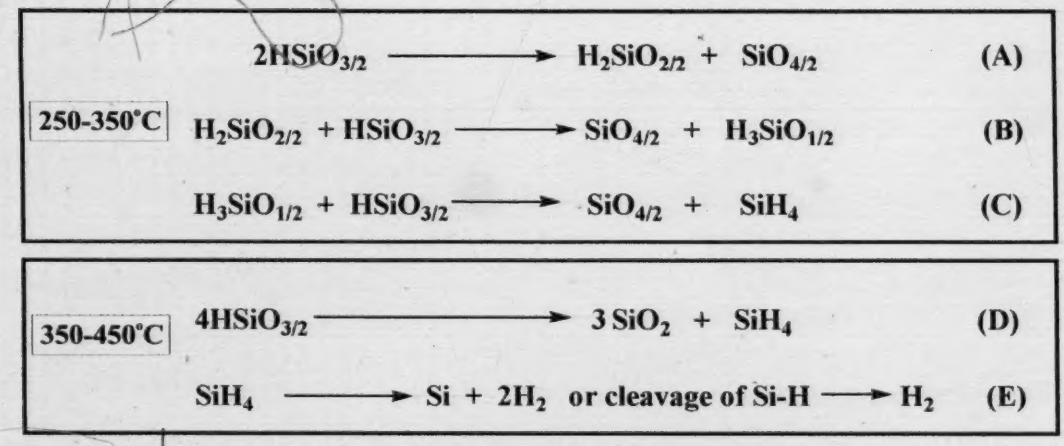
2HSiO3/2 → H2SiO2/2 + SiO4/2 (A)
250-350°C
H2SiO2/2 + HSiO3/2 → SiO4/2 + H3SiO1/2 (B)
H3SiO1/2 + HSiO3/2 → SiO4/2 + SiH4 (C)
350-450°C
4HSiO3/2 → 3 SiO2 + SiH4 (D)
SiH4 → Si + 2H2 or cleavage of Si-H → H2 (E)

Scheme 2.2. Stages of **HSQ** thermal degradation in an inert atmosphere.

The accepted stages of **HSQ** thermal processing in inert atmosphere (i.e., N_2 or Ar) are summarized in Scheme 2.2 and have previously been attributed to: i) trace solvent loss (< 200 °C), ii) cage network redistribution with associated loss of SiH_4 (ca. 250-350 °C), iii) Si-H thermal dissociation accompanied by loss of SiH_4 and H_2 (350-450 °C), and iv) collapse of the pore structure (> 450 °C).[64] The structures of low temperature (i.e., 250°C-350 °C) thermally processed **HSQ** thin films have been studied spectroscopically, but the identity of any gas byproducts remains unknown. This is not the case for high temperature region of the TGA for which the loss of SiH_4 and H_2 has been confirmed by mass spectrometry.[65] Consistent with our nitrogen atmosphere TGA observations, Belot *et al.* noted a decrease in SiH_4 evolution and weight loss at 507 °C with increased heating rates and *proposed,* in the absence of definitive evidence, this resulted from the rapid thermal decomposition of SiH_4 into silicon and hydrogen.[66] Herein, we confirm that the observed trend in weight loss at ca. 450 °C, with increased heating rate, indeed results from the thermal decomposition of SiH_4 and the formation of amorphous clusters of

elemental Si (*vide infra*). Upon rapid heating of **HSQ** (i.e., ≥ 50 °C/min under N_2 or ≥ 10 °C/min under 4% H_2 : 96% N_2) thermally liberated SiH_4 is unable to escape the rapidly forming silicon oxide matrix prior to decomposing.

Currently, the specific role of hydrogen in the thermal processing atmosphere is unclear and is subject to further investigation in our laboratory. One possible explanation for the decreased weight loss may be H_2-induced modifications to the **HSQ** decomposition mechanism (Scheme 2.2E). It is conceivable that low H_2 concentrations in the thermal processing atmosphere limit, and may even prevent the dehydrogenation of **HSQ** thereby increasing the SiH_4 available for thermal decomposition.

2.3.2. X-ray Powder Diffraction (XRD)

The crystallization of oxide-embedded Si-NCs was evaluated by XRD (Figure 2.4). Analyses of composites **3-6** indicate that when **HSQ** is processed at temperatures below 800°C, only a broad unassigned diffraction peak arising from the amorphous SiO_2-like matrix is observed and there are no characteristic reflections of diamond structure Si. When **HSQ** is thermally processed at 900°C (i.e., **7**) weak, very broad diffraction signals corresponding to the (220) and (311) reflections are discernable above the XRD baseline indicating the formation of short-range nanocrystalline order (Table 2.1). The (220) and (311) peaks increase in intensity and narrow while a characteristic (111) reflection becomes prominent for composites processed at higher temperatures (i.e., **8** and **9**). An estimate of the average nanocrystal size can be attained using the Scherrer equation, a relationship which relates spectral peak broadening in XRD to average crystal size (Equation 2.1).

$$D = \frac{0.9\lambda}{B\cos\theta_B}$$

Equation 2.1: Scherrer equation.

$$B = FWHM_{Total} - FWHM_{Insturment}$$

Equation 2.2: Isolation of size related instrumental broadening from total broadening and instrumental broadening.

By this relationship the diameter of the crystal (D) is related to the wavelength of the X-ray photon source (λ = 0.154 nm for Cu) and the size related spectral broadening (B), in radians. The broadening is measured at an intensity equal to half the maximum intensity, typically referred to as the full with at half maximum, FWHM. In order to isolate the size related spectral broadening (B) from the total spectral broadening ($FWHM_{Total}$), the instrumental broadening ($FWHM_{Instrument}$), obtained by measuring the spectral broadening of a bulk standard, is subtracted (Equation 2.2). The utilization of the Scherrer relationship is however applicable to sufficiently small crystals that have an appreciable amount of size induced crystal strain. It has been previously shown that this XRD analysis is a proven method to obtain accurate crystal diameters for a variety of materials in the nanometer size regime, however, the size related XRD spectral broadening becomes negligibly small for crystals greater than 100 nm.[66,67,68,69] As such, particles with dimensions greater than 100 nm can be more accurately characterized by electron microscopy.

Employing the Scherrer relationship to the broadened (311) reflection obtained from the XRD of **9,** a crystallite size of ca. 4 nm was obtained. The positions and intensities of all broadened reflections agree with the selected area electron diffraction obtained for composite **9** and are consistent with diamond structure Si. Samples thermally processed at lower temperatures (i.e., **3-6**) can be reprocessed at 1100°C to produce similar nanocrystalline domains observed for composite **9** (Figure 2.5A). HF etching of **9** yields freestanding Si-NCs (*vide infra*). XRD patterns of the freestanding Si-NCs show no broad diffraction arising from the amorphous composite matrix while the peaks characteristic of diamond structure Si remain (Figure 2.5B).

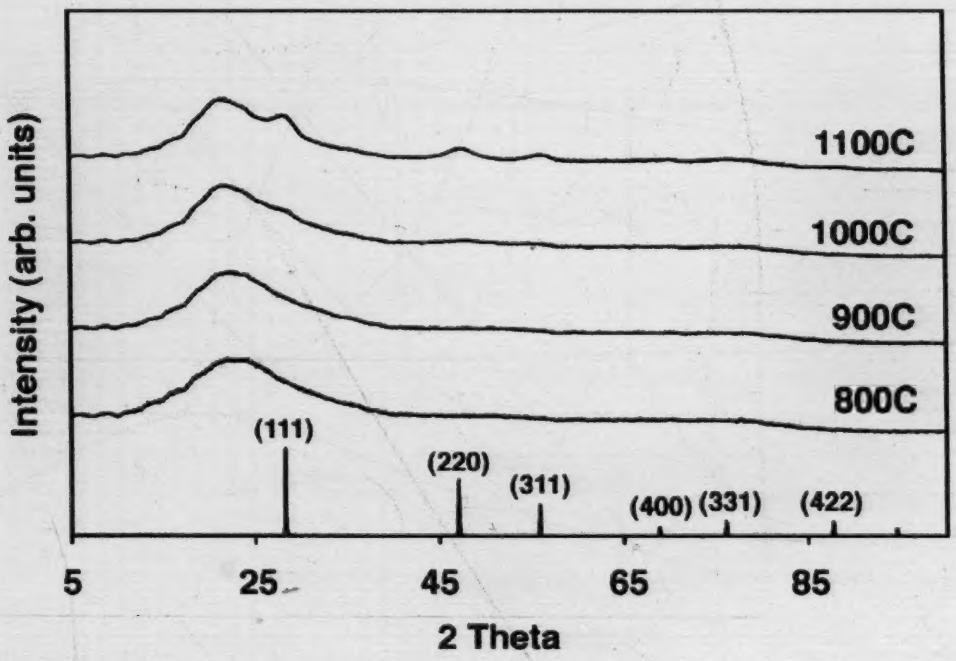

Figure 2.4. X-ray powder diffraction of composites **6-9** showing the peak thermal processing temperature dependence of Si nano-domain crystallinity. Characteristic reflections of a silicon powder standard presented for comparison.

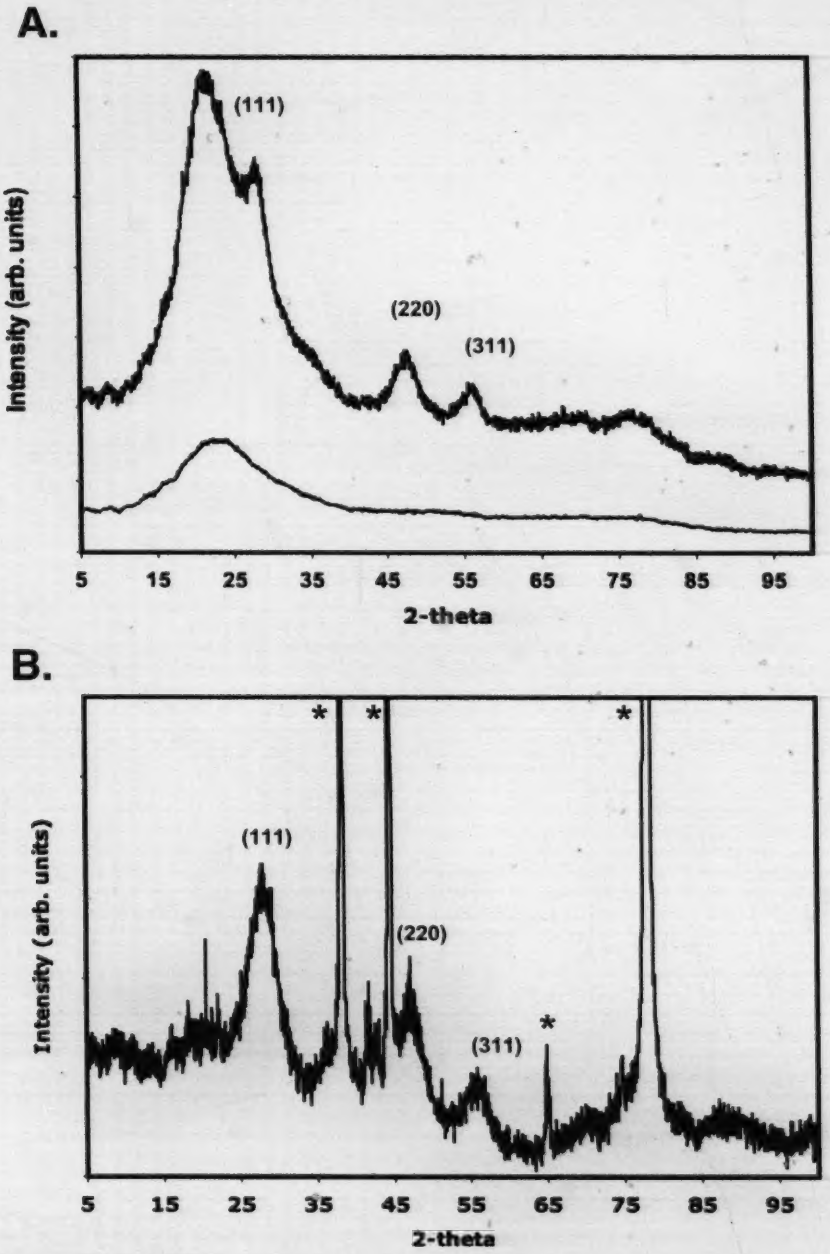

Figure 2.5. A. X-ray powder diffraction of composites **6** (bottom) and **9** (top). Characteristic (111), (220), and (311) reflections of diamond structure are noted. **B.** X-ray powder diffraction of **18**. Characteristic (111), (220), and (311) reflections of diamond structure and sample holder background peaks (*) are noted.

2.3.3. X-ray Photoelectron Spectroscopy

Survey XPS analyses of **6**,**9** confirm the presence of only silicon and oxygen. High resolution scanning of the Si 2p region for composites **6** and **9** show two peaks at approximately 101.9 and 98.1 eV, readily assigned to oxides of silicon and elemental silicon, respectively (Figure 2.6). The ratio of oxide and elemental Si 2p emission peaks is independent of thermal processing temperature suggesting the formation of a constant amount of elemental Si regardless of thermal processing temperature.

The TGA, XRD and XPS data support a multi-step thermal decomposition mechanism that produces Si-NCs. Thermal processing of **HSQ** produces silane. At rapid heating rates (e.g., ≥ 18°C/min in 4%/H_2) silane decomposes and yields non-crystalline clusters of elemental silicon that subsequently crystallize when heated above ca. 900°C. Similar crystallization processes have been reported for SiO_x composites.[70]

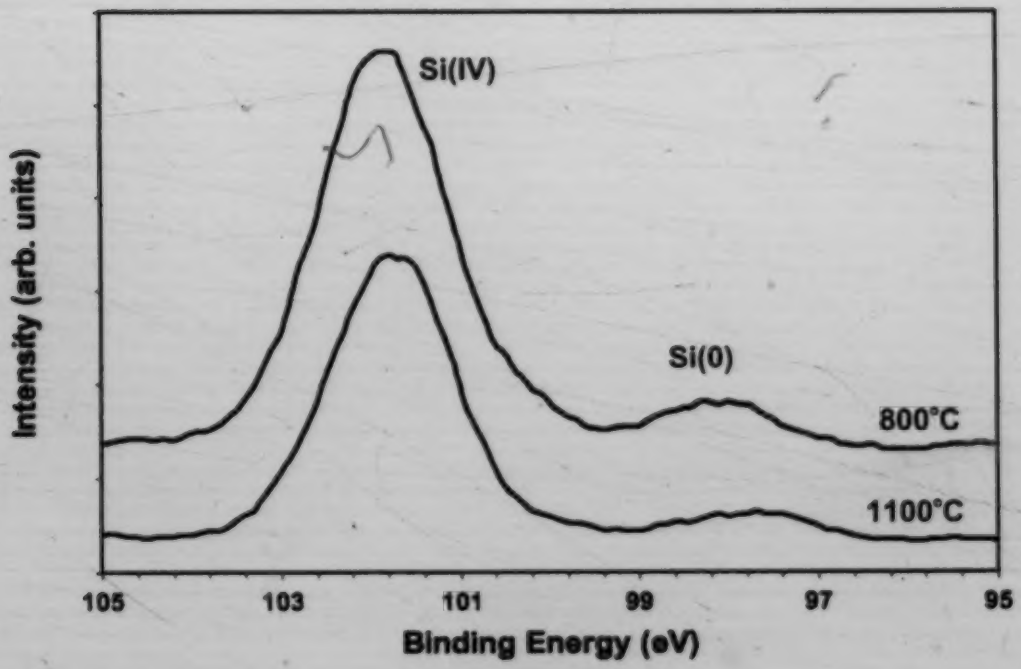

Figure 2.6. High-resolution X-ray photoelectron spectroscopy of the Si 2p spectral region of composites **6** (top) and **9** (bottom). Discernable features with binding energies consistent with SiO_2 and elemental silicon are noted for both samples.

2.3.4. Fourier Transform Infrared Spectroscopy

FT-IR spectroscopy of NEAT **HSQ** shows a characteristic absorption at 2251 cm^{-1} that is readily assigned to Si-H stretching (Figure 2.7A).[71] Absorptions are also noted in the range of ca. 1300 to 800 cm^{-1} and have previously been assigned to internal vibrations of the Si-O-Si cage framework.[72] Following reductive thermal processing at or above 500°C the absorption arising from Si-H stretching disappears suggesting the **HSQ** molecules have crosslinked and the cage structure has collapsed (See: Figure 2.7B). We also observe the replacement of broad **HSQ** Si-O-Si vibrations with a broad featureless absorption centered at ca. 1096 cm^{-1} that we assign to Si-O-Si bending in an SiO_2-like network. Figure 2.7C shows a typical FT-IR spectrum of a pentane cast film of **17**. Reappearance of the characteristic $Si-H_x$ stretching at 2100 cm^{-1} is consistent with at least partial hydride termination of the particles. Bending frequencies of the Si-O-Si bonding configuration at $\leq$ 1400 cm^{-1} remain a dominant spectral feature in this spectrum indicating incomplete liberation. As expected, a marked decrease in the intensity of the Si-O-Si absorptions is noted with increased HF etching time. A representative FT-IR spectrum of fully etched, hydride surface terminated silicon particles (**21**) showing characteristic Si-H stretching and bending frequencies is shown in Figure 2.7D. A very weak Si-O-Si vibration is present in this spectrum and likely results from limited surface oxidation that occurs during sample preparation.[73] Weak C-H stretching and bending frequencies arising from residual pentane are also observed.

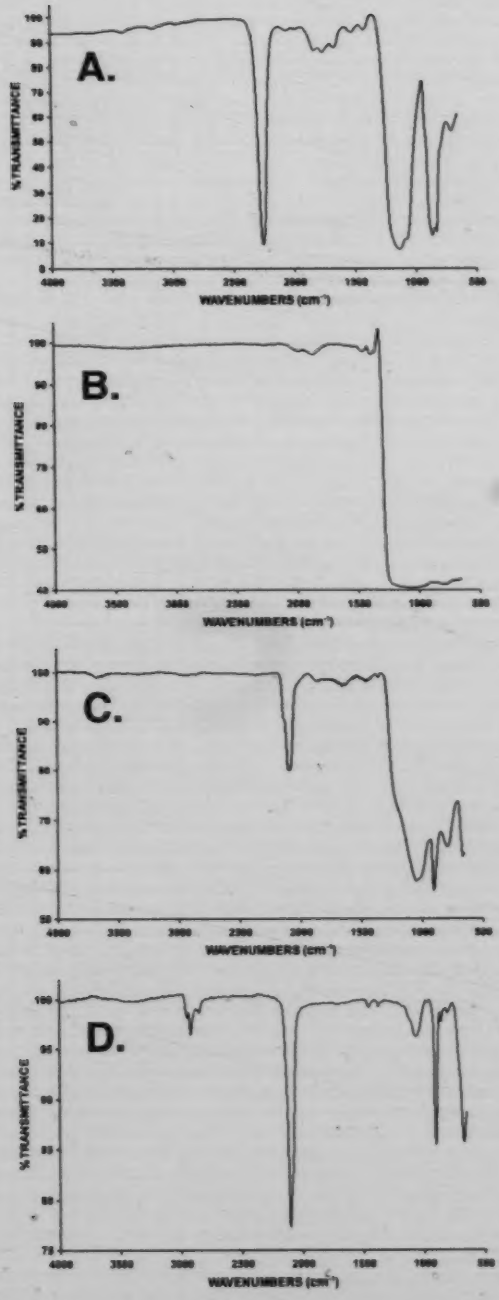

Figure 2.7. Infrared spectra of A) NEAT hydrogen silsesquioxane B) HSQ processed at 1100°C, Sample **9** C) Samples of annealed HSQ (Sample **9**) etched with HF for: C) 60 minutes, Sample **18** D) 120 min, Sample **20.**

2.3.5. Photoluminescence Spectroscopy

HSQ shows no visible photoluminescence. Composites **3-6** exhibit no detectable photoluminescence upon exposure to a standard handheld UV-light. However, excitation with the 325 nm line of a He-Cd laser yields characteristic Si-NC/SiO_2 emission at ca. 800 nm from a solid film of **9**. (Figure 2.8). Upon etching with an HF solution, silicon crystals are liberated from the oxide matrix and become highly luminescent. The emission maxima of these isolated nanocrystals depend on the etching time (Figure 2.9). The observed blue shift in PL maximum upon extended exposure to HF is consistent with previous reports for etched Si-NC/SiO_2 nanocomposites and can be attributed to quantum confinement effects arising from decreased particles size. External photoluminescent quantum yields of isolated, hydride surface terminated Si particles are approximately 0.04 consistent with those reported for similar systems in hydrocarbon solvents.[21,74] Still, light scattering from the characteristically cloudy solutions of hydride terminated freestanding Si-NCs limit quantitative interpretation of this data.

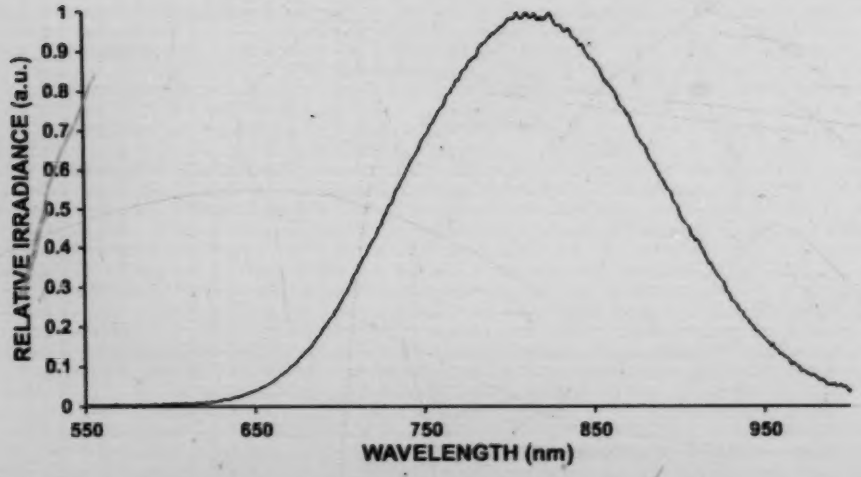

Figure 2.8. Photoluminescence spectrum obtained upon excitation of a thin film of **9** dropcoated from a pentane suspension of the finely ground powder onto optical grade silica using the 325 nm line of a He-Cd laser.

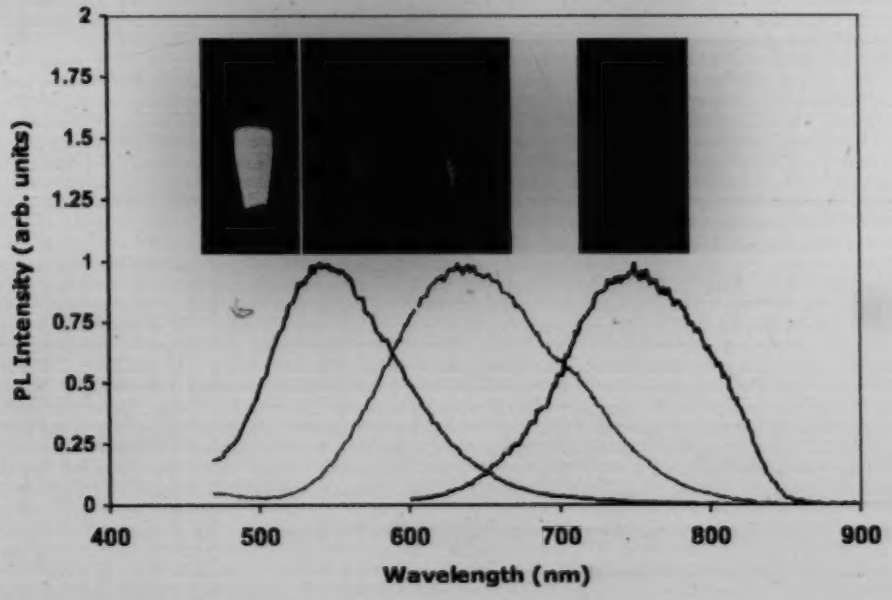

Figure 2.9. Photoluminescence spectra of pentane suspensions of **18** (red), **19** (orange), **20** (yellow), and **21** (green). Inset: Photographs of photoluminescence observed from pentane suspensions of **18 – 21** upon exposure to a standard handheld UV light.

2.3.6. Transmission Electron Microscopy, Energy Dispersive X-ray Spectroscopy and Selected Area Electron Diffraction

Figure 2.10 shows a representative bright field TEM image of a mounted piece of **9** that has been ion milled to perforation. This image shows irregular Si-NC particles. It can be concluded that silicon nanoparticles are uniformly distributed throughout the composite, but a meaningful size distribution could not be deduced from the TEM image due to variations in TEM focus through the width of the sample. EDX analysis confirms the presence of only Si and O. Selected area electron diffraction (Figure 2.10, inset) shows the particles are crystalline and have the characteristic diamond structure of silicon, supporting present XRD analysis. TEM of HF-liberated Si-NCs on carbon-coated grids show discrete Si-NCs with diameters of $d = 3.41$ nm ($2\sigma = 1.40$ nm; $n = 188$) and is consistent with Scherrer analysis of XRD signal broadening (Figure 2.11).

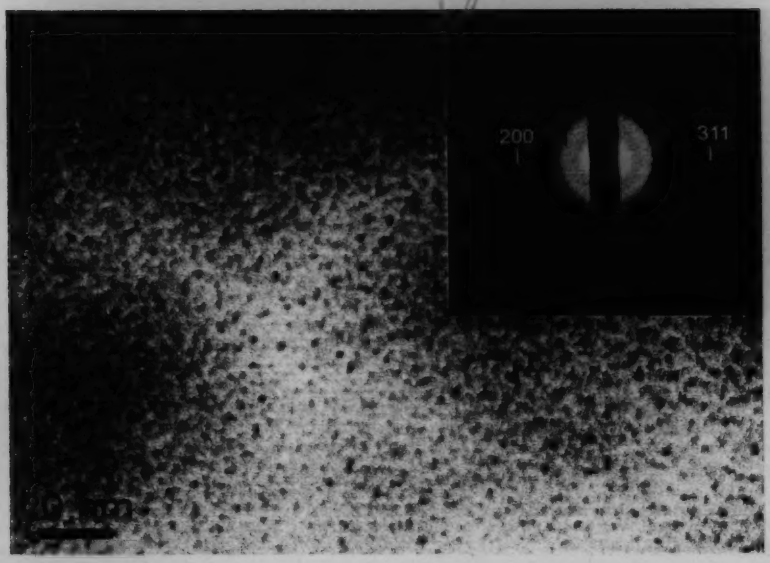

Figure 2.10. A brightfield transmission electron micrograph of **9**. (Inset: Selected area electron diffraction of Si-NC/SiO_2 thin film composite showing the characteristic (111), (220), and (311), reflections of diamond structure silicon.)

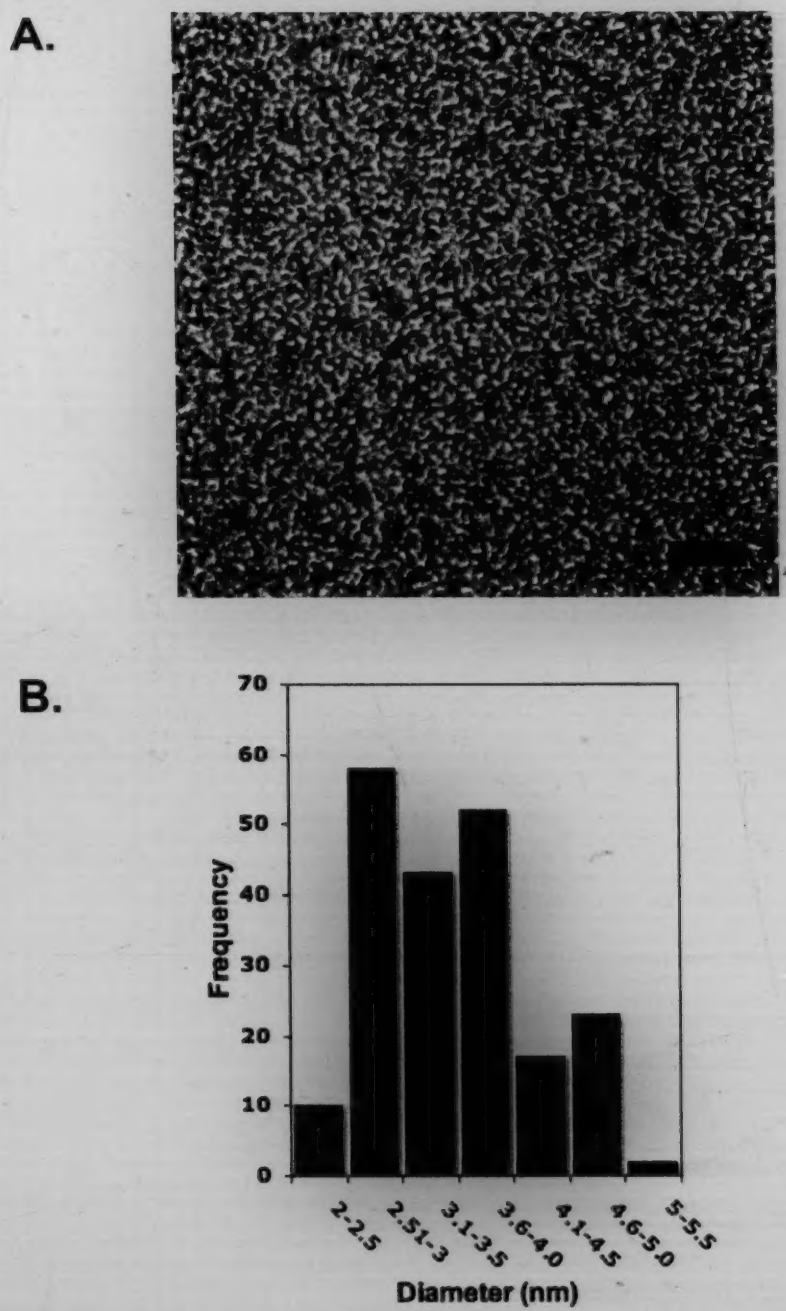

Figure 2.11. A. A representative bright-field transmission electron micrograph of **20** (bar = 20 nm). **B.** Size distribution of **20** providing average particle dimensions of d = 3.41 nm (2σ = 1.40 nm; n = 188).

2.4. Conclusion

The present report outlines a straightforward method for preparing macroscopic quantities of Si-NC/SiO_2 composites and freestanding Si-NCs that are photoluminescent through the visible and near-IR regions of the electromagnetic spectrum. Thermogravimetric analysis indicates that sample heating rate and processing atmosphere influence the weight loss arising from SiH_4 evolution. Transmission electron microscopy, selected area electron diffraction, X-ray powder diffraction and X-ray photoelectron spectroscopy all confirm the presence of Si-NCs. In addition, the solution processability, ease of handling, and chemical tunability of silsesquioxanes will facilitate the preparation of patterned optoelectronic films with tailored chemical response for incorporation into a variety of device structures including, chemical sensors, optical amplifiers, and waveguides.

2.5. References

(1) Buriak, J. M. *Chem. Rev.* **2002**, *102*, 1271.

(2) Meldrum, A. *Recent Res. Devel. Nuclear Phys.* **2004**, *1*, 93.

(3) Veinot, J.G.C. *Chem. Comm.* **2006**, 40, 4160.

(4) Bulk Si exhibits a sharp emission line at 1060 nm when cooled to liquid helium temperatures.

(5) Takagahara, T.; Takeda, K. *Phys. Rev. B* **1992**, *46*, 15578.

(6) Klimov, V.I.; Schwarz, C.J.; McBranch, D.W.; White, C.W. *Appl. Phys. Lett.* **1998**, *73*, 2603.

(7) Canham, L. T. *Appl. Phys. Lett.* **1990**, *57*, 1046.

(8) Baldwin, R.K.; Pettigrew, K.A.; Garno, J.C.; Power, P.P.; Liu, G.-Y.; Kauzlarich, S.M. *J. Am. Chem. Soc.* **2002**, *124*, 1150.

(9) Pettigrew, K.; Liu, Q.; Power, P.P.; Kauzlarich, S.M. *Chem. Mater.* **2003**, *15*, 4005.

(10) Rowsell, B.D.; Veinot, J.G.C. *Nanotechnology* **2005**, *16*, 732.

(11) Li, X.G.; He, Y.Q.; Swihart, M.T. *Langmuir* **2004**, *20*, 4720.

(12) Li, X.G.; He, Y.Q.; Talukdar, S.S.; Swihart, M.T. *Langmuir* **2003**, *19*, 8490.

(13) Nayfeh, M.H.; Barry, N.; Therrien, J.; Akcakir, O.; Gratton, E.; Belomoin, G. *Appl. Phys. Lett.* **2001**, *78*, 1131.

(14) Nayfeh, M.H.; Akcakir, O.; Belomoin, G.; Barry, N.; Therrien, J.; Gratton, E. *Appl. Phys. Lett.* **2000**, *77*, 4086.

(15) Belomoin, G.; Therrien, J.; Smith, A.; Rao, S.; Twesten, R.; Chaleb, S.; Nayfeh, M.H.; Wagner, L.; Mitas, L. *Appl. Phys. Lett.* **2002**, *80*, 841.

(16) Ding, Z.; Quinn, B.M.; Haram, S.K.; Pell, L.E.; Korgel, B.A.; Bard, A. J. *Science* **2002**, *296*, 1293.

(17) Derfus, A.M.; Chan, W.C.W.; Bhatia, S.N. *Nano Lett.* **2004**, 4, 11

(18) Glover, M.; Meldrum A. *Opt. Mater.* **2005**, *27*, 977.

(19) Z. Zhou, L Brus and R. Friesner. *Nano Lett.* **2003**, 3, 163.

(20) (a) J.H. Warner, H. Rubinsztein-Dunlop and R.D. Tilley, *J. Phys. Chem. B* **2005**, 109, 19064. b) J.H. Warner, A. Hoshino, K. Yamamoto and R.D. Tilley, *Angew. Chem. Int. Ed.* **2005**, 44, 4550. c) R.D. Tilley, J. H. Warner, K. Yamamoto, I. Matsui and H. Fujimori *Chem. Comm.* **2005**, 1833.

(21) J.D. Holmes, K.J. Ziegler, R.C. Doty, L.E.Pell, K.P. Johnston and B. A. Korgel, J. Amer. Chem. Soc. **2001**, 123, 3743.

(22) a) L. Brus, *J. Phys. Chem.* **1994**, 98, 3575. b) K.A. Littau, P.J. Szajowski, A.J. Muller, A.R. Kortan and L.E. Brus, *J. Phys. Chem.* **1993**, 97, 1224.

(23) M.V. Wolkin, J. Jorne, P.M. Fauchet, G. Allan and C. Delerue, *Phys. Rev. Lett.* **1999**, 82, 197.

(24) Breitenecker, M.; Sexl, R.; Thirring ,W. *Zeit. Physik* **1964**, *182*, 123.

(25) Hill, N. A.; Whaley, K. B. *J. Electron. Mater.* **1996**, *25*, 269.

(26) Hill, N. A.; Whaley, K. B. *Phys. Rev. Lett.* **1995**, *75*, 1130.

(27) Wang, L. W.; Zunger, A. *J. Phys. Chem.* **1994**, *98*, 2158.

(28) Delerue, C.; Allan, G.; Lannoo, M. *Phys. Rev. B* **1993**, *48*, 11024.

(29) Delerue, C.; Allan, G.; Lannoo, M. *J. Lumines.* **1998**, *80*, 65.

(30) Ogut, S.; Chelikowsky, J.R.; Louie, S.G. *Phys. Rev. Lett.* **1997**, *79*, 1770.

(31) Shimizu-Iwayama, T.; Ohshima, M.; Niimi, T.; Nakao, S.; Saitoh, K.; Fujita, T.; Itoh, N. *J. Phys.; Condens. Matter* **1993**, *5*, L375.

(32) Meldrum, A.; Haglund, R.F.; Boatner, L.A.; White, C.W. *Adv. Mater.* **2001**, *13*, 1431.

(33) Kahler, U.; Hofmeister, H.; *Opt. Mater.* **2001**, *17*, 83.

(34) Gorbilleau, F.; Portier, X.; Ternon, C.; Voivenel, P.; Madelon, R.; Riszk, R. *Appl. Phys. Lett.* **2001**, *78*, 3058.

(35) Orii, T.; Hirasawa, M.; Seto, T. *Appl. Phys. Lett.* **2003**, *83*, 3395.

(36) Valenta, J.; Janda, P.; Dohnalova, K.; Niznansky, D.; Vacha, F.; Linnros, *J. Opt. Mat.* **2005**, *27*, 1046.

(37) Recently bulk thermolysis of "SiO_x" was reported however no yield was provided. See: Liu, S.M.; Sato, S.; Kimura, K. *Langmuir* **2005**, *21*, 6324.

(38) Heath, J.R.; Shiang, J.J.; Alivisatos, A.P. *J. Chem. Phys.* **1994**, *101*, 1607.

(39) Baldwin, R.K.; Pettigrew, K.A.; Garno, J.C.; Power, P.P.; Liu, G.Y.; Kauzlarich, S. M. *J. Am. Chem. Soc.* **2002**, *124*, 1150.

(40) Zou, J.; Baldwin, R.K.; Pettigrew, K.A.; Kauzlarich, S.M. *Nano Lett.* **2004**, *7*, 1181.

(41) Pettigrew, K.A.; Liu, Q.; Power, P.P.; Kauzlarich, S.M. *Chem. Mat.* **2003**, *15*, 4005.

(42) Liu, Q.; Kauzlarich, S.M. *Mat. Sci. and Eng. B* **2002**, *96*, 72.

(43) Mayeri, D.; Phillips, B.L.; Augustine, M.P., Kauzlarich, S.M. *Chem. Mater,* **2001**, *13*, 765.

(44) Baldwin, R.K.; Pettigrew, K.A.; Ratai, E.; Augustine, M.P.; Kauzlarich, S.M. *Chem. Comm.* **2002**, *17*, 1822.

(45) Wilcoxon, J.P.; Provencio, P.P.; Samara, G.A. *Phys. Rev. B* **1999**,*60*, 2704.

(46) A. Meldrum, A. Hryciw, A.N. MacDonald, C. Blois, K. Marsh, J. Wang, and Q. Li, *J. Vac. Sci. Tech.* **2006**, 24, 713.

(47) Neufeld, E.; Wang, S.; Aptez, R.; Buchal, Ch.; Carius, R.; White, C.W.; Thomas, D.K. *Thin Sol. Films* **1997**, *294*, 238.

(48) Schulmeister, K.; Mader, W. *J. Non-Cryst. Sol.* **2003**, *320*, 143.

(49) Commercially available "SiO" is an orange/brown/black solid, however SiO is reported to be a white, crystalline (cub.) solid with m.p. > 1702 °C. See: *Handbook of Chemistry and Physics 73rd Edition*, D.R. Linde Editor, CRC Press, Boca Raton, FL. **1997**.

(50) "SiO_x" is viewed as an inert, amorphous material that converts to the thermodynamically favored nanocrystalline Si and SiO_2 upon thermal processing. See ref. 30.

(51) Brook, M.B. *Silicon in Organic, Organometallic, and Polymer Chemistry*, John Wiley and Sons, Inc.: New York, NY, **2000**.

(52) Feher, F.J.; Budzichowski, T.A.; Blanski, R.L.; Weller, K.J.; Ziller, J.W. *Organometallics* **1991**, 10, 2526.

(53) Feher, F.; Newman, D.A. *J. Am. Chem. Soc.* **1990**, *112*, 1931.

(54) Feher, F.; Newman, D.A.; Walzer, J.F. *J. Am. Chem. Soc.* **1989**, *111*, 1741.

(55) Feher, F.J.; Budzichowski, T.A.; Rahimian, K.; Ziller, J.W. *J. Am. Chem. Soc.* **1992**, *114*, 3859.

(56) Azinovic, D.; Cai, J.; Eggs, C.; Konig, H.; Marsmann, H.C.; Veprek, S. *J. Lumines.* **2002**, *97*, 40.

(57) Tour, J.M.; Pendalwar, S.L.; Cooper, J.P. *Chem. Mat.* **1990**, *2*, 647.

(58) Brook, M.A.; Ketelson, H.A.M.; Pelton, R.H.; Heng, Y.-M. *Chem. Mat.* **1996**, *8*, 2195.

(59) Arkles, B.; Berry, D.H.; Figge, L.K.; Composto, R.J.; Chiou, T.; Colazzo, H.; Wallace, W.E. *Sol-Gel Sci. Tech.* **1997**, *8*, 465.

(60) Yang, C.,-C.; Chen, W.-C. *J. Mat. Chem.* **2002**, 12, 1138.

(61) Hummel, J.; Endo, K.; Lee, W.W.; Mills, M.; Wang, S.Q. *Low-Dielectric Constant Materials V*, The Materials Research Society, Warrendale, PA, **1999**, vol. 565.

(62) Quantum yields were determined using the relationship: $\phi_{SiNP} = \phi_r \left(\frac{A_r}{A_{SiNP}}\right)\left(\frac{\eta_{SiNP}}{\eta_r}\right)^2\left(\frac{D_{SiNP}}{D_r}\right)$ where, ϕ_{SiNP}, A_{SiNP}, η_{SiNP}, and D_{SiNP} are the quantum yields, absorbance at the excitation wavelength, refractive index, and integrated photoluminescence intensity, respectively. The corresponding terms with subscript "*r*" refer to equivalent parameters for the appropriate standard. For the present approximation the following quantities were used: quantum yield (ϕ_r) of fluoroscein = 0.79, rhodamine 590 = 0.70, $[Ru(bpy)_3]Cl_2$ = 0.042, $\eta_{SiNP} \approx \eta_{pentane}$ = 1.357, $\eta_r \approx \eta_{water}$ = 1.333 for $[Ru(bpy)_3]Cl_2$, $\eta_r \approx \eta_{methanol}$ = 1.328 for fluorscein and rhodamine 590. Demas, J.N.; Crosby, G.A. *J. Phys. Chem.* **1971**, 75, 991.

(63) Williams, K. R. *J. Microelectromech. Syst.* **1996**, *5*, No. 4.

(64) Detailed literature studies of **HSQ** thermal properties report on thermal processing of partially crosslinked HSQ gels and thin films, accounting for small differences

in the present DSC temperature ranges. See: Yang, C., -C.; Chen, W.,-C. *J. Mat. Chem.* **2002**, 12, 1138.

(65) Belot, V.; Corriu, R.; Leclecq, D.; Mutin, P.H.; Vious, A. *Chem. Mat.* **1991**, *3*, 127.

(66) Krill, C.E.; Birringer, R.; *Phil. Mag. A.* **1998**, 77, 621.

(67) Jiang, H.G.; Rühle, M.; Lavernia, E.J.; *J. Mater. Res.* **1999**, 14, 549.

(68) Tian, H.H.; Atzmon, M.; *Phil. Mag. A.* **1999**, 79, 1769.

(69) Ungár, T.; Ott, S.; Sanders, P.G.; Borbély, A.; Weertman, J.R.; *Acta. Materialia.* **1998**, 46, 3693.

(70) Wang, J.; Wang, X.F.; Li, Q.; Hryciw, A.; Meldrum, A. *Phil. Mag.* **2006**, 87, 11.

(71) Frye, C.L.; Collins W.T.; *J. Am. Chem. Soc.* **1970**, 92, 5586.

(72) Albrecht, M.G.; Blanchette, C. *J. Electrochem. Soc.* **1998**, *145*, 4019.

(73) Etching times to achieve complete removal of the SiO_2-like matrix depends on grinding efficiency of the composite material and the corresponding composite particle size.

(74) Fojtik, A.; Henglein, A. *J. Phys. Chem B.* **2006**, *110*, 1994.

Chapter 3:

An investigation of the formation and growth of oxide-embedded silicon nanocrystals in hydrogen silsesquioxane derived nanocomposites*

* A version of this chapter has been published.

Hessel, C. M.; Henderson, E. J.; Veinot, J. G. C. *J. Phys. Chem. C* **2007**, 111, 6956 – 9661.

3.1. Introduction

Silicon structures in the form of porous silicon (p-Si), silicon rich oxides (SROs) and freestanding silicon nanocrystals (Si-NCs) have been shown to exhibit photoluminescent characteristics in the visible and near infrared (NIR) regions of the electromagnetic (EM) spectrum.[1,2,3] Bulk silicon has an indirect bandgap (E_g = 1.12 eV) whose optical transition is dipole-forbidden; this alone significantly limits practical optoelectronic application of the bulk crystal due to low photoluminescence intensity and slow carrier dynamics. As the dimensions of semiconductor particles approach the Bohr exciton radius (ca. 5 nm for silicon), quantum confinement (QC) effects emerge. One manifestation of QC is the shift of the photoluminescence (PL) maximum into the visible spectrum and a concomitant increase in emission intensity. Although numerous explanations for the PL response of Si nanostructures have been presented,[4,5] it is now generally accepted that this behavior results from quantum confinement.[6]

Methods for preparing freestanding Si-NCs, their surface functionalization, as well as their optical properties were the subjects of our recent review.[3] Our group,[7] and others[8] have tailored the PL maximum of freestanding Si-NCs throughout the visible spectrum by controlling particle dimensions. Typically, orange/red PL is observed from ca. 4 nm hydride surface-terminated freestanding Si-NCs.[8c] As expected from QC predictions, a significant blue shift in the PL occurs with decreasing size.[7,9] Blue PL has also been reported for silicon nanomaterials, [8a,10] but the emission mechanism was not reported. Although tailoring particle size affords some control over PL maximum, it also complicates material characterization and handling. To prepare easily manipulated nanocrystals with predictable, stable optical properties and useful electronic

characteristics, new experimental methods for controlling the electronic structure of freestanding Si-NCs must be investigated.

As with any preparative method, solution-based procedures for preparing freestanding Si-NCs have associated benefits and drawbacks.[3] These techniques have provided valuable examples of oriented crystal growth in Si nanowires,[11] shape control,[12] and compositional tailoring,[13] suggesting that controlling these properties may offer alternative methods for tuning the Si-NC PL. In addition, many technologically relevant Si-based nanomaterials of tailored composition and shape have been prepared using well-established physical techniques (e.g., ion implantation,[14a,b] vacuum evaporation,[14c] among others[14d,e]). If these materials could be obtained in tangible quantities (> 500 mg/batch), many optoelectronic applications such as fluorescent biological labels could be realized. Furthermore, other practical limitations of Si-based materials, such as low photoluminescence quantum yield, may be addressed.[15]

In chapter 2 we demonstrated the preparation of oxide-embedded Si-NCs via the controlled thermally induced disproportionation of hydrogen silsesquioxane, **HSQ**. Hydride surface-terminated freestanding Si-NCs are readily liberated from the resulting oxide matrix via straightforward chemical etching. Here we report a detailed investigation into the formation, crystallization, and growth of oxide embedded silicon nanodomains using state-of-the-art spectroscopic and diffraction techniques. Information obtained from the present study facilitates an understanding and ultimate application of our thermolytic approach to the synthesis of oxide embedded and freestanding Si containing Group IV semiconductor nanomaterials of well-defined size, shape, crystallinity, and composition.[16]

3.2. Experimental Details

3.2.1. Reagents and Materials

HSQ was purchased from Dow Corning (tradename FOx-17®) as a 17 weight percent solution in methyl isobutyl ketone and toluene. This stock solution was used as received and stored in subdued light and inert atmosphere prior to use.

3.2.2. Bulk Si-NC/SiO_2 Composite Preparation (1-16)

All composites were prepared as described in chapter 2.[7] In brief, solvent was removed from the stock solution to yield white, solid **HSQ** that was subsequently heated for a predetermined time in a 5% H_2 and 95% Ar atmosphere. In the furnace, samples were heated to peak processing temperatures at 20°C/min. Processing temperatures and times are summarized in Table 3.1. After cooling to room temperature, the solid was mechanically ground and the fine powder was suspended in distilled water and collected/dried by vacuum filtration. The resulting powders were evaluated using XPS, XRD, FT-IR, Raman, and PL spectroscopy.

Table 3.1. Samples of **HSQ** processed at 20°C/min for specified times and temperatures under 5%H_2/95%Ar. The Si L-edge electron binding energies for $Si^{(0)}$ and $Si^{(IV)}$ are presented with theoretical estimates of nanocrystal size for the corresponding samples.

Compd.	Processing Temp. (°C)	Processing Time (min.)	Si $^{(0)}$ $2p_{3/2}$ B.E. (eV)[a]	Si $^{(IV)}$ $2p_{3/2}$ B.E. (eV)[a]	XRD Diameter (nm)[b]	PL Diameter (nm)[c]
HSQ	-	-	-	-	-	-
1	300	60	-	-	-	-
2	400	60	-	-	-	-
3	500	60	-	-	-	-
4	600	60	99.3	104	-	-
5	700	60	99.4	103.6	-	-
6	800	60	99.2	103.6	-	-
7	900	60	99.1	103.6	-[d]	4.1
8	1000	60	99.1	103.3	-[e]	4.8
9	1100	60	99.1	103.5	3.3	4.8
10	1200	60	99	103.6	4.2	5.1
11	1300	60	98.9	103.8	5.5	6.0
12	1400	60	98.8	103.7	8.7	6.0
13	1100	120	99.6	103.7	3.2	5.1
14	1100	300	99.5	103.5	3.4	5.5
15	1100	600	99.6	103.9	3.6	5.9
16	1100	1440	99.5	103.9	3.6	6.3
Si Powder	-	-	98.7	-	-	-

[a] All spectra were calibrated to the C1s emission (284.8eV)

[b] Determined using Scherrer Analysis as described in reference 22.

[c] Determined using the Effective Mass Approximation as described in reference 26.

[d] No diffraction was observed for samples processed at or below 900°C.

[e] Only weak diffraction was observed hindering application of the Scherrer Relationship.

3.2.3. X-ray Photoelectron Spectroscopy (XPS)

All spectra were collected using a Kratos Axis Ultra instrument operating in energy spectrum mode at 210 W. The base pressure and operating chamber pressure was maintained at $\leq 10^{-7}$ Pa. A monochromatic Al K_α source was used to irradiate the samples and the spectra were obtained with an electron take-off angle of 90°. To control sample charging, the charge neutralizer filament was used during all experiments. Wide survey spectra were collected using an elliptical spot with 2 mm and 1 mm major and minor axis lengths, respectively, and a 160 eV pass energy with a step of 0.33 eV.

3.2.4. X-ray Photoelectron Spectroscopy Analysis

CasaXPS (Vamas) software was used to process high-resolution spectra. All spectra were calibrated to the C1s emission (284.8eV) arising from surface contamination. After calibration, the background from each spectrum was subtracted using a Shirley-type background to remove most of the extrinsic loss structure.[17] Sample compositions were determined from the emission intensities of the survey spectra using appropriate sensitivity factors.

The high-resolution Si 2p region of spectra collected for **1-16** were fit to Si $2p_{1/2}$ Si $2p_{3/2}$ partner lines with spin-orbit splitting fixed at 0.6 eV and the Si $2p_{1/2}$ Si $2p_{3/2}$ intensity ratio was set to ½.

3.2.5. X-ray Powder Diffraction (XRD)

Bulk crystallinity of finely ground **1-16** mounted on a low intensity background silicon (100) sample holder was evaluated using an INEL XRG 3000 X-ray diffractometer equipped with a Cu K_α radiation source.

3.2.6. Optical Spectroscopy

Fourier-transform infrared spectroscopy (FTIR) of powders was performed using a Nicolet Magna 750 IR spectrophotometer. Raman spectroscopy was performed using a Renishaw inVia Raman microscope equipped with a 785 nm diode laser and a power of 7.94 mW on the sample. Photoluminescence (PL) spectra of finely powdered composites (**1-16**) dropcoated from a pentane suspension onto optical grade quartz were evaluated at room temperature using the 325 nm line of a He-Cd laser excitation source. PL emission was detected with a fiber-optic digital charge coupled device (CCD) spectrometer whose spectral response was normalized using a standard blackbody radiator.

3.3. Results and Discussion

In chapter 2 we have shown that thermal processing of **HSQ** is a convenient and versatile method for preparing tangible quantities of silicon nanocrystal composites, (Si-NC/SiO_2).[7] However, the formation mechanism of the SiNCs remains unclear. A better understanding of the processes leading to the formation of Si-NCs obtained from the studies described herein will assist in controlling particle dimensionality, shape, crystallinity, and composition. **HSQ** has been processed under varied reaction conditions and the resulting composites (**1** - **16**) were evaluated using XPS, XRD, FTIR, Raman, and PL.

3.3.1. X-ray Photoelectron Spectroscopy

Survey XP scans confirm that composites **1**-**16** contain only silicon, oxygen, and adventitious carbon impurities. Figures 3.1 and 3.2 show representative high-resolution Si 2p XP spectra collected for **1**-**16**. Like XP spectra reported for ion implanted SROs, Si/SiO_2 interfaces, and substituted siloxane polymers,[18] those obtained for **5** - **16** show two distinct spectral regions corresponding to $Si^{(IV)}$ and $Si^{(0)}$ that are separated by a non-zero baseline. For these materials, the Si 2p region is routinely fit to Si $2p_{1/2}$ and Si $2p_{3/2}$ partner lines for $Si^{(IV)}$, $Si^{(0)}$, and low valent Si (i.e, $Si^{(n)}$; n =0, I, II, III) arising from silicon sub-oxides, SiO_x (i.e., x = 1/2, 1, 3/2 for Si_2O, SiO, and Si_2O_3, respectively).[19] The structures of composites **5**-**16** are dominated by interfaces between Si nanodomains[20] and an SiO_2-like matrix, and it is therefore reasonable that similar sub-oxides exist. However, it is difficult to differentiate between the influences of bulk sub-oxides from ill-defined interfaces between Si nanodomains and SiO_2 consisting of $Si(-O)_n$ (n = 1 – 3) linkages.

In addition, present FT-IR analysis indicates significant Si-H bonding (*vide infra*) which may complicate detailed interpretation of the XP spectra of **1-6**.

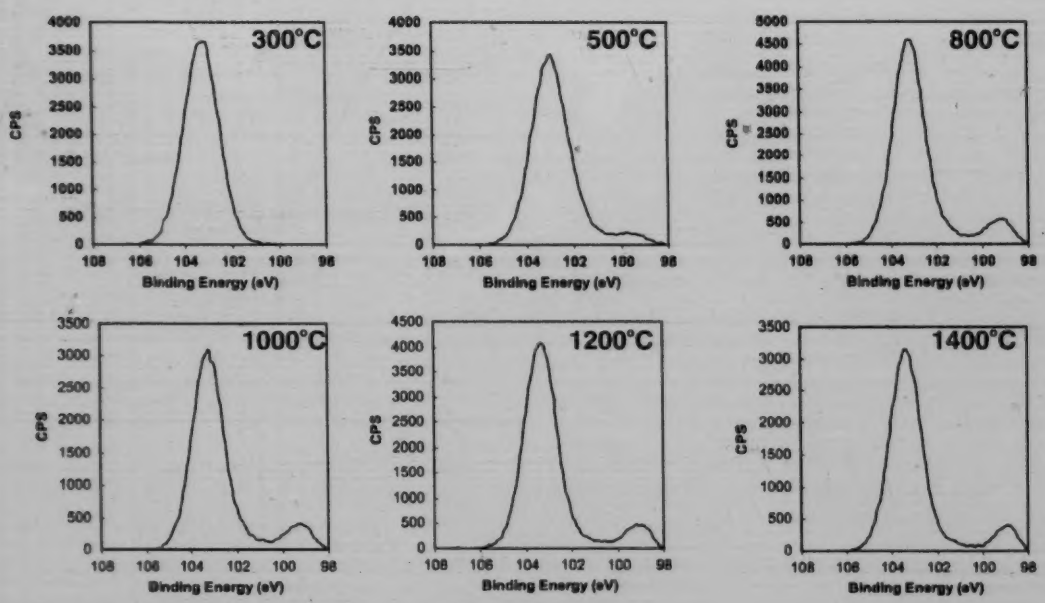

Figure 3.1. Representative Shirley background subtracted high-resolution XP spectra of the Si 2p region for Si-NC/SiO_2 composites obtained from processing HSQ at the indicated temperature. This series of spectra clearly highlights the evolution of the low oxidation state Si emission with increased processing temperature.

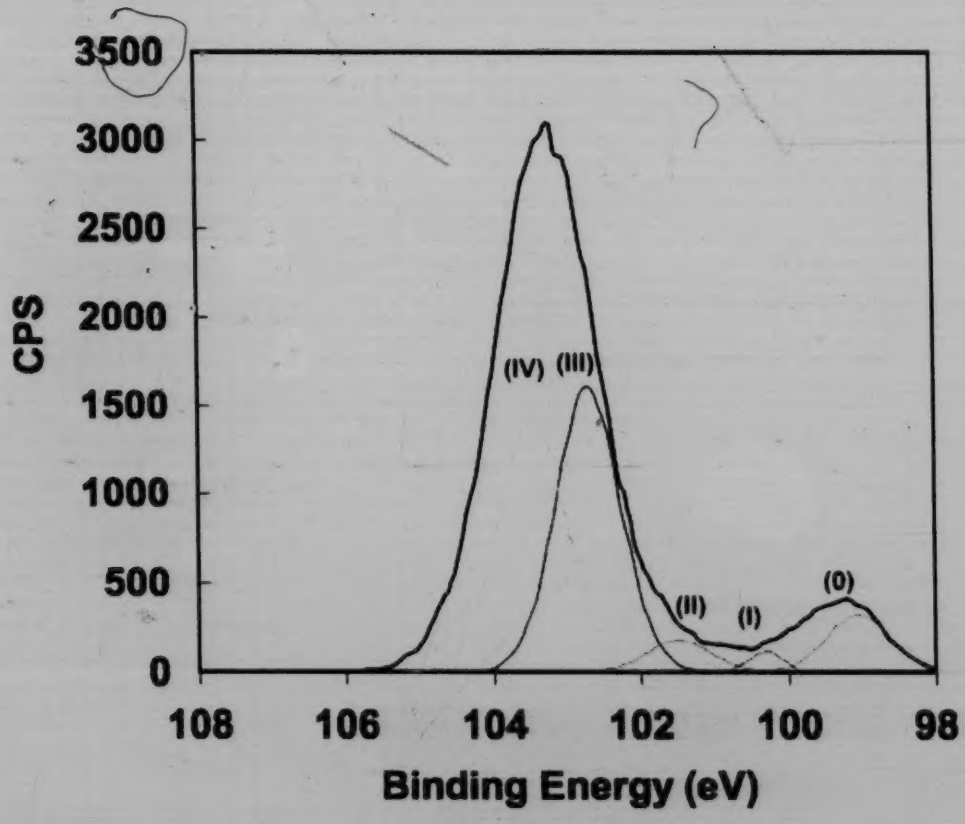

Figure 3.2. Shirley background subtracted high-resolution XP spectrum of the Si2p region for Si-NC/SiO_2 for **9** (i.e., processing T=1100°C). For clarity only the Si $2p_{3/2}$ spin-orbit couple partner lines are shown.

Despite these factors, we fit XP spectra of **1** - **16** to suitable Si $2p_{1/2}$ and Si $2p_{3/2}$ partner lines for $Si^{(n)}$(n = 0 – IV). It is clear from the evolution of the Si 2p spectral region, shown in Figure 3.1, that increased processing temperature results in increased concentrations of low valent silicon. For composites prepared at or below 400°C (i.e., **1** and **2**) the Si 2p emission is readily fit to the Si $2p_{1/2}$ and Si $2p_{3/2}$ partner lines for $Si^{(IV)}$ and $Si^{(III)}$. Beginning at 500°C (i.e., **3**) a weak, low energy emission emerges, arising from low valent Si. When the processing temperature is increased to 800°C, 1000°C, 1200°C,

and 1400°C (i.e., **6, 8, 10, 12**), this new peak shifts to lower energy and increases in intensity with greater $Si^{(0)}$ contribution. Table 3.1 summarizes $Si^{(0)}$ and $Si^{(IV)}$ Si $2p_{3/2}$ binding energies for **1-16**. We observe insignificant changes in the $Si^{(0)}$ 2p region with prolonged processing at 1100°C (i.e., **9, 13 - 16**). With increased processing temperature (**4 - 12**) the $Si^{(IV)}$ $2p_{3/2}$ emission remains constant, consistent with little or no sample charging. In contrast, for samples **9 - 12**, a clear relationship between peak processing temperature and $Si^{(0)}$ $2p_{3/2}$ binding energy emerges. As processing temperature is increased above 1100°C the $Si^{(0)}$ $2p_{3/2}$ emission shifts to lower binding energy and approaches our measured value for bulk Si of 98.7 eV (See Figure 3.3). Qualitatively, this shift has been shown for oxide-embedded Si-NCs of increasing size.[19d] In summary, the present XPS suggests that low valent Si begins forming upon heating **HSQ** in a reducing environment at ca. 500°C. With increased processing temperature $Si^{(0)}$ reaches a maximum concentration for composites prepared at 1000°C (i.e., **8**). Subsequent increases in processing temperatures result in Si nanodomain crystallization and crystal growth, which are supported by the XRD, FT-IR, Raman, and PL analyses (*vide infra*).

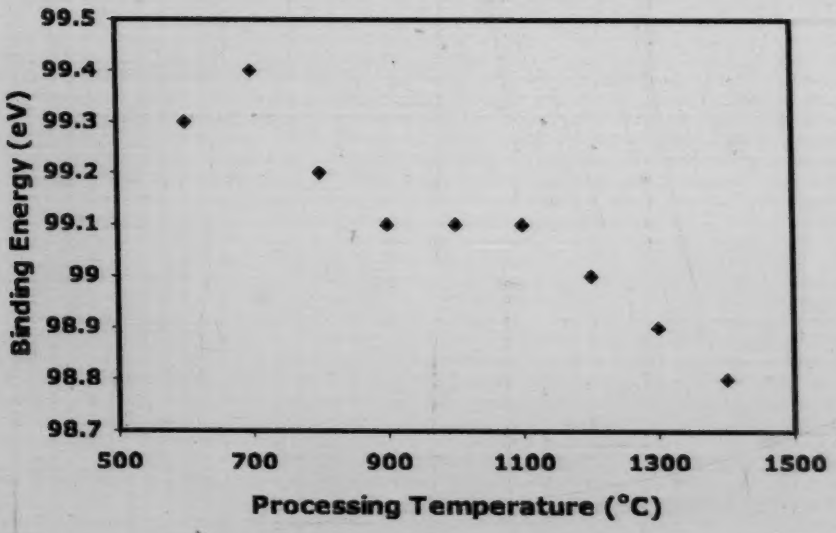

Figure 3.3. The relationship between Si $2p_{3/2}$ binding energy and peak processing temperature.

3.3.2. X-ray Powder Diffraction

Previously in chapter 2 we demonstrated that Si/SiO_2 composites obtained from thermally processing **HSQ** at < 900°C contained no detectable Si-NCs. We also showed that subsequent heating of low temperature processed **HSQ** samples at 1100°C yields Si-NC/SiO_2.[7] Here we demonstrate the effect of increased processing temperature and time on nanodomain size and crystallinity. X-ray diffraction patterns of HSQ processed between 1100°C– 1400°C (Figure 3.4) show the evolution of characteristic Si reflections with processing temperature. Broadened peaks indexed to the (111), (220), and (311) crystal planes of diamond structure Si are observed for **9** and **10**. After heating to 1300°C broadened reflections arising from the Si diamond structure (111), (220), (311), (400), (331), (422), (333), (440), and (531) crystal planes are observed. These reflections

narrow and intensify upon heating to 1400°C, indicating increased crystallinity and growth of oxide embedded Si-NC domains. Scherrer analyses of XRD peak broadening for samples **9** - **12** approximate crystal diameters in the range of 3.3 – 8.7 nm (Table 3.1).[21] Undetectable changes in particle dimension (i.e., d < 0.5 nm) were observed for prolonged heating at 1100°C, consistent with a report describing the influence of processing time on particle size in Si-NC/SiO_2 composites obtained from annealing ion implantation samples.[22] However, we do note slight increases in peak intensity relative to the amorphous background, suggesting improved particle crystallinity that possibly arises from the elimination of defects via a thermal annealing process.

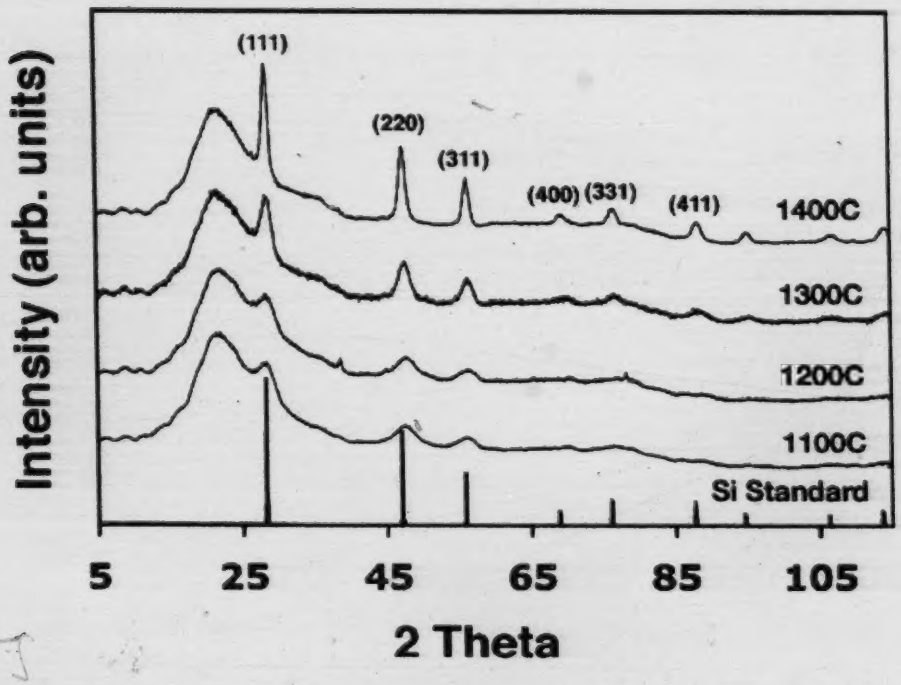

Figure 3.4. X-ray powder diffraction patterns showing the appearance of characteristic Si (111), (220), (311), (400), (331), (422), (333), (440), and (531) reflections for composites **9**, **10**, **11**, and **12**. Peak processing temperatures are indicated for clarity.

3.3.3. Fourier Transform Infrared and Raman Spectroscopy

FT-IR spectroscopy of **HSQ** shows a characteristic Si-H stretching absorption at 2251 cm^{-1}.[7] Absorptions are also noted in the range of ca. 1300 to 800 cm^{-1} and have previously been assigned to internal vibrations of the Si-O-Si cage framework.[23] The FT-IR spectra of **1** and **2** strongly resemble that of **HSQ**. Products obtained from increased processing temperatures (i.e., **3 – 7**) show decreased Si-H stretching intensity, Figure 3.5. This can be attributed to the loss of hydrogen from hydrogenated Si nanodomains. Samples obtained from processing at, or above 900°C (**8 – 12**) show no evidence of Si-H bonding. We also observe a replacement of **HSQ** cage Si-O-Si vibrations for **1 – 7** with a broad, featureless absorption centered at ca. 1096 cm^{-1} that we assign to Si-O-Si bending in an SiO_2-like network (Figure 3.5). No changes in the Si-O-Si spectral region are noted for **8 – 12**. Raman spectra in Figure 3.6 show an increased intensity of the Si-Si optical phonon vibration at ca. 507 cm^{-1} for **1** through **7.** This observation is consistent with the presence of more Si-Si bonds resulting from the increased concentration of $Si^{(0)}$ evident in our XPS analyses (*vide supra*).

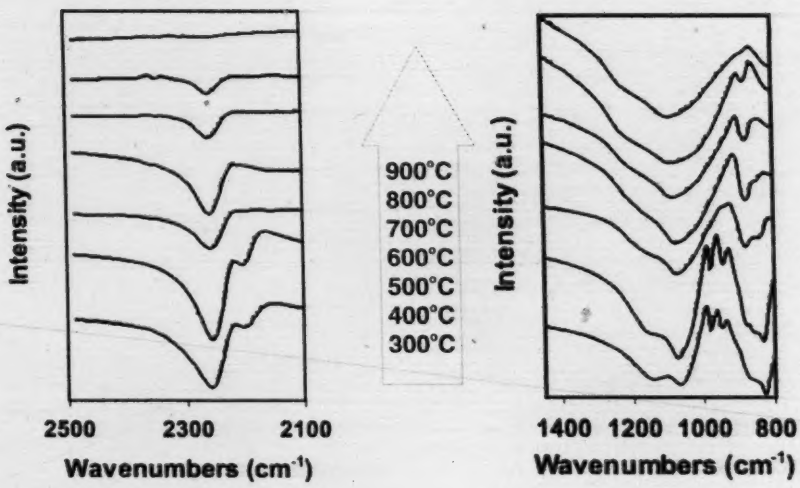

Figure 3.5. FTIR spectra of composites **1 – 7** showing a marked decrease in Si-H stretching (left) and increase in Si-O-Si stretching with increased processing temperature. Processing temperatures are noted for clarity.

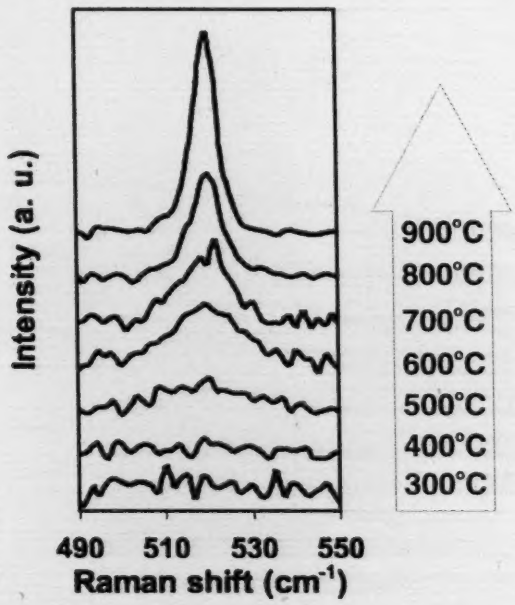

Figure 3.6. The Si-Si region of the Raman spectra of composites **1 – 7** showing a clear increase in Si-Si vibration with increased peak processing temperature. Processing temperatures are provided for clarity.

3.3.4. Photoluminescence Spectroscopy

It is generally accepted that the major contributing factor to the photoluminescent behavior of Si-NCs is quantum confinement. Correspondingly, there are numerous reports of size dependent emission maxima. In addition there are many computational methods for relating PL energy to particle size, including: the effective mass approximation,[24] empirical tight binding band theory,[25] empirical pseudopotential approximation,[26] and *ab-initio* local density approximation.[27] It is undisputable that particle size strongly influences the photoluminescent properties of Si-NCs; still numerous factors complicate straightforward interpretation of the Si-NC PL data, including: interfacial sites,[28] defects,[29,30,31] size distribution and carrier tunneling,[32] surface chemistry,[6a,b,33] and inter-particle spacing.[34]

The photoluminescent responses of the present **HSQ** derived Si-NC/SiO_2 composites were evaluated as a function of processing time (**9**, **13 – 16**) and temperature (**7 – 12**). We note that increasing processing time from 1 to 24 hours at 1100°C, results in a red-shift of the PL maximum from 819 to 920 nm (Figure 3.7A). The effective mass approximation[Error! Bookmark not defined.] predicts this shift would result from an in increase in average particle diameter from ca. 5 to 7 nm. This assumes the change in PL maximum arises solely from the influence of quantum confinement. This prediction is not supported by our XRD analyses of **9**, **13 – 16** (vide supra) and we conclude that another mechanism is responsible for the observed spectral changes.

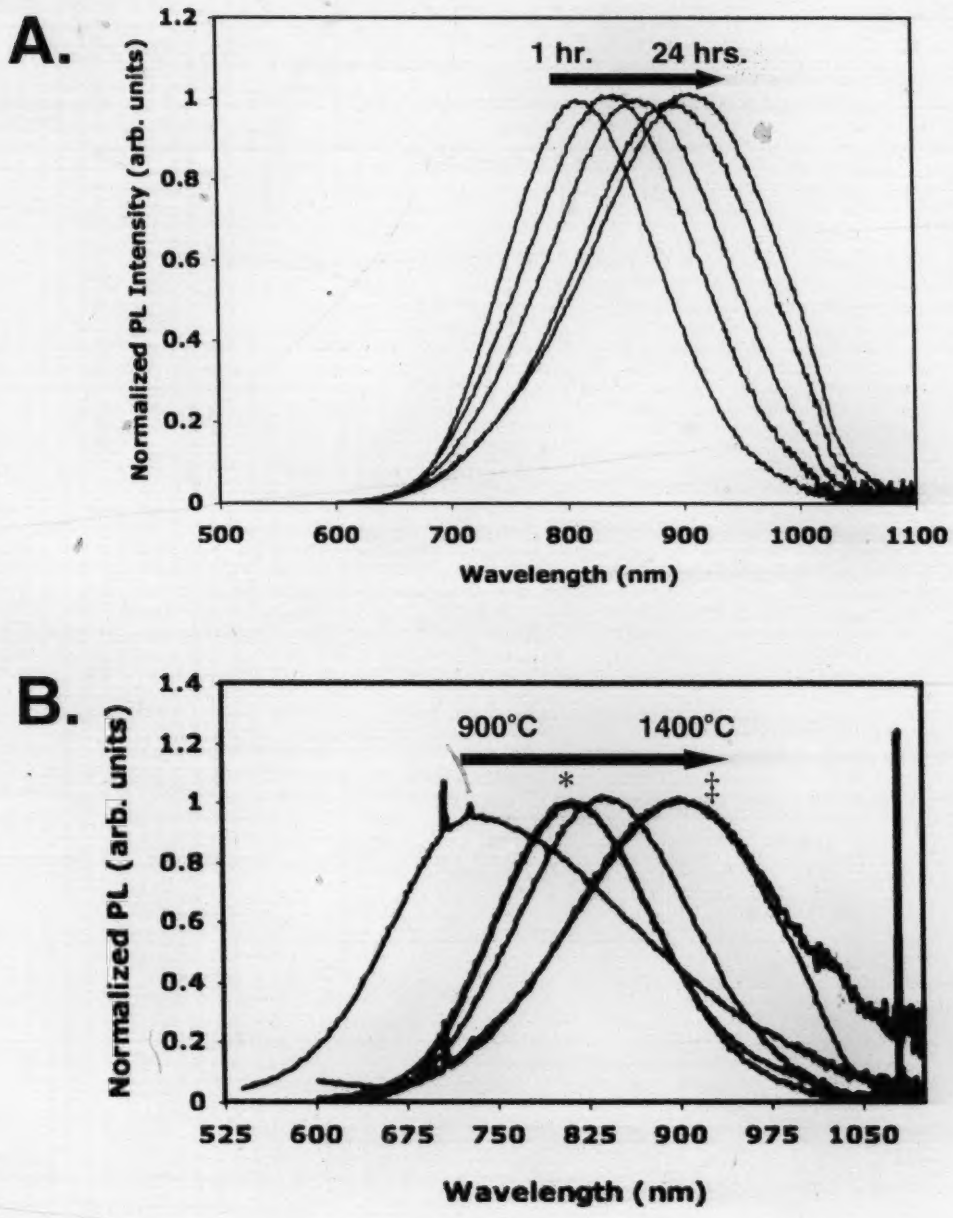

Figure 3.7. Normalized PL spectra for cast films of **9**, **13** - **16** (top) and **7** – **12** (bottom).

* PL spectra for 8 and 9 (*) and 11 and 12 (‡) are coincident.

Similar PL spectral shifts have been noted for Si-NC/SiO_2 composites annealed in 5%H_2/95%N_2 for prolonged periods. These changes have been attributed to the enhancement of the emission from larger nanocrystals resulting from the passivation of volume defects.[29] In this regard, our PL observations can be explained in the context of the distribution of defects within **HSQ** derived oxide-embedded Si-NCs. Larger crystalline silicon nanodomains are expected to contain more defects by virtue of their larger volume. This higher defect concentration causes the PL of larger particles to be preferentially quenched. With this in mind, prolonged heating in 5%H_2/95%Ar at 1100°C is expected to remove volume defects via an annealing/passivation process that ultimately renders larger particles luminescent. While one may expect this process to qualitatively yield a straightforward broadening of the PL band, this is not the case. It was recently shown that nonresonant carrier tunneling to larger Si-NCs quenches the PL emanating from smaller nanocrystals within Si-NC/SiO_2 composites.[32] Consequently, the PL spectra of Si-NC/SiO_2 composites are dominated by the optical response of the largest particles present. Of important note, our proposal of an annealing/passivation/tunneling model requires no significant change in particle dimensionality or particle size distribution, and is fully consistent with present experimental observations.

In contrast, with increased processing temperature the resulting Si-NC/SiO_2 composites exhibit a significant red-shift in PL maximum, consistent with Scherrer interpretation of XRD data (Figure 3.7B, Table 3.1). Particle dimensions of **9 - 11** determined using the effective mass approximation are consistently larger than those predicted from our Scherrer interpretation of XRD line broadening. This apparent inconsistency is expected because the PL response of Si-NC/SiO_2 composites is

dominated by the largest photoluminescent particles present (vide supra).[32] We also note that the PL maxima of **11** and **12** remain constant and qualitatively decrease in intensity with higher processing temperature. These observations may be understood in the context of our XRD analyses that show the nanocrystal dimensions exceed the Bohr exciton radius for Si (ca. 5 nm). It is expected that Si-NCs with dimensions larger than the Bohr exciton radius will not photoluminesce because of the appearance of bulk material properties.

3.3.5. Factors Influencing Silicon Nanodomain Formation, Growth, and Crystallization

The combination of diffraction and spectroscopic analyses described herein, effectively tracks the formation and crystallization of Si nanodomains. In summary, we divide the processes into three stages as illustrated in Scheme 3.1.

1. *HSQ structural changes*. Processing **HSQ** at, or below 400°C provides no low valent Si (i.e., Si^{n+}, where n<4) at the sensitivity of the present techniques. Subtle changes in the FTIR spectrum have been qualitatively attributed to **HSQ** crosslinking and cage rearrangement. Definitive assignments of these structural changes are beyond the scope of the present discussion.
2. *Formation and growth of oxide-embedded Si nanodomains*. XP, Raman, and FT-IR spectra of **3** - **6** all support the presence of partially hydrogenated elemental Si nanodomains. XP analyses show increasing low oxidation state Si concentrations for samples **3** - **6**. Raman spectra indicate increased Si-Si emission while FT-IR exhibits a decrease in Si-H stretching for **3** – **6**. In addition, XRD shows no evidence of long-

range order in these samples. These data support the formation and dehydrogenation of noncrystalline Si nanodomains with increased heating. The exact source of the these nanodomains remains unclear, but our observations remain in agreement with our earlier proposal that they may arise from the rapid thermal decomposition of silane at ca. 450°C.

XP and Raman spectra of **7** show maximum concentrations of $Si^{(0)}$ and Si-Si bonding, respectively. FT-IR shows no evidence of Si-H stretching and particle crystallinity is not detected at the sensitivity of our analyses. In addition, we observe a weak, broad photoluminescence band emerges for **7**. From these observations of **7**, we conclude that the oxide embedded nanodomains are completely dehydrogenated and are on the cusp of crystallization.

3. *Nanodomain crystallization and growth.* XRD, PL, and XP data all confirm the growth and increased crystallinity of silicon nanodomains with increased processing temperature above 900°C (i.e., **8 – 12**). In addition, prolonged heating at 1100°C also results in an annealing process and passivation of volume defects.

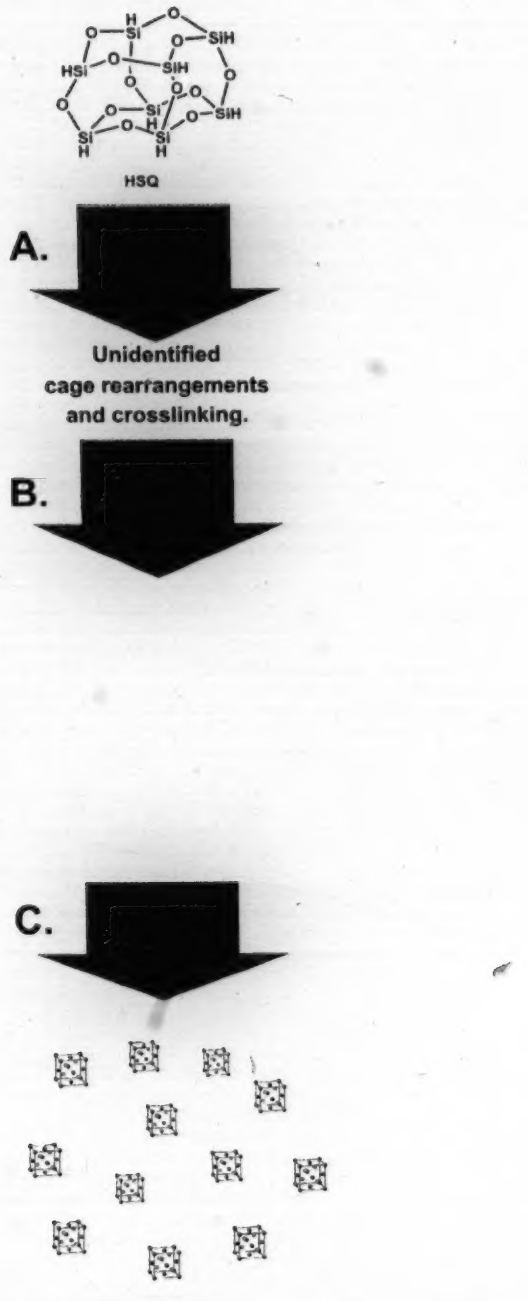

Scheme 3.1. Processing **HSQ** at: **A.** ≤400°C for 1 hour yields unidentified, crosslinked silsesquioxane materials. **B.** 500-800°C for 1 hr. provides material containing low valent Si, Si-H and Si-O bonding. **C.** 900°C-1400°C for 1 hr. induces crystallization and growth of Si nanodomains.

3.4. Conclusion

The present report outlines a detailed, spectroscopic and diffraction study of the formation of oxide-embedded Si-NCs during the reductive thermal processing of hydrogen silsesquioxane. From this study we have identified three stages in the formation of oxide-embedded Si-NCs from the thermal processing of **HSQ**. Our data indicates that hydrogenated amorphous silicon nanodomains evolve into well-defined Si-NCs upon thermal processing. The silicon-based nanocomposites are readily prepared in large quantities via straightforward thermal processing. In addition, nanodomain size and crystallinity can be tailored via careful control of processing parameters. The present understanding of the Si-NC/SiO_2 formation process will facilitate rational experimental design leading to the synthesis of oxide-embedded Si-NCs of controlled composition and shape.

3.5. References

(1) Buriak, J. M. *Chem. Rev.* **2002**, 102, 1271.

(2) Meldrum, A. *Resent Res. Devel. Nuclear Phys.* **2004**, 1, 93.

(3) Veinot, J.G.C. *Chem. Comm.* **2006**, 40, 4160.

(4) Takagahara, T.; Takeda, K. *Phys. Rev. B* **1992**, 46, 15578.

(5) Klimov, V.I.; Schwarz, C.J.; McBranch, D.W.; White, C.W. *Appl. Phys. Lett.* **1998**, 73, 2603.

(6) a) Brus, L. *J. Phys. Chem.* **1994**, 98, 3575. b) Littau, K.A.; Szajowski, P.J.; Muller, A.J.; Kortan, A.R.; Brus, L.E. *J. Phys. Chem.* **1993**, 97, 1224. c) Wilson, W.; Brus, L.E. *Science* **1993**, 262, 1242. d) Brus, L.E. *Appl. Phys. A* **1991**, 53, 465.

(7) Hessel, C.M.; Henderson, E.J.; Veinot, J.G.C. *Chem. Mat.* **2006**, 18, 6139.

(8) a) Hua, F.; Erogbogbo, F.; Swihart, M.T.; Ruckenstein, E. *Langmuir* **2006**, 22, 4363. b) Hua, F.; Swihart, M.T.; Ruckenstein, E., *Langmuir* **2005**, 21, 6054. c) Li, X.; He, Y.; Swihart, M.T. *Langmuir* **2004**, 20, 4720. d) Li, X.; He, Y.; Talukdar, S.S.; Swihart, M.T., *Langmuir* **2003**, 19, 8490. c) Liu, S-M.; Sato, S.; Kimura, K. *Langmuir* **2005**, 21, 6324.

(9) Ehbrecht, M.; Kohn, B.; Huisken, F.; Laguna, M. A.; Paillard, V. *Phys. Rev. B* **1997**, 56, 6958.

(10) a) Tilley, R.D.; Warner, J.H.; Yamamoto, K.; Matsui, I.; Fujimori, H. *Chem. Comm.* **2005**, 1833. b) Holmes, J.D.; Ziegler, K.J.; Doty, C.; Pell, L.E.; Johnston, K.P.; Korgel, B.A., *J. Am. Chem. Soc.* **2001**, 123, 3743.

(11) a) Lee, D.C. Hanrath, T.; Korgel, B.A., *Angew. Chem. Int. Ed.* **2005**, 44, 3573. b) Tuan H.-Y.; Lee, D.C.; Hanrath, T.; Korgel, B.A., *Nano Lett.* **2005**, 5, 681. c) Lu X., Hanrath, T.; Johnston, K.P.; Korgel, B.A., *Nano Lett.* **2003**, 3, 93.

(12) Baldwin, R.K.; Pettigrew, K. A.; Garno, J.C.; Liu, G.; Kauzlarich, S.M., *J. Am. Chem. Soc.* **2002**, 124, 1150.

(13) Baldwin, R.K. et al., *Chem. Comm.* **2006**, 658.

(14) a) Shimizu-Iwayama, T.; Ohshima, M.; Niimi, T.; Nakao, S.; Saitoh, K.; Fujita, T.; Itoh, N. J. Phys.; *Condens. Matter* **1993**, 5, L375. b) Meldrum, A.; Haglund, R. F.; Boatner, L. A.; White, C. W. *Adv. Mater.* **2001**, 13, 1431. c) Kahler, U.; Hofmeister, H. *Opt. Mater.* **2001**, 17, 83. d) Gorbilleau, F.; Portier, X.; Ternon, C.; Voivenel, P.; Madelon, R.; Rizk, R. *Appl. Phys. Lett.* **2001**, 78, 3058. e) Orii, T.; Hirasawa, M.; Seto, T., *Appl. Phys. Lett.* **2003**, 83, 3395.

(15) a) Mimura, A.; Fujii, M.; Hayashi, S. *Phys Rev B*, **2000**, 62, 12625. b) Fujii, M.; Mimura, A.; Hayashi, S.; Yamamoto, K. *Appl. Phys. Lett.* **1999**, 75, 184. c) Fujii, M.; Mimura, A.; Hayashi, S.; Yamamoto, K.; Urakawa, C.; Ohta, H., *J. App. Phys.* **2000**, 87, 1855., d) Tetelbaum, D.I.; Gorshkov, O. N.; Trushun, S. A.; Revin, D. G.; Gaponova, D. M.; Eckstein, W. *Nanotech.* **2000**, 11, 295.

(16) Henderson, E.J.; Veinot, J.G.C. *Chem. Mat.* **2007**, 19, 1886.

(17) Norgren, B.S.; Somers, M.A.J.; deWit, J.H.W. *Surf. Interface Anal.* **1994**, 21, 378.

(18) O'Hare, L.-A.; Parboo, B.; Leadley, S.R. *Surf. Interface Anal.* **2004**, 36, 1427.

(19) a) Liu, Y.; Chen, T.P.; Ng, C.Y.; Ding, L.; Zhang, S.; Fu, Y.Q.; Fung, S. *J. Phys. Chem. B* **2006**, 110, 16499. b) Chen, T.P.; Liu, Y.; Sun, C.Q.; Tse, M.S.; Hsieh, J.H.; Fu, Y.Q.; Liu, Y.C.; Fung, S. *J. Phys. Chem. B.* **2004**, 108, 16609. c) Karadas, F.; Ertas, G.; Suzer, S. *J Phys. Chem. B* **2004**, 108, 1515. d) Sun, C.Q.; Pan, L.K.; Fu, Y.Q.; Tay, B.K.; Li, S. *J. Phys. Chem. B* **2003**, 107, 5113.

(20) For clarity, we define a Si "nanodomain" as an oxide embedded silicon-rich region of unspecified crystallinity and chemical composition (i.e., it may contain hydrogen).

(21) Comedi, D.; Zalloum, O.H.Y.; Irving, E.A.; Wojcik, J.; Flynn, M.J.; Mascher, P. *J. Appl. Phys.* **2006**, 99, 023518. and references therein.

(22) Fernandez, B.G.; López, M.; Garcia, G.; Pérez-Rodriguez, Morante, J.R.; Bonafos, C.; Carrada, M.; Claveria, A. *J. App. Phys.* **2002**, 91, 798.

(23) Albrecht, M.G.; Blanchette, C. *J. Electrochem. Soc.* **1998**, 145, 4019.

(24) Breitenecker, M.; Sexl, R.; Thirring ,W. *Zeit. Physik* **1964**, 182, 123.

(25) a) Hill, N. A.; Whaley, K. B. *J. Electron. Mater.* **1996**, 25, 269. b) Hill, N. A.; Whaley, K. B. *Phys. Rev. Lett.* **1995**, 75, 1130.

(26) a) Wang, L. W.; Zunger, A. *J. Phys. Chem.* **1994**, 98, 2158. b) Delerue, C.; Allan, G.; Lannoo, M. *Phys. Rev. B* **1993**, 48, 11024.

(27) a) Delerue, C.; Allan, G.; Lannoo, M. *J. Lumines.* **1998**, 80, 65. b) Ogut, S.; Chelikowsky, J.R.; Louie, S.G. *Phys. Rev. Lett.* **1997**, 79, 1770.

(28) a) Iwayama, T.S.; Hama, T.; Hole, D.E.; Boyd, I.W. *Vacuum* **2006**, 81, 179. b)Shimizu-Iwayama, T.; Hama T.; Hole, D.E.; Boyd, I.W. *Solid State Elec.* **2001**, 45, 1487. c) Shimizu-Iwayama, T.; Kurumado, N.; Hole, D.E.; Townsend, P.D. *J. Appl. Phys.* **1998**, 83, 6018.

(29) a) Cheylan, S.; Elliman, R.G. *Appl. Phys. Lett.* **2001**, 78, 1225. b) Cheylan, S.; Elliman, R.G. *Appl. Phys. Lett.* **2001**, 78, 1912. c) Cheylan, S.; Elliman, R.G. *Nuclear Inst. Methods* **2001**, 175, 422.

(30) Lannoo, M.; Delerue, C.; Allan, G. *J. Lumines.* **1996**, 70, 170.

(31) Neufield, E.; Wang, S.; Apetz, R.; Buchal, C.; Carius, R.; White, C.W.; Thomas, D.K. *Thin Solid Films* **1997**, 294, 238.

(32) Lockwood, R.; Hryciw, A.; Meldrum, A. *Appl. Phys. Lett.* **2006**, 89, 263112.

(33) Zhou, Z.; Brus, L.; R. Friesner, R. *Nano Lett.*, **2003**, 3, 163

(34) Glover, M.; Meldrum, *A. Opt. Mat.* **2005**, 27, 977.

Chapter 4:

The origin of luminescence from silicon nanocrystals: A near edge X-ray absorption fine structure (NEXAFS) and X-ray excited optical luminescence (XEOL) study of oxide-embedded and freestanding systems*

* A version of this chapter has been accepted for publication.
Hessel, C. M.; Henderson, E. J.; Kelly, J. A.; Cavell, R. G.; Sham, T. K.; Veinot, J. G. C. *J. Phys. Chem. C.* **2008**, Submission: jp-2008-02095j.

4.1. Introduction

Oxide-embedded silicon nanocrystal (Si-NC) composites and freestanding Si-NCs are unique materials that have been shown to exhibit photoluminescence (PL) in the visible and near-infrared (NIR) regions of the electromagnetic (EM) spectrum.[1-4] Freestanding semiconductor nanocrystals have recently been the focus of intense research in the medical and biological fields due to their potential as *in vivo* fluorescent labels. Many compound semiconductor nanocrystals (e.g., CdSe, ZnS) have been shown to be resistant to photobleaching,[5-7] to have exceptional chemical tunability,[8,9] and can be selectively tailored to act purely as luminescent beacons or as photochemically active species with environment-dependant photophysical characteristics (i.e., sensors).[10] Although compound semiconductor nanocrystals possess very fast radiative recombination rates (i.e., ca. 10^{-9} seconds) and high photoluminescence quantum yields (i.e., ca. 30 – 50 %) throughout the visible spectrum,[11-13] both of which are desirable characteristics for *in vivo* biosensing, the challenges associated with the cytotoxicity of these materials may limit their eventual application.[14,15] In contrast, these challenges have not been identified for silicon-based nanomaterials, including porous silicon,[16] silicon nanowires,[17,18] and luminescent silica nanoparticles,[19] all of which have been shown to be electrochemically stable and non-toxic in biological environments. The methodology of incorporating silica as a biocompatible interface between sensor and sensing media has previously been utilized to isolate CdSe/ZnS or CdS/ZnSe nanocrystals from biologically sensitive environments in an effort to prevent the adverse effects associated with Cd^{2+} leaching.[5] Since Si-NCs are fluorescence chromophores that are resistant to photobleaching and do not exhibit adverse toxicological effects associated

with nanocrystal oxidation, they are an attractive alternative to their compound semiconductor counterparts.

In order to utilize Si-NCs for labeling and sensing applications, surface-modification is required to render the nanocrystals compatible with the sensing medium. Specifically, *in vivo* biosensing requires water-soluble fluorophores that maintain their emission characteristics in the sensing environment and do not aggregate. A variety of water-soluble Si-NCs have been prepared through surface-modification techniques,[20-22] but in most cases the chemical functionalization resulted in unpredictable changes in luminescence properties, typically affecting quantum efficiency and peak emission energy. Although these investigations used different synthetic procedures to produce water-soluble Si-NCs, the functionalization methods were similar, and relied on attachment of the desired chemical moiety through reaction with a surface Si-H bond. Silicon hydride surfaces have previously been shown to be versatile platforms for a variety of functionalization processes on the bulk scale,[23] and have also been examined to a limited extent on the nanoscale, both theoretically and experimentally.[24-26] However, to realize the full potential of Si-NCs as functional materials for fluorescence labeling and sensing, a fundamental investigation of the origin of luminescence from oxide-embedded and freestanding Si-NCs is essential in order to understand how the luminescence characteristics evolve during the Si-NC synthesis and subsequent Si-H surface modification. Identifying the specific chemical species that give rise to Si-NC luminescence in the initial steps of the formation and hydride modification processes would provide a knowledge basis that would aid in predicting how subsequent chemical modification would alter the luminescence properties of Si-NCs.

X-ray excited optical luminescence (XEOL) is an information rich characterization method that has successfully been used to provide insight into the origins of emission within luminescent materials.[27-30] When compared to laser-based methods, the advantage of this technique lies in its ability to simultaneous collect X-ray absorption and optical emission data as the absorption edge of a particular chemical species is scanned using a tunable X-ray excitation source (i.e., a synchrotron). Correlations between the relative quantum yield of a specific chromophore and the X-ray excitation energy can provide information on the local chemical and electronic structure of the chemical species that give rise to the luminescence within a sample.

The impact that XEOL characterization has had on the field of silicon nanomaterials has been significant, with its true potential first being realized during the debate surrounding the origin of luminescence from porous silicon.[31,32] The specificity of the XEOL technique was crucial in disproving an emission model based on siloxene compounds and provided support for the now widely accepted theory that the dominant emission from porous silicon is a result of small (sub-5 nm) crystallites within the sponge-like porous silicon network.[33-38] XEOL has also been utilized to successfully determine the source of luminescence in freestanding silicon nanostructures, including silicon nanowires and alkyl terminated Si-NCs derived from porous silicon.[39-43] Synchrotron-based techniques have also provided unique insight into the electronic structure of oxidized Si-NCs formed by the pyrolyisis of silane.[44] In all the aforementioned XEOL investigations, silicon oxide species were identified as key contributors to the emission characteristics of the resulting silicon nanostructures. These oxide species have been shown to alter the emission profile of the "as-prepared" silicon

nanostructures or manifested new luminescence bands in the optical spectrum. The ease with which bulk silicon surfaces react with ambient oxygen is further accentuated on the nanoscale and thus it is very difficult to obtain silicon nanostructures that are oxide free. Considering the influence silicon oxides have on the emission characteristics of silicon nanostructures, the challenges associated with the rapid oxidation of silicon on the nanometer scale hinder the accurate identification of the luminescent species. Therefore, in an effort to eliminate the effects that silicon oxide species have on the resulting electronic and luminescence characteristics of as-prepared silicon nanomaterials, hydrofluoric acid (HF) etching procedures have been employed prior to X-ray analysis. Not only does HF etching effectively remove the native silicon oxide from the silicon surface, it also passivates it with chemically versatile Si-H bonds, a convenient starting point for further chemical functionalization.

Our group has recently reported the high-yield synthesis of well-defined oxide-embedded Si-NCs with known composition and surface chemistry from the reductive thermal processing of hydrogen silsesquioxane (HSQ).[45,46] The versatility of this precursor has allowed for the production of Si-NCs in a variety of structures/morphologies, including conformal films on flat and non-flat surfaces, sub-100 nm patterns on insulators and semiconductors,[47] bulk composites in gram quantities, and hydride-terminated freestanding Si-NCs that are photoluminescent throughout the visible and NIR regions of the EM spectrum (530 nm - 950 nm). The electronic structure and luminescent characteristics of these materials have been probed by X-ray photoelectron and laser-based PL spectroscopies, however, to date, these properties have never been

measured simultaneously, thus complicating the assignment of the PL emission to specific silicon species.

In this report we provide an interpretation of the silicon K-shell near edge X-ray absorption fine structure (NEXAFS) for oxide-embedded Si-NCs produced by the thermal decomposition of HSQ. We also employ XEOL spectroscopy to selectively excite specific silicon species within our samples in order to gain insight into the species that are responsible for the optical photoluminescence. To determine the influence of surface oxidation on the overall luminescence characteristics, HF etching processes were used to yield oxide-free Si-NCs that were also examined by NEXAFS and XEOL spectroscopy. This investigation provides a report of the origin of luminescence from oxide-embedded and hydride-terminated freestanding Si-NCs derived from HSQ composites.

4.2. Experimental Details

4.2.1. Sample Preparation

Oxide-embedded Si-NC composites used in this study were prepared by the rapid thermal processing of hydrogen silsesquioxane (HSQ), as previously described.[45,46] In brief, HSQ was purchased from Dow Corning as 17 wt% solutions (FOx-17®) and was used as received. To obtain solid HSQ from FOx-17® solutions, solvent was removed *in vacuo* to yield a white solid that was subsequently heated at 18°C/min to a specific temperature, and held for 1 hour in a flowing 5% H_2/95% Ar atmosphere. Samples processed below 1100°C (Table 4.1, Samples **3, 5, 7, 9**) show no sign of crystallinity by

X-ray diffraction (XRD). Increasing the peak processing temperature to 1100°C induces the crystallization of the amorphous silicon clusters formed by the thermally induced disproportionation of HSQ. Transmission electron microscopy (TEM) and XRD have previously shown that the ca. 4 nm diameter diamond structure Si-NCs reside in an encapsulating silica matrix.[45]

Table 4.1: Samples of hydrogen silsesquioxane (HSQ) processed in 5% H_2/95% Ar at specified temperatures and times with a heating rate of 18°C/min. Sample **9** was etched with solutions of 49% HF, water, ethanol, and for specified times to yield Samples **18** and **20**.

Sample ID	Processing Temperature (°C)	Processing Time (hours)
HSQ	N/A	N/A
Sample 3	500	1
Sample 5	700	1
Sample 7	900	1
Sample 9	1100	1
	Etching Conditions 49%HF : water : ethanol	Etching Time (hours)
Sample 18	1:1:1	1
Sample 20	1:1:1	1.5

4.2.2. Hydrofluoric Acid Etching of Oxide-Embedded Silicon Nanocrystal Composites

Oxide-embedded Si-NC composites were etched with solutions of HF to produce freestanding, hydride-terminated Si-NCs. All etching experiments were performed onsite immediately prior to analysis. Semiconductor grade 49% HF (J.T. Baker), 95%

ethanol (Sigma-Aldrich), HPLC grade pentane (Sigma Aldrich) and 10 MΩ·cm Millipore water were used without further purification. The etching procedure consisted of adding 10 mL of a 1:1:1 solution of 49% HF: water: ethanol to 300 mg of mechanically ground composite (Table 4.1, Sample **9**) in a Teflon® beaker. Solutions were stirred for a predetermined time at 300 rpm (Table 4.1, Sample **18, 20**) until the Si-NCs were liberated from the encapsulating silica matrix and the desired nanocrystal size was obtained. Hydrophobic, hydride-terminated Si-NCs were isolated via solvent extraction with two 10 mL aliquots of pentane and were drop cast onto aluminum discs under an inert atmosphere. Samples were quickly transferred under inert atmosphere and reduced temperature to the high vacuum (1×10^{-8} Torr) endstation to prevent surface oxidation.

4.2.3 X-ray Analysis

The spherical grating monochrometer (SGM) undulator beamline 11-ID.1 at the Canadian Light Source (CLS) located in Saskatoon, Saskatchewan provided highly monochromatic X-rays for both NEXAFS and XEOL analyses. The CLS is a third generation synchrotron source that operates at 2.9 GeV, with a 250 mA current upon injection. The photon flux on the high-energy optimized grating at the silicon edge (1839 eV) was ca. 10^{10} photons/second and the resolution was less than 1 eV. The incident photon flux was monitored by an in-line nitrogen ionization chamber. The total electron yield (TEY) was measured by normalizing the sample drained current to the incident photon flux. X-ray fluorescence yield (FLY) was measured using a channel plate detector positioned at a 45° angle from the sample. All oxide-embedded Si-NC composites (Table 4.1, Samples **3, 5, 7, 9**) were freshly ground and mounted on carbon

tape to maintain electrical connectivity, essential for TEY measurements. NEXAFS spectra were calibrated to a powdered silicon wafer standard by setting the first derivative maximum of the Si K-edge absorption to 1839 eV. XEOL measurements involved setting the spherical grating monochrometer to the desired excitation energy and opening the exit slit width to 400 μm to maximize the X-ray photon flux. Measurements were made for a maximum integration time of 20 seconds to minimize the effect of beam exposure on the resulting spectra. Photoluminescence photons were collected though a lens coupled to an Ocean Optics USB4000 or QE65000 spectrometer. The results from both instruments were the same within experimental error. All analyses were conducted in vacuum (1×10^{-8} Torr).

4.2.4 X-ray Photoelectron Spectroscopy (XPS)

XPS measurements were performed at The Alberta Center for Surface Engineering and Science (ACSES). XPS spectra were collected using a Kratos Axis Ultra instrument operating in energy spectrum mode at 210 W. The base pressure and operating chamber pressure was maintained at $\leq 10^{-9}$ Torr. A monochromatic Al K_α source was used to irradiate the samples and the spectra were obtained with an electron take-off angle of 90°. To offset the effects of sample charging a charge neutralizing filament was used during all experiments. Wide survey spectra were collected using an elliptical spot with 2 mm and 1 mm major and minor axis lengths, respectively, and a 160 eV pass energy with a step of 0.33 eV.

4.2.5 X-ray Photoelectron Spectral Analysis

CasaXPS (Vamas) software was used to process high-resolution spectra. All spectra were calibrated to the C1s emission (284.8eV) arising from adventitious surface contamination. After calibration, the background from each spectrum was subtracted using a Shirley-type background to remove most of the extrinsic loss structure.[48] The high-resolution Si 2p region of spectra collected for Sample **9** (Table 4.1) was fit to Si $2p_{1/2}$ Si $2p_{3/2}$ partner lines with spin-orbit splitting fixed at 0.6 eV and the Si $2p_{1/2}$ Si $2p_{3/2}$ intensity ratio was set to ½.

4.3. Results and Discussion

To understand the evolution of the silicon electronic structure resulting from the thermal disproportionation of HSQ, NEXAFS spectra were examined as a function of processing temperature. Figure 4.1 shows the normalized FLY spectra at the silicon K-edge for samples of HSQ thermally processed from 500°C to 1100°C. The fluorescence spectrum for unprocessed HSQ contains a dominant edge feature at 1845 eV and a second feature at 1847 eV. Comparing these features to the absorption energies of silicon in an elemental, (1841 eV, Figure 4.1, Si standard) and fully oxidized environment, (1848 eV, Figure 4.1, SiO_2 standard), it is clear that the silicon in HSQ exists predominantly as a silicon suboxide, SiO_x ($0 < x < 2$). This is consistent with the empirical formula of HSQ ($SiO_{1.5}H$) in which each silicon atom is ideally bonded to three oxygen atoms and one hydrogen atom (Figure 4.2). In accordance with these findings, silicon suboxides in porous silicon have been previously shown to absorb soft X-rays in the intermediate energy region between the silicon and silica absorption features.[37]

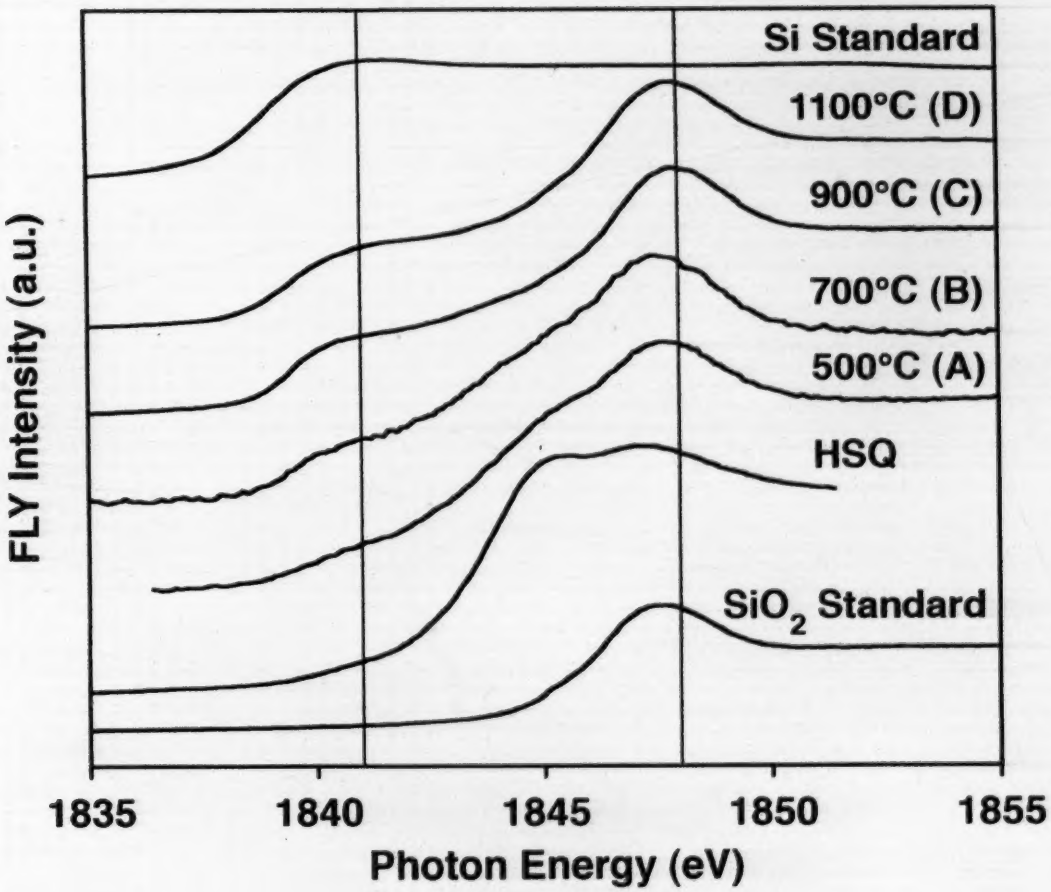

Figure 4.1. Normalized FLY Si K-edge NEXAFS spectra for HSQ thermally processed between 500°C and 1100°C for 1 hour in 5% H_2/95% Ar. FLY spectra are also included for SiO_2 and elemental Si standards for comparison. The fluorescence maxima for Si and SiO_2, 1841 eV and 1848 eV respectively, are noted for reference. Spectra have been shifted vertically for clarity.

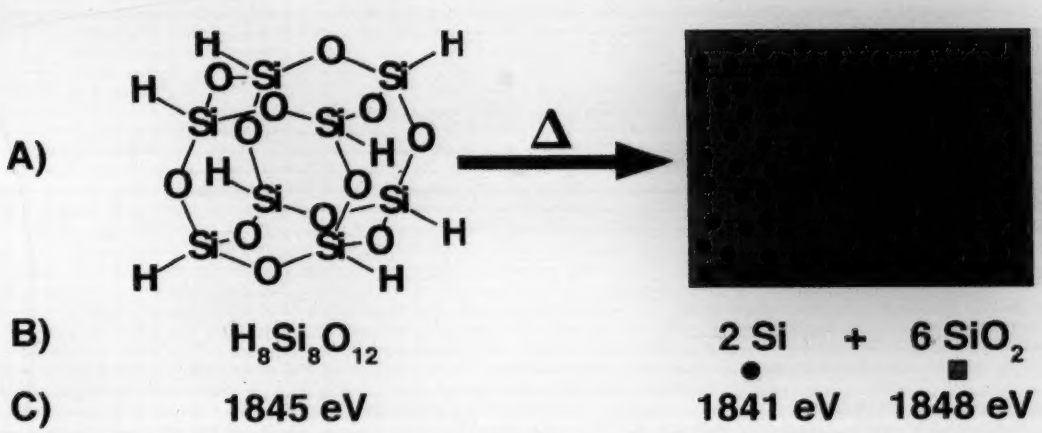

Figure 4.2. A) Schematic of the thermal degradation of HSQ to form oxide-embedded Si-NCs. B & C) HSQ has a theoretical silicon to oxygen ratio of 1 to 1.5, and a Si K-edge absorption maximum at 1845 eV, an energy between that of the products, elemental Si (1841 eV) and SiO_2 (1848 eV).

The evolution of the absorption Si edge (Figure 4.1) as a function of processing temperature is consistent with the progression of a thermally-induced HSQ disproportionation reaction to form elemental Si clusters in a SiO_2-like matrix, Figure 4.2. As the processing temperature is increased above 500°C, the silicon suboxide absorption at 1845 eV in HSQ steadily decreases in intensity while the absorption feature arising from silicon in a SiO_2-like environment (1847 eV) intensifies and shifts toward the theoretical absorption energy for SiO_2, 1848 eV. Most importantly, there is a concomitant emergence of an absorption feature at 1841 eV which increases in intensity with temperature and is consistent with the continual formation of elemental silicon. When HSQ is processed at 1100°C (Figure 4.1, Sample **9**) the X-ray absorption spectrum contains only two absorption features, characteristic of elemental Si (1841 eV) and SiO_2 (1848 eV). This verifies our previous studies that showed that processing HSQ at

elevated temperatures induces a thermal disproportionation and results in the formation of elemental silicon domains in a SiO_2-like matrix.[45] In order to examine the correlations between specific silicon species in the system and the optical luminescence, the exact energy of all absorption features on the Si K-edge is essential prior to XEOL analysis.

As previously mentioned, XEOL is an effective method for assigning the species responsible for emission from luminescent silicon nanostructures with multiple chemical species and emission bands.[39,41] As such, it is an ideal characterization technique for determining the origins of luminescence from oxide-embedded Si-NCs derived from HSQ. The selectivity of XEOL spectroscopy arises from the ability to tune incident X-rays to the resonant absorption energy of a specific chemical species, thus maximizing its absorption cross-section and resulting in the preferential absorption of a majority of the incoming photons. If the selected species has luminescence properties, this preferential absorption leads to an increase in the quantum yield and results in an enhancement of the associated emission band. If multiple emission bands are present in the optical spectrum, the increase in relative quantum yield leads to an increase in the emission intensity with respect to other luminescence bands in the spectrum. When this relative spectral intensity enhancement is correlated to the incident X-ray energy, the chemical environment of the emitting species can be identified. Although previous studies have simultaneously measured the optical emission as the absorption edge energy is scanned, a technique known as optical X-ray absorption fine structure (optical XAFS) spectroscopy, this method was not employed for the present study due to sample degradation resulting from prolonged beam exposure. XEOL spectra were instead collected with 20 second integration times. Unprocessed HSQ, and samples processed at or below 900°C (Table

4.1, **3**, **5**, **7**, **9**) show no sign of visible luminescence upon X-ray excitation. This is consistent with non-luminescent amorphous silicon nanodomains previously identified in HSQ composites prior to Si-NC formation.[46] Samples processed at 1100°C, however, exhibit two intense emission bands in the visible region of the EM spectrum centered at 540 nm and 780 nm, Figure 4.3. XEOL spectra were initially collected with excitation energies of 1836 eV and 1852 eV, energies that are below the Si absorption feature at 1841 eV, and above the SiO_2 feature at 1848 eV, respectively, and will hereafter be referred to as "background spectra". Obtaining XEOL spectra with excitation energies on either side of these absorption features provides emission spectra that do not have biased quantum yields resulting from enhanced absorption by either silicon species. Excitation at an energy below the Si absorption feature (< 1841 eV) results in the non-discriminant promotion of electrons with lower binding energies to continuum states (i.e., valence, Si 2p, and O 1s). Optical luminescence in the visible region of the EM spectrum results when a fraction of these excited state electrons radiatively recombine with vacancies in the top of the valence band. When the XEOL spectrum is collected at an excitation energy of 1852 eV, above the Si K-edge absorption energy, neither silicon species (i.e., Si and SiO_2) preferentially absorb a majority of the incoming photons. The emission spectrum still remains indiscriminant even though the excitation threshold for all silicon species in the sample is surpassed, and the optical spectrum now contains contributions from all decay processes associated with the removal of Si 1s electrons.

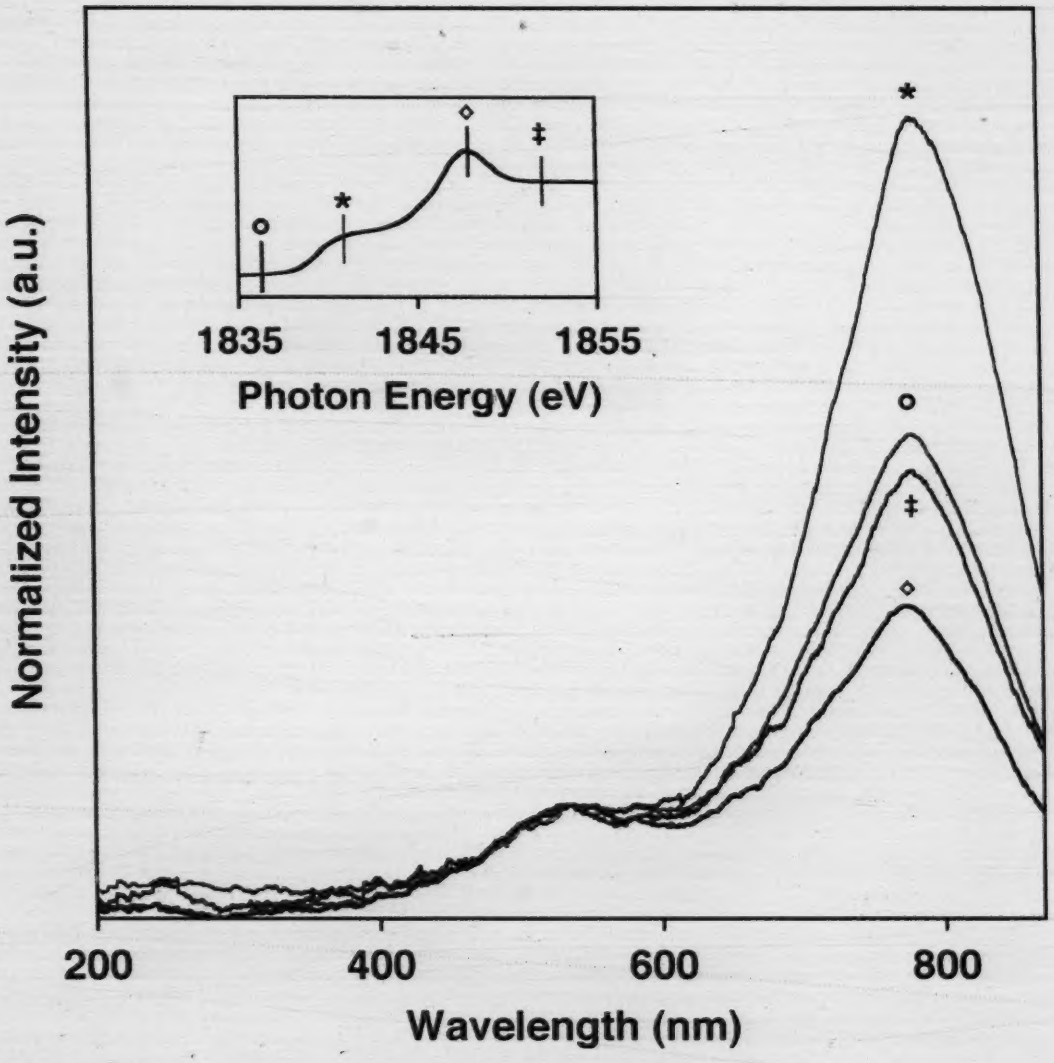

Figure 4.3. Normalized X-ray excited optical luminescence (XEOL) spectra of Sample 9. The inset indicates the selected X-ray excitation energy for each XEOL spectrum with respect to the NEXAFS spectrum. The spectra are normalized to the intensity maximum of the 540 nm emission peak to clearly indicate how the intensity of the emission bands change as a function of excitation energy.

XEOL spectra were collected at excitation energies resonant with the Si and SiO_2 absorption features at the Si K-edge to examine any correlations between the silicon species present in the sample and the two emission bands identified in the optical emission spectrum. When the excitation energy is set to the Si absorption at 1841 eV there is a dramatic increase in relative intensity for the emission band at 780 nm, with respect to the two background spectra, Figure 4.3. When exciting at this energy, the elemental Si-NCs absorb a majority of the photons, resulting in the formation of a greater number of valence band vacancies in the Si-NCs. The holes in the valence band are formed by a variety of processes after the initial absorption of an X-ray photon, including Auger cascades, photoemission events and inelastic energy losses from high-energy electrons during atomic relaxation. Therefore, the relative intensity increase in the emission band at 780 nm, with respect to the band at 540 nm, suggests that the emission at 780 nm is of elemental Si origin and results from radiative recombination of electrons and holes within the Si-NC core. Other forms of elemental silicon have also been shown to exhibit luminescence in the low energy region of the visible spectrum, with emission bands from porous silicon reported at 600 nm and 640 nm when excited at the silicon K and L-edges, respectively.[35,37] When compared to the emission energy from the present ca. 4 nm silicon crystals formed from HSQ thermally processed at 1100°C, porous silicon samples emit at higher energies due to the smaller (1.5 – 2.5 nm)[31] Si-NCs within the porous matrix. This is expected from quantum confinement theory.

The XEOL spectrum acquired when exciting at the SiO_2 absorption feature (1848 eV) shows relative intensity changes in the emission bands as a result of the shift to higher X-ray excitation energy. Specifically, a greater intensity is observed for the

emission band at 540 nm while the emission band at 780 nm is suppressed, Figure 4.3. Considering the spectra in Figure 4.3 are normalized to the intensity of the 540 nm emission band, an intensity enhancement of this band is seen as a suppression of the 780 nm band to a level below the background spectral intensity. This intensity enhancement is a result of tuning the X-ray energy to the absorption cross-section maximum for silicon oxide species at 1848 eV, which leads to the preferential absorption of a majority of the incoming photons. As such, the total XEOL emission consists of a greater contribution from luminescent silicon oxide species. The correlation between excitation energy and emission intensity for the 540 nm and 780 nm emission bands suggests that the emission band at 540 nm has silicon oxide origins, whereas the emission band at 780 nm arises from elemental Si-NCs.

The presence of a high-energy emission band in XEOL investigations of silicon nanomaterials is common, and is typically attributed to silicon oxide species formed by the rapid surface oxidation of silicon under ambient conditions. Emission bands in the visible and UV regions of the EM spectrum have been reported from defective silicon oxide,[35,49] suboxides, and neutral oxide vacancies depending on the method of synthesis and the resulting sample homogeneity. [39,50] Considering the variety of oxide-related species reported to emit at visible and UV energies, it is important to note that both emission bands identified in the present study were observed simultaneously, and emerged as a result of increasing the processing temperature of HSQ from 900°C to 1100°C, in parallel with the transition of amorphous silicon to crystalline silicon. In this temperature region, the clusters of elemental silicon formed by the decomposition of HSQ crystallize in the SiO_2-like matrix. Therefore the high energy emission band (540

nm) in the XEOL spectrum for HSQ processed at 1100°C is a direct result of the nanocrystal formation process and is attributed to the interface between the nanocrystal core and the surrounding SiO_2 matrix. The local electronic information provided by the NEXAFS data shows only two discernable features separated by a non-zero intermediate region (Figure 4.1, Sample **9**). This is consistent with Sample **9** containing predominantly Si and SiO_2, with a small amount of silicon suboxides, SiO_x ($0 < x < 2$). These observations suggest there is a well-defined interface between the Si-NCs and the surrounding SiO_2 matrix. These findings are in accordance with previous photoemission and theoretical studies on Si/SiO_2 interfaces formed in controlled, high temperature environments that showed a defect free transition between the elemental silicon and surrounding oxide matrix, and contained only minimal suboxide species.[51] These results differ from the findings of Daldosso and coworkers that reported a graded transition region (ca. 1 nm) between the nanocrystal core and the surrounding oxide matrix in samples of oxide-embedded Si-NCs.[52] The preparative method reported by Daldosso involved the PECVD of silicon oxide to produce thin films of SiO_x that were subsequently thermally processed in a nitrogen environment to generate oxide-embedded Si-NCs. Although their method differs from the present synthesis, the resulting oxide-embedded Si-NCs appear to be very similar. To determine if the wide graded interfacial region identified by Daldosso is applicable to the present system, or a result of the preparative method, an additional XPS analysis was performed in an effort to evaluate the presence of intermediate oxides in samples of HSQ processed at 1100°C. Figure 4.4 shows the high resolution XP spectrum of the Si 2p region for Sample **9**.

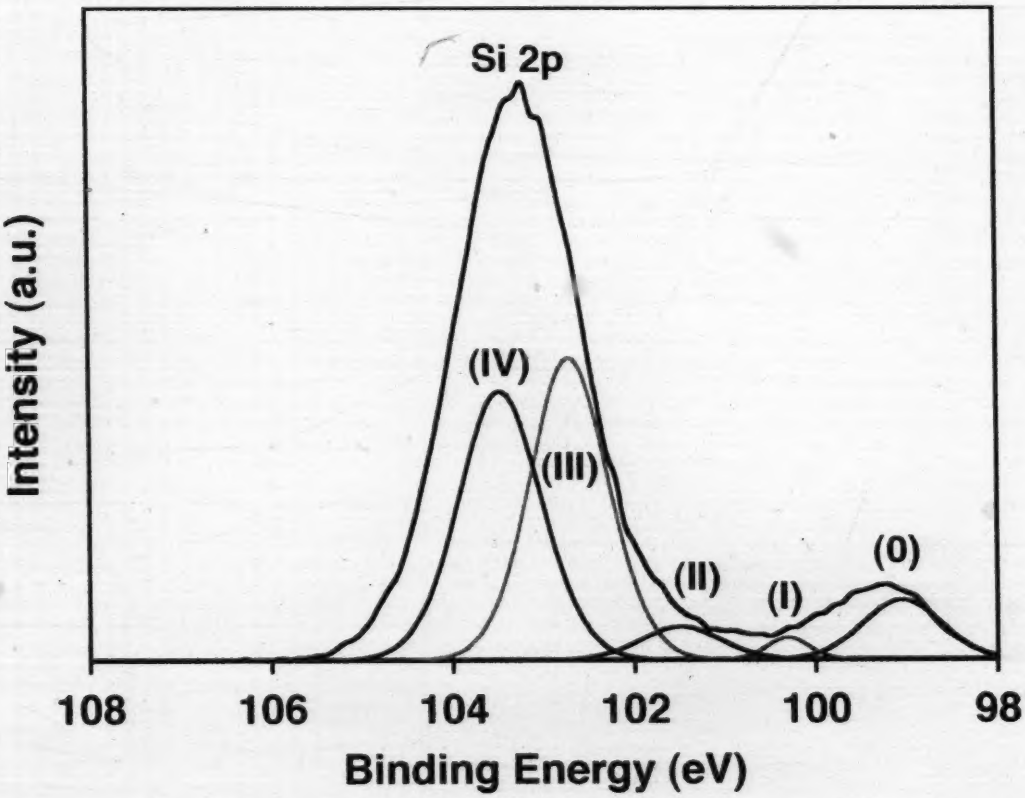

Figure 4.4. Shirley background subtracted high-resolution XP spectrum of the Si 2p region for Sample **9**. For clarity, the Si $2p_{1/2}$ spin-orbit couple partner lines have been omitted. All silicon oxide species, $Si^{(n)}$ (n = 0 – IV) are labeled for clarity.

The Shirley background subtracted fit contains the Si $2p_{1/2}$ and Si $2p_{3/2}$ partner lines for $Si^{(n)}$ (n = 0 – IV) however, the Si $2p_{1/2}$ fitting has been omitted in Figure 4.4 for clarity. The spectrum shows two emission peaks separated by a non-zero baseline at 99.3 eV and 103.2 eV that are predominantly attributed to $Si^{(0)}$ and a combination of $Si^{(III)}$ and $Si^{(IV)}$, respectively. The non-zero baseline indicates there are intermediate, low oxidation silicon species ($Si^{(I)}$ & $Si^{(II)}$) present, which is inevitable when transitioning from the elemental Si nanocrystal to the SiO_2 matrix, but the occurrence of these species are limited. The prevalence of $Si^{(III)}$ and $Si^{(IV)}$ species at the interface is also in accordance with previous theoretical and experimental investigations of the atomic population and depth distribution of silicon oxides at Si/SiO_2 interfaces.[51] Therefore, the XPS data, in conjunction with the NEXAFS data, which also shows very minimal intermediate silicon oxides, indicate that the wide graded Si/SiO_2 interface is inherent to the Daldosso synthesis and is not pertinent to the present system. The large proportion of surface silicon atoms relative to the number of core atoms, due to the small size of the Si-NCs, results in a distinct interfacial species with emission characteristics heavily influenced by the surrounding oxide matrix. This electronic influence causes an increase in the excitation energy required for the interfacial species to emit,[35,43] and is likely the reason that the high-energy emission (540 nm) was not observed during previous low energy (λ_{ex} = 325 nm) laser-based PL studies on identical materials.[45,46] This observation alone highlights the need for X-ray based spectroscopy as a definitive technique when determining the origins of emission from luminescent materials that contain multiple luminescence pathways.

Although TEY has superior surface sensitivity over FLY, in the case of nanomaterials, thickness effects are not as apparent since the sizes of the structures are typically below the attenuation length of the X-ray fluorescence photons. The sampling depths for TEY and FLY measurements in silicon materials have previously been determined to be ca. 70 nm to several hundred nm, respectively, at Si K-shell absorption energies (1830 eV – 1900 eV). The oxide-embedded samples in the present study have grain sizes of ca. 1 – 5 μm as established by scanning electron microscopy (SEM), which are greater than the sampling depth of X-ray fluorescence photons in silicon materials. Therefore, to determine the technique best suited for detection and representation, the TEY and FLY for both the oxide-embedded and freestanding systems were compared. Figure 4.5 shows the comparison between the TEY and FLY data for mechanically ground HSQ processed at 1100°C (Sample **9**). The signal for SiO_2 (1848 eV) in the TEY is enhanced with respect to that of the FLY, likely a result of matrix and surface oxides that are exposed during mechanical grinding. The comparison indicates that the TEY signal is notably influenced by surface species and the FLY provides accurate information on the electronic structure of silicon both above and below the particle surface. A similar comparison of the TEY and FLY for oxide-free Si-NCs (Sample **20**) produced by HF etching of Sample **9** is also shown in Figure 4.5. Both spectra of the sub-5 nm freestanding Si-NCs are very similar in appearance and only show the presence of elemental silicon. Therefore the data for the discussion of freestanding system is presented in the FLY form to maintain consistency.

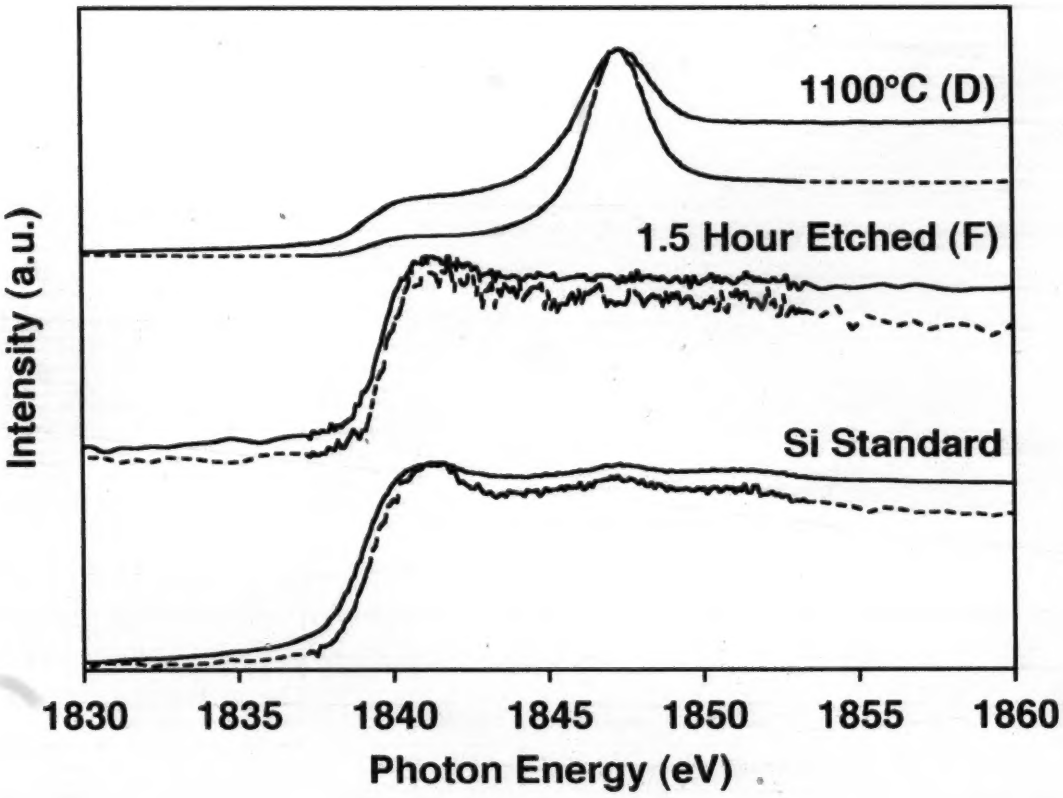

Figure 4.5. Comparison of the Si K-edge TEY (dotted trace) and FLY (solid trace) spectra for oxide-embedded Si-NCs (Sample **9**), HF prepared freestanding Si-NCs (Sample **20**) and, a ground silicon wafer standard. Spectra have been shifted vertically for clarity.

In order to provide additional confirmation for the assignments of the two emission bands in the XEOL spectra, an HF etching procedure was employed to liberate the Si-NCs from the oxide matrix and eliminate the influences that silicon oxides have on the electronic and optical characteristics of the system. HF is an effective etchant that reacts rapidly with SiO_2 and has also been shown to react with silicon.[1,45] In the case of oxide-embedded Si-NCs, HF etching quickly (ca. 50 mins) removes the oxide matrix and slowly decreasing the Si-NC size during prolonged exposure. As previously mentioned, HF has been used with varied effectiveness in other silicon-based XEOL studies in an effort to obtain optical spectra free of the influences of silicon oxides.[37,39] In the present study, ground samples of Sample **9** were etched with 1:1:1 solutions of 49% HF: water: ethanol to yield oxide-free hydride-terminated freestanding Si-NCs. To ensure the hydride-terminated nanocrystals did not oxidize after the etching process, special handling precautions were taken during all preparation steps. After the oxide removal was complete, the hydride-terminated Si-NCs were handled under a nitrogen atmosphere and kept at reduced temperature to prevent surface oxidation prior to introduction in the vacuum analysis chamber. The total time from extraction of the Si-NCs from the etching solution to introduction into the high vacuum (1×10^{-8} torr) endstation was less than 5 minutes. The efforts taken to prevent oxidation of freestanding Si-NCs were successful, as reflected by the silicon K-edge NEXAFS spectra (Figure 4.6) that show negligible signal for silicon oxide species. When the FLY NEXAFS spectra of the unetched oxide-embedded Si-NCs and freestanding Si-NCs are compared, the absence of the SiO_2 absorption feature at 1848 eV in the spectrum for freestanding Si-NCs is consistent with the complete removal of all silicon oxide species. The absorption feature at 1841 eV,

attributed to elemental silicon, remains the only feature on the absorption edge to the sensitivity of TEY and FLY measurements (*vide supra*). To our knowledge, this is the first report in which NEXAFS and XEOL data has been successfully collected for oxide-free Si-NCs. Eliminating the electronic effects induced by the encapsulating SiO_2 matrix is of extreme importance since any associated effects in the XEOL spectra resulting from silicon oxides are also removed. Therefore, evaluating the emission characteristics of oxide-free Si-NCs is a necessary step for the verification of the emission band assignments.

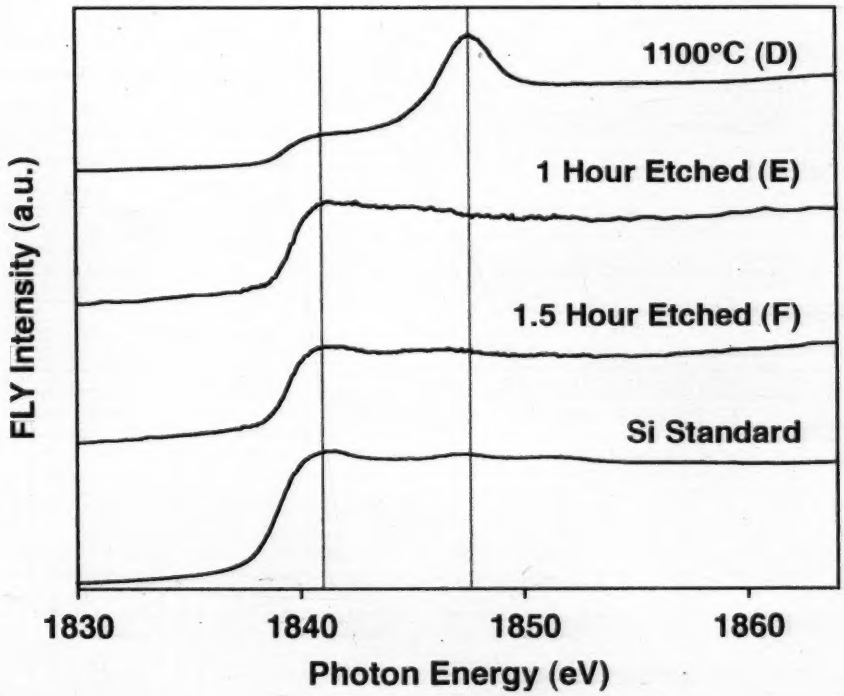

Figure 4.6. Normalized FLY Si K-edge NEXAFS spectra of hydride-terminated freestanding Si-NCs produced by etching composites of oxide-embedded silicon nanocrystals for specified times in solutions of HF. Spectra for Sample **9** and a silicon wafer standard are included for reference. The absorption maxima for Si and SiO_2, 1841 eV and 1848 eV respectively, are noted for reference. Spectra have been shifted vertically for clarity.

To examine the post-etching emission characteristics of oxide-free Si-NCs, XEOL measurements were collected at an excitation energy of 1841 eV, the only remaining absorption feature on the silicon K-edge, corresponding to the absorption energy of elemental silicon. Figure 4.7 shows the normalized XEOL spectra of Samples **18** and **20** that were etched in solutions of HF for 1 and 1.5 hours, respectively, to yield hydride-terminated Si-NCs. In comparison with the optical spectrum of Sample **9** it is clear from the emission profile of the etched samples that the low-energy emission remains, and the high-energy emission previously at 540 nm is completely absent. This observation indicates the removal of matrix and interfacial oxides in the Si-NC samples through HF etching eliminated the high-energy luminescence pathway. Since it is the emission at 540 nm that disappears upon removal of the oxide, the conclusion that this emission results from an oxide influenced emission process at the Si/SiO_2 interface is further strengthened.

The XEOL observations from the two etched samples also provide vital information necessary to confirm the origin of emission of the low-energy spectral feature. After 1 hour in the etching solution the oxide matrix is completely removed and the Si-NCs are slightly reduced in size, causing the emission band to narrow and shift to a lower peak wavelength of 700 nm. When the Si-NCs are further reduced in size by an additional 0.5 hours in the etching solution, the trend in increasing emission energy with decreasing particle size continues, and the resulting emission shifts to 530 nm. The shift of the emission to higher energy and the narrowing of its profile with a concomitant decrease in nanocrystal size confirms that the origin of the low-energy emission is a

result of quantum confinement effects in sub-5 nm freestanding hydride-terminated Si-NCs.

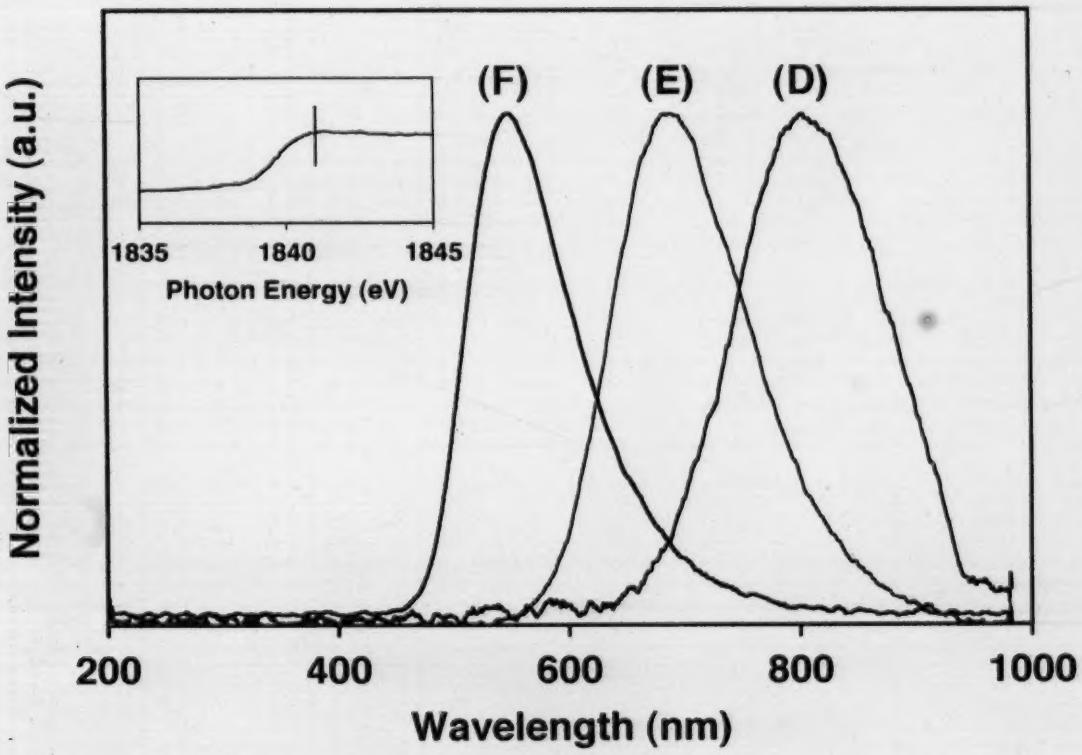

Figure 4.7. Normalized X-ray excited optical luminescence (XEOL) spectra of oxide-embedded silicon nanocrystals (Sample **9**) and hydride-terminated freestanding silicon nanocrystals produced by etching composites of for 1 hour (Sample **18**) and 1.5 hours (Sample **20**) with solutions of hydrofluoric acid. The inset depicts the X-ray excitation energy for each XEOL spectrum at 1841 eV.

4.4. Conclusion

NEXAFS spectroscopy was used to monitor the thermal decomposition of HSQ and identified only two predominant silicon species at the peak processing temperature of 1100°C, corresponding to elemental Si-NCs and an encapsulating SiO_2 matrix. It was also found that the interface between the nanocrystal surface and the encapsulating matrix was well-defined, containing minimal suboxide species. XEOL spectroscopy of oxide-embedded Si-NCs yielded two emission bands in the visible spectrum, a low energy band at 780 nm and a high energy band at 540 nm that had previously not been observed with low energy laser-based spectroscopy. Variable excitation XEOL spectra show a correlated quantum yield enhancement of the low energy emission band with the elemental silicon absorption at 1841 eV, and an enhancement of the high-energy emission band at the SiO_2 absorption at 1848 eV. An HF etching procedure was employed to remove matrix and surface oxides to produce oxide-free freestanding Si-NCs, as confirmed by post-etching NEXAFS spectra. The correlated loss of the high energy emission band at 540 nm as a result of oxide removal supports the assignment of this band to interfacial electronic effects of the encapsulating silicon oxide matrix on the optical properties of the Si-NCs. Hydride-terminated freestanding Si-NCs of decreasing size exhibited a blue-shift in the emission energy of the 780 nm emission band, confirming that this emission is a result of quantum confinement processes in Si-NCs. This report further establishes quantum confined emission processes as the governing radiative pathway in oxide-free, hydride terminated Si-NCs, and highlights the electronic influence of Si-NC surface chemistry on the resulting emission characteristics of Si-NCs. It also provides a fundamental understanding of the emission characteristics for hydride-

terminated Si-NCs, a common reaction platform for further chemical modification. From the conclusions established in this investigation the emission characteristics associated with surface modification can be predicted and tailored for specific sensing environments.

4.5. References

(1) Li, X.; He, Y.; Talukdar, S. S.; Swihart, M. T. *Langmuir* **2003**, *19*, 8490.

(2) Pettigrew, K. A.; Liu, Q.; Power, P. P.; Kauzlarich, S. M. *Chem. Mater.* **2003**, *15*, 4005.

(3) Mangolini, L.; Kortshagen, U. *Adv. Mater.* **2007**, *19*, 2513.

(4) Wilcoxon, J. P.; Samara, G. A. *Appl. Phys. Lett.* **1999**, *74*, 3164.

(5) Bruchez Jr, M.; Moronne, M.; Gin, P.; Weiss, S.; Alivisatos, A. P. *Science* **1998**, *281*, 2016.

(6) Chan, W. C. W.; Nie, S. *Science* **1998**, - *281*.

(7) Green, M. *Angew. Chem. Int. Ed.* **2004**, *43*, 4129.

(8) Uyeda, H. T.; Medintz, I. L.; Jaiswal, J. K.; Simon, S. M.; Mattoussi, H. *J. Am. Chem. Soc.* **2005**, *127*, 3870.

(9) Michalet, X.; Pinaud, F. F.; Bentolila, L. A.; Tsay, J. M.; Doose, S.; Li, J. J.; Sundaresan, G.; Wu, A. M.; Gambhir, S. S.; Weiss, S. *Science* **2005**, *307*, 538.

(10) Somers, R. C.; Bawendi, M. G.; Nocera, D. G. *Chem. Soc. Rev.* **2007**, *36*, 579.

(11) Murray, C. B.; Norris, D. J.; Bawendi, M. G. *J. Am. Chem. Soc.* **1993**, *115*, 8706.

(12) Wu, F.; Zhang, J. Z.; Kho, R.; Mehra, R. K. *Chem. Phys. Lett.* **2000**, *330*, 237.

(13) Dabbousi, B. O.; Rodriguez-Viejo, J.; Mikulec, F. V.; Heine, J. R.; Mattoussi, H.; Ober, R.; Jensen, K. F.; Bawendi, M. G. *J. Phys. Chem. B* **1997**, *101*, 9463.

(14) Derfus, A. M.; Chan, W. C. W.; Bhatia, S. N. *Nano Lett.* **2004**, *4*, 11.

(15) Jaiswal, J. K.; Simon, S. M. *Trends Cell Bio.* **2004**, *14*, 504.

(16) Canham, L. T.; Reeves, C. L.; Newey, J. P.; Houlton, M. R.; Cox, T. I.; Buriak, J. M.; Stewart, M. P. *Adv. Mater.* **1999**, *11*, 1505.

(17) Cui, Y.; Wei, Q.; Park, H.; Lieber, C. M. *Science* **2001**, *293*, 1289.

(18) Nagesha, D. K.; Whitehead, M. A.; Coffer, J. L. *Adv. Mater.* **2005**, *17*, 921.

(19) Jin, Y.; Kannan, S.; Wu, M.; Zhao, J. X. *Chem. Res. Toxicol.* **2007**, *20*, 1126.

(20) Li, X.; He, Y.; Swihart, M. T. *Langmuir* **2004**, *20*, 4720.

(21) Warner, J. H.; Hoshino, A.; Yamamoto, K.; Tilley, R. D. *Angew. Chem. Int. Ed.* **2005**, *44*, 4550.

(22) Rogozhina, E. V.; Eckhoff, D. A.; Gratton, E.; Braun, P. V. *J. Mater. Chem.* **2006**, *16*, 1421.

(23) Buriak, J. M. *Chem. Rev.* **2002**, *102*, 1271.

(24) Zhou, Z.; Friesner, R. A.; Brus, L. *J. Am. Chem. Soc.* **2003**, *125*, 15599.

(25) Zhou, Z.; Brus, L.; Friesner, R. *Nano Letters* **2003**, *3*, 163.

(26) Wolkin, M. V.; Jorne, J.; Fauchet, P. M.; Allan, G.; Delerue, C. *Phys. Rev. Lett.* **1999**, *82*, 197.

(27) Hu, Y. F.; Tan, K. H.; Kim, P. S.; Zhang, P.; Naftel, S. J.; Sham, T. K.; Coulthard, I.; Yates, B. W. *Rev. Sci. Instrum.* **2002**, *73*, 1379.

(28) Kim, P. S.; Sham, T. K.; Zhang, P.; Fung, M. K.; Lee, S. T.; Hu, Y. F.; Yates, B. W. *J. Am. Chem. Soc.* **2001**, *123*, 8870.

(29) Zhang, P.; Naftel, S. J.; Sham, T. K. *J. Appl. Phys.* **2001**, *90*, 2755.

(30) Armelao, L.; Heigl, F.; Jurgensen, A.; Blyth, R. I. R.; Regier, T.; Zhou, X. T.; Sham, T. K. *J. Phys. Chem. C* **2007**, *111*, 10194.

(31) Sham, T. K.; Jiang, D. T.; Coulthard, I.; Lorimer, J. W.; Feng, X. H.; Tan, K. H.; Frigo, S. P.; Rosenberg, R. A.; Houghton, D. C.; Bryskiewicz, B. *Nature* **1993**, *363*, 331.

(32) Cullis, A. G.; Canham, L. T.; Calcott, P. D. J. *J. Appl. Phys.* **1997**, *82*, 909.

(33) Deak, P.; Rosenbauer, M.; Stutzmann, M.; Weber, J.; Brandt, M. S. *Phys. Rev. Lett.* **1992**, *69*, 2531.

(34) Brandt, M. S.; Fuchs, H. D.; Stutzmann, M.; Weber, J.; Cardona, M. *Solid State Commun.* **1992**, *81*, 307.

(35) Coulthard, I.; Jiang, D. T.; Sham, T. K. *J. Electron. Spectrosc. Relat. Phenom.* **1996**, *79*, 233.

(36) Coulthard, I.; Sham, T. K. *Solid State Commun.* **1999**, *110*, 203.

(37) Coulthard, I.; Antel Jr, W. J.; Freeland, J. W.; Sham, T. K.; Naftel, S. J.; Zhang, P. *Appl. Phys. Lett.* **2000**, *77*, 498.

(38) Gardelis, S.; Bangert, U.; Hamilton, B.; Pettifer, R. F.; Hill, D. A.; Keyse, R.; Teehan, D. *Appl. Surf. Sci.* **1996**, *102*, 408.

(39) Sun, X. H.; Wong, N. B.; Li, C. P.; Lee, S. T.; Sham, T. K. *J. Appl. Phys.* **2004**, *96*, 3447.

(40) Sun, X. H.; Tang, Y. H.; Zhang, P.; Naftel, S. J.; Sammynaiken, R.; Sham, T. K.; Peng, H. Y.; Zhang, Y. F.; Wong, N. B.; Lee, S. T. *J. Appl. Phys.* **2001**, *90*, 6379.

(41) Sham, T. K.; Naftel, S. J.; Kim, P. S. G.; Sammynaiken, R.; Tang, Y. H.; Coulthard, I.; Moewes, A.; Freeland, J. W.; Hu, Y. F.; Lee, S. T. *Phys. Rev. B: Condens. Matter* **2004**, *70*.

(42) Chao, Y.; Houlton, A.; Horrocks, B. R.; Hunt, M. R. C.; Poolton, N. R. J.; Yang, J.; Siller, L. *Appl. Phys. Lett.* **2006**, *88*.

(43) Chao, Y.; Krishnamurthy, S.; Montalti, M.; Lie, L. H.; Houlton, A.; Horrocks, B. R.; Kjeldgaard, L.; Dhanak, V. R.; Hunt, M. R. C.; Siller, L. *J. Appl. Phys.* **2005**, *98*, 1.

(44) Schuppler, S.; Friedman, S. L.; Marcus, M. A.; Adler, D. L.; Xie, Y. H.; Ross, F. M.; Chabal, Y. J.; Harris, T. D.; Brus, L. E.; Brown, W. L.; Chaban, E. E.; Szajowski, P. F.; Christman, S. B.; Citrin, P. H. *Phys. Rev. B: Condens. Matter* **1995**, *52*, 4910.

(45) Hessel, C. M.; Henderson, E. J.; Veinot, J. G. C. *Chem. Mater.* **2006**, *18*, 6139.

(46) Hessel, C. M.; Henderson, E. J.; Veinot, J. G. C. *J. Phys. Chem. C* **2007**, *111*, 6956.

(47) Hessel, C. M.; Summers, M. A.; Meldrum, A.; Malac, M.; Veinot, J. G. C. *Adv. Mater.* **2007**, *19*, 3513.

(48) Norgren, B. S.; Somers, M. A. J.; de Wit, J. H. W. *Surf. Interface Anal.* **1994**, *21*, 381.

(49) Kovalev, D. I.; Yaroshetzkii, I. D.; Muschik, T.; Petrova-Koch, V.; Koch, F. *Appl. Phys. Lett.* **1994**, *64*, 214.

(50) Yu, D. P.; Hang, Q. L.; Ding, Y.; Zhang, H. Z.; Bai, Z. G.; Wang, J. J.; Zou, Y. H.; Qian, W.; Xiong, G. C.; Feng, S. Q. *Appl. Phys. Lett.* **1998**, *73*, 3076.

(51) Luh, D. A.; Miller, T.; Chiang, T. C. *Phys. Rev. Lett.* **1997**, *79*, 3014.

(52) Daldosso, N.; Luppi, M.; Ossicini, S.; Degoli, E.; Magri, R.; Dalba, G.; Fornasini, P.; Grisenti, R.; Rocca, F.; Pavesi, L.; Boninelli, S.; Priolo, F.; Spinella, C.; Iacona, F. *Phys. Rev. B: Condens. Matter* **2003**, *68*, 853271.

Chapter 5:

Direct patterning, conformal coating, and erbium doping of luminescent Si-NC/SiO_2 thin films from solution processable hydrogen silsesquioxane*

---

* A version of this chapter has been published.
Hessel, C. M.; Summers, M. A.; Meldrum, A.; Malac, M.; Veinot, J. G. C. *Adv. Mater.* **2007**, *19*, 3513.

5.1. Introduction

Silicon nanomaterials such as porous silicon (*p*-Si),[1] freestanding silicon nanocrystals (Si-NCs),[2] as well as those embedded in a silicon oxide matrix (Si-NC/SiO_2)[3] have been the foci of numerous investigations in recent years. Part of the interest in these materials stems from their potential application in photonic devices such as waveguide amplifiers,[4] light emitting diodes (LEDs),[5] or potentially a silicon nanocrystal laser.[6] Beyond optical applications, Si-NC/SiO_2 composites have also shown promise as a material for flash memory applications.[7]

Inherent in many device fabrication methods is the requirement to pattern or locate the Si-NCs in the appropriate structure – a process that often involves multiple lithographic steps in which several problems can occur. In the present work, a new method overcomes many of these issues and provides a uncomplicated way to produce finely patterned Si-NC arrays. Furthermore, the method is compatible with the application of Si-NCs as sensitizers for the 1.5 μm fluorescence of Er^{3+}, which is of special interest in the nascent field of silicon microphotonics.[8]

Fabrication methods demonstrated to date generally involve either physical or chemical vapor deposition or ion implantation to produce SiO_x films, which are then treated at or above 1000 °C to induce the nucleation, growth, and crystallization of oxide-embedded Si-NCs. In many device structures (*e.g.*, waveguides) the film must be subsequently patterned using a resist and various etching techniques. Features are often limited to sizes greater than a few microns, and sidewall roughness in silicon nanocrystal waveguides remains a significant issue.[9] Additionally, none of the standard physical deposition methods afford straightforward coating of non-planar surfaces. In an effort to

exploit the benefits of solution processability, methods in which *p*-Si is pulverized and added to a spin-on or sol-gel glasses were reported.[10,11] Still, these mixing procedures must overcome challenges such as limited chemical tunability, material inhomogeneity, and phase separation.

In chapter 2 we have shown the bulk synthesis of Si-NC/SiO_2 composites in near quantitative yield via the reductive thermal processing of hydrogen silsesquioxane (Figure 5.1a).[12] HSQ is a versatile, commercially available compound that has previously found application as a spin-on, interlayer dielectric. It is also a well known a high-resolution e-beam resist that affords 20 nm resolution and feature sizes as small as 7 nm.[13] With all the added benefits associated with solution processability, commercial availability, and straightforward lithographic patterning, HSQ should be an excellent precursor for the fabrication of Si-NC thin films. In the present work, a new solution-based procedure for preparing Si-NC/SiO_2 thin films enables conformal coverage of non-planar surfaces and direct lithographic patterning.

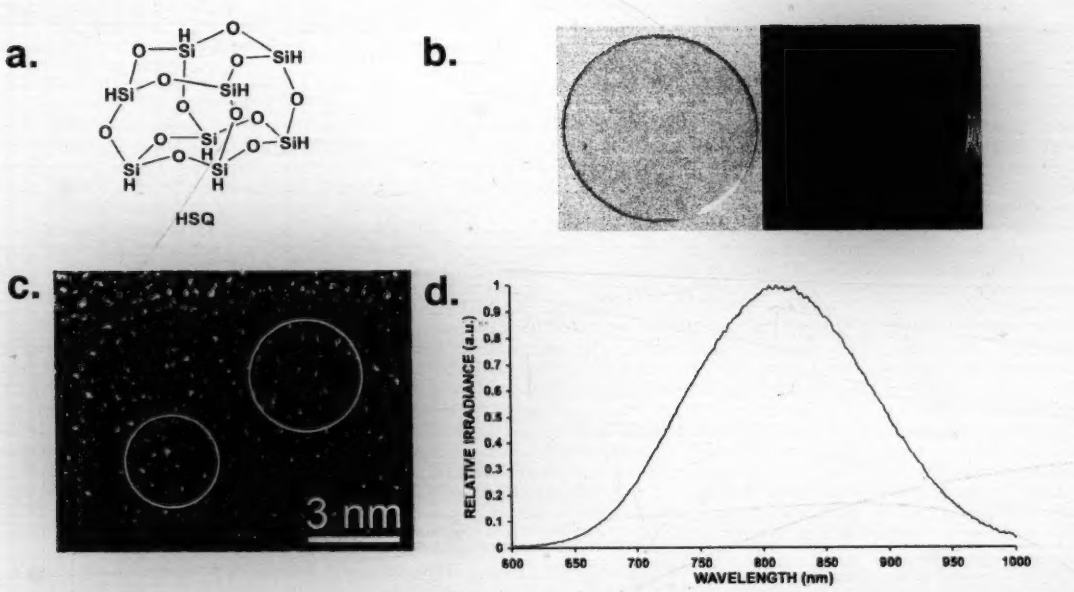

Figure 5.1. a) Structure of hydrogen silsesquioxane. This material can be spin coated onto large wafers (b). The HSQ structure collapses upon thermal processing to form Si-NCs in SiO_2, as shown in the high-resolution TEM image in (c). Panel (d) shows the photoluminescence spectrum (λ_{ex} = 325 nm) obtained from spin-coated films in (b).

5.2. Experimental Details

5.2.1. Geometry Preparations

Geometry 1. In a nitrogen-filled glovebox (< 0.1 ppm H_2O; 0.6 ppm O_2). HSQ stock solution was spin-coated onto quartz substrates using a Laurell Technologies WS-400B-6NPP/LITE programmable spincoater. Colorless, transparent, uniform films (ca. 80 nm) of **HSQ** were formed by dropping 0.5 ml of FOx- 17 stock solution onto the substrate followed by spinning at 0-5800 rpm in 5 seconds, followed by an additional 30 seconds at 5800 rpm. Coated substrates were transferred in inert atmsosphere to a high temperature furnace and processed in 5% H_2/95% N_2. While in the furnace, the geometries were rapidly heated (ca. 20°C/min) to peak temperature (i.e., 1100°C) where they remained for 1 hour.

Geometry 2. HSQ thin films (ca. 80 nm) were spin coated onto Si (100) substrates using a Laurell Technologies WS-400B-6NPP/LITE programmable spincoater in a nitrogen filled glovebox (< 0.1 ppm H_2O; 0.6 ppm O_2). Colorless, transparent, uniform films of **HSQ** were formed by dropping 0.5 ml of FOx-12 stock solution onto the substrate followed by spinning at 0-5800 rpm in 5 seconds, followed by an additional 30 seconds at 5800 rpm.

Patterns of **HSQ** were produced using a Raith 150 electron beam lithography system and imaged *in situ*. The 10 keV electron beam had an approximate spot size of 2 nm and produced an exposure dose of 350 $\mu C/cm^2$. Following e-beam exposure, patterns were developed for 1 minute in a 25% tetramethylammonium hydroxide (TMAH) solution, followed by a 10 second rinse in each distilled water and isopropyl alcohol. Patterned

HSQ films were transferred to a high temperature furnace and processed in the same conditions described for Geometry 1.

Geometry 3. The polyimide cladding was removed from silica fiber optic cable (Nufern (Product # 780-HP)) by submersion in boiling sulphuric acid for 10 minutes. The clean fibers were subsequently dipped into the HSQ stock solution, dried in inert atmosphere, and processed in 5% H_2/95% N_2 for one hour at 1100°C.

5.2.2. Optical Characterization

Photoluminescence (PL) spectra of Geometry 1 were obtained at room temperature using the 325 nm line of a He-Cd laser excitation source and a detection system consisting of a fiber-optic digital charge coupled device (CCD) spectrometer whose spectral response was normalized using a standard black-body radiator. Fluorescence imaging was performed by exciting the specimen with either the 405 nm line of an Hg lamp or with the 488-nm line of an Ar laser interfaced to a Nikon inverted microscope. Fluorescence imaging employed a Retiga Exifast camera equipped with a color imaging filter. The same microscope was used for reflection imaging.

5.2.3. Scanning and Transmission Electron Microscopy

SEM micrographs were obtained with a using a JEOL 6301F field-emission scanning electron microscope with an acceleration voltage of 5 kV. TEM imagining was done using a Hitachi HF 3300 300 kV transmission electron microscope equipped with cold field emission gun. The high resolution images were obtained in bright field mode of the

TEM and the electron diffraction patterns were acquired from an area about 500 nm in diameter.

5.3. Results and Discussion

A series of geometrys were prepared for the present investigation to demonstrate the versatility of HSQ as Si-NC/SiO_2 precursor (*vide infra*). Geometry 1 was prepared by spin coating approximately 0.5 ml of the HSQ stock solution onto a quartz wafer. The resulting transparent HSQ precursor film was thermally processed at 1100 °C for one hour in flowing gas (5% H_2/95% N_2) to yield a faintly yellow, transparent film (Figure 5.1b). Transmission electron microscopy of the thermally processed HSQ film demonstrated the presence of diffraction rings unambiguously attributable to silicon, and high-resolution imaging (Figure 5.1d) showed randomly oriented crystalline particles with lattice spacings (3.1Å for (111) planes) consistent with various Si zone axes. The photoluminescence spectrum of processed thin films showed a broad, intense peak centered at ca. 800 nm, widely characteristic of Si-NCs (Figure 5.1c).[14]

Having established the presence of luminescent Si-NCs in thermally processed HSQ thin films, it is necessary to demonstrate the fabrication of structures that exploit the benefits of this method. These advantages include: first, unlike for deposition-based methods, both thin films and macroscopic quantities of Si-NC/SiO_2 can be readily produced.[12a] Second, of key import for the present work, HSQ is also an electron beam resist, which allows the straightforward patterning of Si-NCs to form well-defined Si-NC/SiO_2 structures with sub-100 nm dimensions (no separate resist and etching stages are needed because the nanocrystal-containing material *is* the resist). Third, HSQ solution

processability should allow for fabrication of uniform Si-NC/SiO_2 coatings on non-planar surface by a dip-coating method.

To evaluate the ease of patterning Si-NC/SiO_2 thin films obtained from HSQ reductive processing, Geometry 2 was prepared by spin coating a 60-nm-thick HSQ layer onto a silicon wafer. The HSQ film was preheated to remove any residual solvent that may degrade patterned features, exposed using an electron beam writer, and subsequently developed. Following thermal processing at 1100 °C for one hour, the structures were evaluated using scanning electron microscopy (SEM) and fluorescence microscopy (Figure 5.2). The HSQ-derived Si-NC/SiO_2 patterns withstood high temperature processing with no obvious feature degradation (Figure 5.2a,d,g). The patterned Si-NC/SiO_2 structures are readily visible using a fluorescence microscope (Figure 5.2c,f), with feature sizes approaching the resolution limit of the instrument.

When compared to the extensive body of work focused on Si-NC/SiO_2, the present patterning method yields well-formed structures with obvious advantages that may facilitate the development of efficient silicon-nanocrystal-based waveguides, flash memory, and other devices in which well-defined and smooth lithographic structures are required. We have fabricated highly photoluminescent Si-NC/SiO_2 features approaching the smallest dimensions realized with HSQ as an e-beam resist using the present procedure.[13] This method clearly allows for the preparation of patterns with of sub-10-nm features that contain luminescent nanocrystals without the tedious etching and subsequent oxidation of silicon pillars required when employing standard patterning methods.[9]

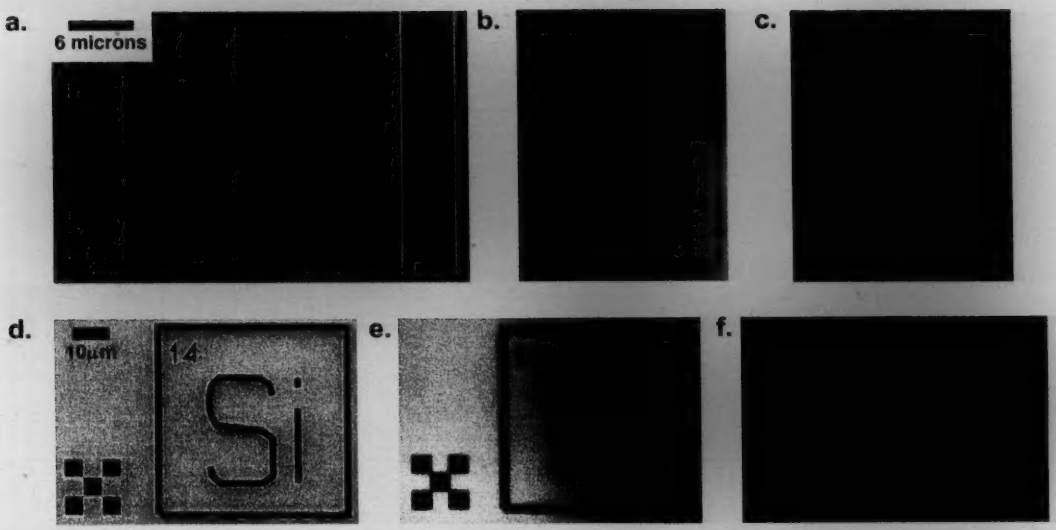

Figure 5.2. a) SEM micrograph of a line pattern of indicated line widths (1μm, 100 nm, 10 nm, 7 nm). b) Reflective optical image of the same line pattern in (a). c) PL image of the line pattern shown in (a) and (b). d) SEM micrograph of a more complex pattern. e) Reflective optical image of pattern in (d). f) PL image of the line pattern shown in (d) and (e).

The next objective was to demonstrate the formation of non-flat coatings of luminescent Si-NC/SiO_2 using HSQ. A commercially available optical fiber was used for this study (Geometry 3). The fiber consisted of a single-mode core with a 125-μm-diameter cladding and a thick polyimide coating with a net fiber thickness 370 μm. The fiber was freed from its protective polymer coating and cleaned using the procedure outlined in the experimental section. The clean fiber was dipped into the HSQ stock solution, and subsequently thermally processed identically as for Geometries 1 and 2. SEM images of nanocrystal-coated fibers are shown in Figure 5.3 a-d. Thicker films (ca. 2.6 μm) obtained from multiple dipping cycles crack and lift off from the fiber surface (Figure 5.3 a). Thinner films are smooth, conformal, and do not crack (Figure 5.3 e). When pumped with a blue laser (488 nm) or even a standard handheld UV lamp, the length of the coated fibers glowed red/orange to the naked eye and an intense red dot could be observed exiting the cleaved end of the fiber (Figure 5.3 f). By examining the fiber end-on in the fluorescence microscope, it is clear that the PL is coupled into the entire cross section – as expected since the Si-NC/SiO_2 layer coats the outer fiber diameter. It is reasonable that similar structures prepared using this straightforward procedure could find applications as gas sensors or in other devices where the Si-NC PL is directly coupled to the optical measurement system.

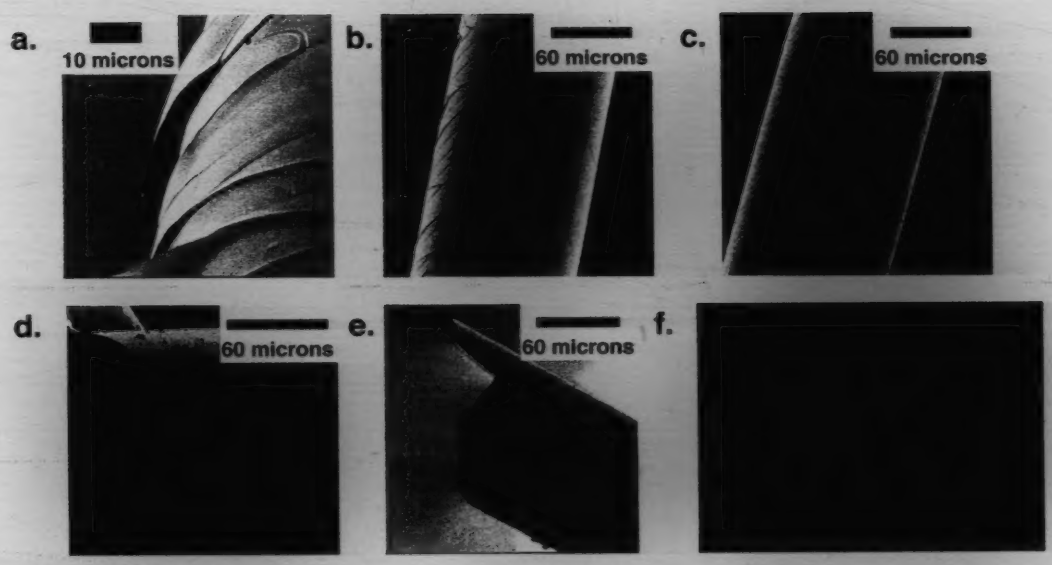

Figure 5.3. Panels a-d show SEM images of optical fibers with Si-NC/SiO_2 coatings of decreasing thicknesses. Thick films crack and peel from the fiber surface, (a). Thinner Si-NC/SiO_2 coatings are smooth and featureless. Panel f shows a fluorescence microscope image of the red-IR emission emanating from the cleaved end of the fiber shown upon 488-nm excitation along the side of the fiber.

The final objective of the present work was to show that Si-NC/SiO_2 produced via the reductive thermal processing of HSQ can sensitize the 1.5 μm emission band of erbium. This demonstration is important for the potential application of HSQ in silicon-nanocrystal-based optical devices. In order to incorporate erbium into the Si nanocrystal films, a small amount of $ErCl_3$ was added to the HSQ stock solution. Figure 5.4 shows the effect of adding erbium to the Si-NC/SiO_2 composite. Identical to the case for Si-NCs produced by standard thin film methods, a Si-NC PL band was observed along with a 1.5 μm emission arising from the $^4I_{13/2} \rightarrow {}^4I_{15/2}$ transition of Er^{3+}, when pumped non-resonant with any erbium absorption band. This is consistent with the Si-NC sensitization of the erbium luminescence and demonstrates that the HSQ method for fabricating Si-NC/SiO_2, in addition to all the advantages discussed previously, can readily be extended to wavelengths of relevance for optical communications.

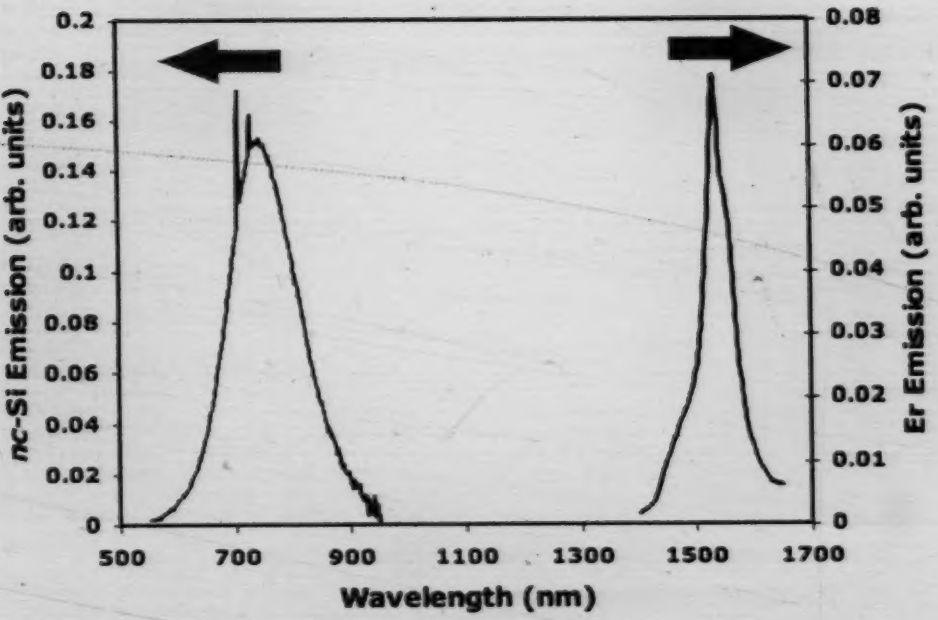

Figure 5.4. A photoluminescence spectrum of Er doped Si-NC/SiO_2 composites upon excitation with the 325 nm line of a He-Cd laser excitation source. This spectrum clearly shows the Si-NC emission as well as the characteristic 1540 nm line arising from energy transfer from the Si-NCs to the Er dopant. The spectra are normalized to the same height for clarity.

5.4. Conclusion

The present work demonstrates that HSQ offers advantages when compared to *status quo* physical synthetic methods. Although the present HSQ-based procedure still requires films be processed at $T \geq 1000$ °C, we have shown that oxide-embedded amorphous Si nanoclusters form at processing temperatures as low as 500°C,[12b] as is the case of films synthesized by PVD methods.[15] These amorphous materials are similarly efficient sensitizers of erbium and other rare earth ions.[16] To conclude, the solution-based method for forming Si-NCs has many striking advantages over previous techniques. First, large wafers can be spin-coated without the need for a costly implantation or thin film system, or any previous processing. Second, because HSQ is an electron-beam resist, it affords all the advantages of nanometer-scale patterning without the need for complicated etching recipes. Third, it is possible to uniformly coat any (non-flat) structure that can be dipped into solution, and fourth, erbium doping to produce 1.5 μm luminescence is equally simple and affords all of the well-known advantages with respect to nanocrystal sensitization of erbium.

5.5. Reference

(1) J.M. Buriak *Chem. Rev.* **2002**, 102, 1271.

(2) J.G.C.Veinot *Chem. Comm.* **2006**, 40, 4160.

(3) A. Meldrum, *Recent Res. Devel. Nuclear Phys.* **2004**, 1, 93.

(4) D.J. Lockwood, L. Pavesi, *Top.* in *Appl. Phys.* **2004**, 94, 1.

(5) a) R.J. Walters, G.I. Bourianoff, H.A. *Atwater Nature Mater.* **2005**, 4, 143., b) J. Valenta, N. Lalic, J. Linnros *Appl. Phys. Lett.* **2004**, 84, 1459., c) M.A. Green, J.H. Zhao, Wang, P.J. Reece, Gal, M. *Nature* **2001**, 412, 805., d) N. Lalic, J. Linnros *J. Lumin.* **1998**, 80, 263.

(6) L. Pavesi, *Proc. SPIE*, **2003**, 4997, 206.

(7) C.M. Compagnoni, R. Gusmeroli, D. Ielmini, A.S. Spinelli, A. L. Lacaita, J. *Nanosci. and Nanotech.* **2007**, 7, 193.

(8) a) A. Hryciw, C. Blois, A. Meldrum, T. Clement, R. DeCorby, Q. Li *Optical Mater.* **2006**, 28, 873., b) Y.H. Ha, S. Kim, D.W. Moon, J.-H. Jhe, J.H. Shin *Appl. Phys. Lett.* **2001**, 79, 287., c) M. Schmidt, J. Heitmann, R. Scholz, M. Zacharias, *J. Non-Cryst. Solids* **2002**, 299 302, 678., d) J.S. Ha, G.Y. Sung, S. Lee, Y.R. Jang, K.H. Yoo, C.H. Bae, J.S. Jeon, S.H. Nam, S.M. Park, *J. Appl. Phys. A* **2004**, 79, 1485.

(9) T.J. Clement, R.G. DeCorby, N. Ponnampalam, T.W. Allen, A. Hryciw, A. Meldrum, *Optics Express*, **2006**, 14, 12151.

(10) V. Svrcek, A. Slaoui, and J.-C. Muller, *J. Appl. Phys.*, **2004**, 95, 3158.

(11) L. Zhang, J.L. Coffer, and T Waldek Zerda, *J. Sol-Gel Sci. Technol.* **1998**, 11, 267.

(12) a) C.M. Hessel, E.J. Henderson, J.G.C. Veinot, *Chem. Mat.* **2006**, 18,6139. b) C.M. Hessel, E.J. Henderson, J.G.C. Veinot, *J. Phys. Chem. C.* **2007**, 111, 6956.

(13) I.B. Baek, J.H. Yang, W.J. Cho, C.G. Ahn, K. Im, S. Lee, *J. Vac. Sci. Tech. B.* **2005**, 23, 3120.

(14) A. Meldrum, A. Hryciw, A.N. MacDonald, C. Blois, K. Marsh, J. Wang, and Q. Li, J. *Vac. Sci. Technol. A*, **2006** 24, 713.

(15) J. Wang, X.F. Wang, Quan Li, A. Hryciw, and A. Meldrum, *Phil. Mag.* **2007**, 87, 11.

(16) A. Meldrum, A. Hryciw, N. MacDonald, C. Blois, T. Clement, R. DeCorby, J. Wang, Quan Li, *J. Lumin.* **2006**, 121, 199.

Chapter 6:

Conclusions

6.1. Conclusions

Since the first report of luminescent silicon nanomaterials in 1990 there have emerged a variety of methods for producing oxide-embedded and freestanding Si-NCs.[1] Criteria to evaluate the advantages/disadvantages of these many synthetic routes do not exist, and as such, a means to evaluated the paramount method is lacking. Considering that each method has its own application domain it is quite difficult to carry out this evaluation. For example, ion implantation is an effective method for producing oxide-embedded Si-NCs for non-volatile memory applications, as it is compatible with current device fabrication procedures,[2-4] but it is an inappropriate route for producing large quantities of freestanding Si-NCs with controlled surface chemistry. The inability of a single technique to produce Si-NCs with the desired characteristics that span the gamut of potential applications is likely the reason why a set of criteria has yet to be established. However, considering the strengths of the preparative methods found in the literature, along with a rational approach to materials production in general, criteria for an ideal preparative method can be devised.

An ideal preparative method for Si-NCs should include the following:

1) Afford well-defined Si-NCs in tangible quantities (> 500 mg/batch). In order to realize the full application potential of Si-NCs, the method must produce enough material to fundamentally evaluate their properties, and provide the working material necessary for intended applications.

2) The precursors should be readily available. The ease by which a Si-NC precursor can be purchased or produced would not only streamline synthesis, but also increase its usage as a preferred preparative method.

3) The synthetic procedure should be straightforward and the resulting nanocrystals easily incorporated into a variety of applications. Increasing the simplicity of the procedure by reducing the number of synthetic steps to a point where personnel with minimal training can produce Si-NCs would allow for the ubiquitous utilization of the method.

4) Minimal investment of infrastructure. The synthetic method should run on inexpensive, easily obtained equipment found in typical chemistry laboratories.

5) The procedure/precursor should be versatile and capable of producing most, if not all, of the Si-NC morphologies and architectures reported in the literature. If a single method/precursor had the ability to produce thin films of Si-NCs, oxide-embedded Si-NCs, and freestanding Si-NCs with controlled surface chemistry, it would have the potential to encompass all current methods of forming Si-NCs.

Considering these criteria, the existing strategies to produce Si-NCs may be evaluated. It is clear from the brief review of current methods to prepare Si-NCs presented in the introduction, that no single method satisfies all of the above criteria. The most significant limitation of these physical and solution-based reduction methods involves their inability to produce large quantities of Si-NCs (> 500 mg/batch). In this regard, Swihart's laser-based synthesis would be the superior method,[5] as it provides tangible (20 – 200 mg/hour) amounts of reasonably well-defined material. However,

the custom-built reactor vital for this synthesis, the requirement for highly trained personnel, and the inability to produce thin films of oxide-embedded Si-NCs, could prevent the overall wide range acceptance of this procedure. With regard to architectural versatility, only the SiO_x based methods have yielded thin films and bulk composites. However, as previously described, challenges associated with precursor purity and deposition homogeneity may inhibit the eventual application of this precursor material. The limitations associated with established methods to produce various architectures of Si-NCs provide the motivation to investigate new Si-NC precursors that satisfy the aforementioned criteria.

The synthetic strategy for producing Si-NCs outlined in the present thesis demonstrates that hydrogen silsesquioxane (HSQ) satisfies many of the requirements outlined for an ideal Si-NC precursor. With respect to the preparation of tangible amounts of material, a typical bulk synthesis of oxide-embedded Si-NCs from HSQ reproducibly generates 4 grams of well-defined material in a single batch, with reaction times of approximately 4 hours. Increasing the batch yield of this synthesis could be easily achieved by scaling to a larger flow-through tube furnace that can accommodate additional precursor. In terms of precursor purity and availability, the challenges associated with the purity of SiO_x are not present for HSQ since it is commercially available at purity levels that meet the standards of the microelectronics industry. It is also easily obtained in most microfabrication facilities given that it is typically used as a spin-on dielectric for device fabrication and as a common e-beam resist. The cost associated with HSQ is minimal. As a solid resin, HSQ costs approximately $17/gram.

Furthermore, if thin film architectures are not required, producing HSQ analogues via a straightforward sol-gel approach may eliminate the majority of this expense.[6,7]

HSQ-based preparation of thin films and bulk composites of oxide-embedded Si-NCs has also been designed to be as straightforward as possible, requiring only minimal infrastructure. In its current form, the production of oxide-embedded Si-NCs requires an inexpensive ($4000) flow-through tube furnace which is a common piece of equipment in most materials chemistry laboratories. For thin film production, the costly and infrastructure-intensive ion implantation and thermal deposition systems are replaced with a standard spin-coater tube furnace. In addition, it has been demonstrated that conformal thin films containing oxide-embedded Si-NCs can be applied to flat and non-flat surfaces, a substantial advantage over line-of-sight physical deposition techniques. The versatility of HSQ is also highlighted by its ability to act as a single source precursor, producing bulk material and thin films of oxide-embedded Si-NCs.

The presented HSQ-based technique can also be used to produce freestanding Si-NCs with controlled surface chemistry that emit across the visible and NIR regions of the electromagnetic spectrum. The development of a recipe-based etching procedure has led to the production of freestanding Si-NCs with predictable size, surface chemistry, and emission characteristics. In context of the aforementioned criteria for an ideal preparative method, it is apparent that utilizing HSQ as a precursor has the potential to revolutionize the way scientists produce Si-NCs. With this in mind, it is important to understand the fundamental mechanisms responsible for Si-NC formation from HSQ and the origin of their photoluminescence response.

Using a combination of diffraction and spectroscopic techniques, the thermally-induced evolution of HSQ to oxide-embedded Si-NCs was monitored, and can be understood in terms of a thermal disproportionation reaction. The processes by which this transformation occur may be divided into 3 steps that occur in separate temperature regimes.

1) HSQ cage rearrangement: 200°C - 400°C.

The initial stages of thermal processing lead to a rearrangement of the HSQ cage structure and further crosslinking into a network solid.. Although only subtle changes were observed in FTIR spectra, similar observations were interpreted in the same manner in a previous thermal decomposition study of HSQ.[8]

2) Formation and nucleation of silicon nanodomains: 400°C - 900°C.

Throughout this temperature regime, XP and Raman spectroscopy identified the formation of partially hydrogenated, low oxidation state silicon clusters within the oxide matrix. Near-edge X-ray absorption fine structure (NEXAFS) spectroscopy also showed an evolution of the silicon 1s absorption edge with increased processing temperature consistent with an HSQ disproportionation reaction. Between 500°C and 900°C the characteristic spectral feature of the dominant Si^{3+} species present in HSQ slowly diminishes, with concomitant emergence of Si^{0} and Si^{4+} spectral signatures. The mechanism of cluster formation may be rationalized in the context of formation and *in situ* decomposition of silane-like species that result from the rapid (> 18°C/min) thermal processing of HSQ. This process continues to 900°C, where XP analysis shows an

unchanging Si^0 content with increasing temperature, and FTIR spectroscopy shows the disappearance of a silicon hydride stretching absorption, which is indicative of a complete disproportionation reaction.

3) Nanodomain crystallization: > 900°C.

Increasing the temperature above 900°C promotes crystallization of elemental silicon nanodomains and leads to Si-NCs growth. The combination of TEM, XRD, and PL spectroscopy indicate that the photoluminescence characteristics of oxide-embedded Si-NCs depend strongly on synthetic processing variables. An increase in the processing temperature above 900°C yield Si-NCs of increasing size, accompanied by a decrease in the PL emission energy. This correlation of emission energy and nanocrystal size suggests that the PL emission is a result of quantum confinement effects in sub-5 nm Si-NCs. This relationship was further investigated by subsequent X-ray-based spectroscopic studies in order to establish causation (*vide infra*). A red-shift in the emission energy was also observed after prolonged thermal processing at constant temperatures. However, since this PL energy shift was not accompanied by an increase in nanocrystals size, as confirmed by XRD, the change in luminescence characteristics is attributed to the passivation of volume defects in larger nanocrystals and subsequent tunneling proceses that result in preferential radiative recombination in these large nanocrystals.

Through controlled, monotonic increases to the processing temperature, between 900°C and 1400°C, resulting in corresponding increases in nanocrystal diameter, oxide-embedded Si-NCs have been shown to emit between 690 – 900 nm. Additionally, when

the particle diameter is decreased via hydrofluoric acid etching, the emission can be tailored throughout the visible region, from the initial emission energy observed in the composite (e.g., 800 nm for HSQ processed at 1100°C), to approximately 530 nm. In order to understand the origin of this photophysical dependence on nanocrystal size and to isolate specific chemical species responsible for luminescence from oxide-embedded and freestanding silicon nanocrystals, X-ray excited optical luminescence (XEOL) was employed. XEOL spectra of oxide-embedded Si-NCs yielded two emission bands in the visible spectrum: a low energy band at 780 nm and a high energy band at 540 nm, absent from low energy laser-based spectroscopy. Variable excitation XEOL spectra show a correlated quantum yield enhancement of the low energy emission band with X-ray excitation of elemental silicon, and a similar enhancement of the high-energy emission band upon X-ray excitation of SiO_2. This band assignment was further supported using a HF etching procedure to remove matrix and surface oxides to produce oxide-free freestanding Si-NCs, as confirmed by post-etching NEXAFS spectra. The loss of the high energy emission band at 540 nm as a result of oxide removal supports the assignment of this band to a silicon oxide species that is present at the interface between the Si-NC core and the surrounding SiO_2 matrix. Hydride-terminated freestanding Si-NCs of decreasing size exhibited a blue-shift in the energy of the 780 nm emission band, confirming that this emission is a result of quantum confinement processes in Si-NCs. To our knowledge, this investigation is the first that conclusively establishes quantum confined emission processes as the governing radiative pathway in oxide-free, hydride terminated Si-NCs.

In addition to determining the origins of emission from oxide-embedded and freestanding Si-NC systems, the XEOL investigation emphasized the influence of Si-NC surface chemistry on the resulting emission characteristics. It also demonstrated the procedure developed for liberating Si-NCs from oxide-embedded composites yields oxide-free, freestanding Si-NCs that have a hydride-terminated surface. Considering the versatility of silicon hydride surfaces, this provides a fundamental understanding of the composition and emission characteristics for hydride-terminated Si-NCs.

Not only does this thesis describe research that thoroughly investigated a new and versatile route to the production of Si-NCs, it also establishes a methodology for forming tangible quantities of oxide-embedded nanocrystals via a thermal disproportionation of metal rich oxides with specific metal to oxygen ratios of 1:1.5. This synthetic route may be applied to a variety of alternative oxide-embedded metal nanocrystal systems, with the exception of elements having low crystallization temperatures. The applicability of this methodology already been demonstrated by Henderson *et al.* in the synthesis of well-defined, oxide-embedded germanium nanocrystals.[9] In this report, a sol-gel route was employed to produce a germanium rich oxide polymer with a germanium to oxygen ratio of 1:1.5. Thermal processing of the polymer resulted in size monodisperse oxide-embedded germanium nanocrystals with size dependent photophysical properties. In addition, the ease by which HSQ can be used to form conformal coatings on non-flat surfaces has been utilized as a method to produce low loss optical cavities containing Si-NCs. In this demonstration, the clever incorporation of HSQ onto the inner walls of a hollow quartz capillary provided an

optical cavity with a Q-factor that is unsurpassed in the literature.[10] These two reports exemplify the potential applicability and versatility of the HSQ methodology.

6.2. Future direction

Although it has been demonstrated the HSQ methodology is a versatile route to form Si-NCs in many morphologies there are still synthetic challenges to address. In particular, the formation of freestanding Si-NCs requires the use of hazardous hydrofluoric acid. The risks associated with the liberation procedure could be greatly reduced if a benign substitute for this etching reagent could be found. Converting to solution-based route to form freestanding Si-NCs could also alleviate the challenges associated with the Si-NCs liberation procedure. Applying HSQ to well-established solution reduction methods may yield freestanding Si-NCs, and therefore would eliminate the HF liberation procedure. This methodology could also alleviate the requirement of high thermal processing temperatures necessary for the current solid state synthesis.

In addition to the characterization already reported to examine oxide-embedded and freestanding systems, supplementary characterization could be used to better understand the formation and luminescence mechanisms of these materials. In particular, it is essential to determine the lifetime and quantum efficiency of the emission band attributed to interfacial oxides in oxide-embedded systems. Preliminary experiments involving time-resolved XEOL have been devised and will soon be investigated.

6.3 References

(1) Canham, L. T. *Appl. Phys. Lett.* **1990**, *57*.

(2) Liu, Y.; Chen, T. P.; Ng, C. Y.; Ding, L.; Zhang, S.; Fu, Y. Q.; Fung, S. *J. Phys. Chem. B* **2006**, *110*, 16499.

(3) Ng, C. Y.; Chen, T. P.; Du, A. *Physica Status Solidi (A) Applications and Materials* **2006**, *203*, 1291.

(4) Ng, C. Y.; Chen, T. P.; Sreeduth, D.; Chen, Q.; Ding, L.; Du, A. *Thin Solid Films* **2006**, *504*, 25.

(5) Li, X.; He, Y.; Talukdar, S. S.; Swihart, M. T. *Langmuir* **2003**, *19*, 8490.

(6) Pauthe, M.; Bernstein, E.; Dumas, J.; Saviot, L.; Pradel, A.; Ribes, M. *J. Mater. Chem.* **1999**, *9*, 187.

(7) Soraru, G. D.; D'Andrea, G.; Campostrini, R.; Babonneau, F.; Mariotto, G. *J. Am. Ceram. Soc.* **1995**, *78*, 379.

(8) Belot, V.; Corriu, R.; Leclercq, D.; Mutin, P. H.; Vioux, A. *Chem. Mater.* **1991**, *3*, 127.

(9) Henderson, E. J.; Hessel, C. M.; Veinot, J. G. C. *J. Am. Chem. Soc.* **2008**, *130*, 3624.

(10) Rodriguez, J. R.; Veinot, J. G, C.; Bianucci, P.; Meldrum, A. *Appl. Phys. Lett.* **2008**, *92*.